Microchemical Systems for Singlet Oxygen Generation

by

Tyrone Frank Hill

B.S., University of Illinois at Urbana-Champaign (2001)

S.M., Massachusetts Institute of Technology (2004)

Submitted to the Department of Electrical Engineering and Computer Science
in partial fulfillment of the requirements for the degree of

Doctor of Philosophy

at the

MASSACHUSETTS INSTITUTE OF TECHNOLOGY

September 2008

Author .....
Department of Electrical Engineering and Computer Science
August 4, 2008

Certified by .....
Carol Livermore
Associate Professor of Mechanical Engineering
Thesis Supervisor

Accepted by .....
Prof. Terry P. Orlando
Chair, Department Committee on Graduate Students

Microchemical Systems for Singlet Oxygen Generation

by

Tyrone Frank Hill

Submitted to the Department of Electrical Engineering and Computer Science
on August 8, 2008, in partial fulfillment of the
requirements for the degree of
Doctor of Philosophy

Abstract

Chemical Oxygen-Iodine Lasers (COIL) are a technology of interest for industrial and military audiences. COILs are flowing gas lasers where the gain medium of iodine atoms is collisionally pumped by singlet delta oxygen molecules, which are created through the catalyzed multiphase reaction of hydrogen peroxide and chlorine. Currently the use of COIL technology is limited by size and efficiency issues. This thesis seeks to use MEMS technology towards the development of more compact and efficient COIL systems, with a focus on the singlet oxygen generator (SOG) stage. Based on success in other applications, MEMS technology offers opportunities for improved reactant mixing, product separation, and heat transfer in SOGs.

A MEMS singlet oxygen generator (or microSOG) is built and demonstrated. The chip features 32 multiplexed packed bed reaction channels and utilizes capillarity effects to separate the gas and liquid products. Cooling channels are arranged on the chip such that they form a cross-flow heat exchanger with the reaction channels. Spontaneous optical emission measurements and mass spectroscopy are used to confirm singlet oxygen production in the chip. A singlet delta oxygen molar flow rate corresponding to a power of 1.37 W was measured in the chip. The singlet oxygen molar flow rate per unit of hardware volume is $6.7\text{x}10^{-2}$ mol/L/sec, which represents an order of magnitude improvement over sparger and rotary SOG designs.

A detailed physical model is developed to understand the behavior of the microSOG. This model is used along with the experimental results to gain insights into the poorly characterized singlet oxygen deactivation coefficients. Clogging and nonlinear hydraulic behavior prevented the first-generation microSOG from performing as well as the models originally suggested. These issues are addressed in a proposed second generation design, which simulations indicate will produce 50% more singlet oxygen per unit of hardware volume than its predecessor.

Thesis Supervisor: Carol Livermore
Title: Associate Professor of Mechanical Engineering

Acknowledgments

It's hard to believe that my time at MIT is coming to an end. It would be an understatement to say that I have grown both as an engineer and as a person during my stay. Many people have helped me along the way, playing roles as collaborators, mentors, and friends.

I would first like to thank my research advisor, Professor Carol Livermore, for giving me the opportunity to work on such an interesting project. When I began graduate school I never dreamed I would do work spanning the fields of chemistry, physics, and engineering. With her guidance and patience I not only gained knowledge in a variety of new areas, but also learned how to communicate that knowledge to others more effectively.

I acknowledge my thesis committee, Professors Alan Epstein, Klavs Jensen, Vladimir Bulović, and Rajeev Ram for their assistance and suggestions. Prof. Jensen generously volunteered his lab space, equipment, and graduate student expertise to me, which was critical to the success of the project. Additionally, I would like to acknowledge DARPA, MDA, and AFRL, which provided the funding for this research.

My collaborators at MIT, Drs. Ben Wilhite and Luis Velásquez-García, also played key roles in my growth as a researcher. At the beginning of the project Ben took me under his wing, giving me an early crash course in chemical engineering and experimental methods. Without Luis' talent and expertise in the field of microfabrication, it would have been impossible for us to meet the ambitious project schedule laid out by DARPA. I would also like to thank Drs. Terry Rawlins, Sun Lee, and Steve Davis of Physical Sciences Inc., for their collaboration with our group. Because of my many conversations with Terry I now know more than I ever thought I could about physical chemistry and O_2 spectroscopy.

I'd also like to thank the other members of the Micropower and Nanoengineering Research Group: Gunjan Agarwal, Feras Eid, Frances Hill, and Nader Shaar. Their camaraderie over the years was invaluable to me.

Up to this point, those that I have acknowledged have mainly contributed to the

professional side of my development over the past several years. However, there were many others who have been important to me on a personal/social level.

First, I'd like to thank Brian Taff and Amil Patel, for always having time to grab a beer or a burrito and kick back with me. I owe my many trips to Taiwan Café and Cranium skills to my friendships with Dave Chao, Karen Wong, and Hannah Seong. Thanks to Dr. Chris Rycroft, Steve Kohen, and Shawn Kuo for making our apartment in Central Square, known to us as Club UK, an always interesting place to live for four of my six years in Cambridge. I am grateful to Binayak Roy, who allowed me to temporarily escape the lab during our many workouts at the Sidney-Pacific gym and dinners at Cambridge Brewing Company. Whether we were just hanging out in Boston or on a camel ride in the deserts of India, the time I spent with Vivian Lei and Dr. Joe Rumpler was always enjoyable. Anuja Mahashabde always kept me updated on the Indian soap operas. Whenever I pass by Toscanini's Ice Cream in Central Square, I will fondly remember my many late-night conversations there with Melva James. Similarly, in my mind eating at Punjab in Arlington will always be synonymous with Gina Gebhart.

Finally, I would like to acknowledge my family for their support over the years. Comparing notes on the graduate school experience with my brother Eric has definitely made the process more tolerable for me. I thank my parents, Darlene and Frank Hill Jr., and my brother Brian for listening to my successes and gripes over the past six years by phone. Their ability to have a positive outlook on nearly any situation was a great asset to me.

Contents

1 Introduction **23**

1.1 What is COIL? 23

1.2 What is Singlet Oxygen? 27

1.3 Performance Metrics 28

1.4 Previous Work 28

1.5 The MEMS approach 29

1.6 Thesis Contributions 32

1.7 Thesis Outline 32

2 The First-Generation MicroSOG Device **33**

2.1 Functional Requirements 33

2.2 Mixing 34

2.2.1 Reaction Channels 34

2.2.2 Bifurcated Inlets and Pressure Drop Channels 38

2.2.3 Other Considerations 39

2.3 Separation 39

2.4 Heat Transfer 41

2.5 Fabrication Process 41

2.6 Summary 42

3 A Physical Model for the MicroSOG **45**

3.1 Chemical Model 45

3.1.1 Deactivation Model 54

3.2 Fluidic Model 55
3.2.1 Hydrodynamics of a Parallelized Reactor 56
3.2.2 Reaction Channel Flow Regime Model 57
3.2.3 A Geometric Contact Area Model 61
3.2.4 Gas - Liquid Separator 63
3.3 Thermal Model 66

4 Experimental Techniques and Measurements 73
4.1 Packaging 73
4.2 Testing Rig 75
4.3 Optical Emission Setup 78
4.4 Mass Spectroscopy 81
4.5 Experimental Procedure 82

5 Experimental Results and Analysis 85
5.1 Preliminary Characterization 85
5.1.1 Helium and Water Flows 85
5.1.2 Cooling Channel Characterization 86
5.2 Operating Points and Parameter Space 87
5.3 Mass Spectroscopy Results 88
5.4 Spontaneous Emission Results 90
5.4.1 Determination of $O_2(a)$ Concentration 91
5.4.2 Fine Structure of Oxygen 95
5.5 Kinetics Analysis 97
5.5.1 Modifications to the Model 98
5.5.2 Results with Adjusted Constant 103
5.6 MicroSOG Power Extraction 104

6 Design of a Second-Generation MicroSOG Device 107
6.1 Motivation 107
6.2 Proposed Design 109

6.2.1 Pressure Drop Channels 109
6.2.2 Reaction Channels 110
6.2.3 Gas-Liquid Separator and Exit Length 117
6.2.4 Cooling Channels 117
6.3 Performance 118

7 Conclusions and Future Work **121**
7.1 Key Results and Conclusions 121
7.2 Future Work 122
7.2.1 Reducing the Reaction Volume 122
7.2.2 Integration and Scale-up 123
7.2.3 Packaging and Materials 124
7.2.4 Modeling and Kinetics 125
7.2.5 MEMS-based jet SOGs 125
7.2.6 Alternative Iodine Pumping 125
7.3 Final Thoughts 127

A Mask Set **129**

B Fabrication Process **137**

C Experimental Protocol **145**
C.1 Equipment 145
C.2 KOH Preparation 145
C.3 Packaging 146
C.4 Gas Flow Startup 146
C.5 Liquid Flow Startup 147
C.6 Reducing Separator Pressure 147
C.7 Reducing Plenum Pressure 148
C.8 Attaining the Desired Set Point 148
C.9 Opening Chlorine Supply Line 148
C.10 Running the Singlet Oxygen Reaction 149

C.11 Shutting Down the Experiment 149
C.12 BHP Disposal 151
C.13 Closing and Purging Chlorine Line 151
C.14 Final Tasks 152

List of Figures

1-1 Illustration of the energy transitions in an oxygen-iodine system. . . . 24

1-2 Block diagram of a COIL system. 25

1-3 Spin configuration of singlet oxygen. 27

1-4 Illustrations of the rotary (A), jet (B), and sparger (C) SOG designs [55], [16]. 30

1-5 Conceptual illustration of the microSOG concept [11]. 31

2-1 Cutaway view of the microSOG illustrating: (1) the bifurcated liquid inlet, (2) the reaction channels, (3) pores for product separation, and (4) cooling channels. 35

2-2 Deconstructed view of the silicon microSOG layers highlighting the gas (green), liquid (blue), and coolant (yellow) flow paths. 36

2-3 Schematic of microSOG with top and profile views of the posts in the reaction channels. 37

2-4 Illustration of the microSOG featuring the pores of the gas-liquid separator. 40

2-5 Photograph of first generation microSOG device 42

3-1 Cartoon depicting Cl_2 diffusion into BHP film, $O_2(a)$ reaction, and diffusion of the gaseous products out of the liquid. 46

3-2 Species profile per reaction channel length, assuming Q_{gas} of 175 sccm, Q_l of 1 ml/min, and a gas outlet pressure of 100 torr. 52

3-3 Per-channel water and hydrogen peroxide gas molar flow rates as function of reactor length. 53

3-4 Liquid-phase peroxide ion density in the BHP as a function of reactor length. 53
3-5 Decay of $O_2(a)$ concentration as a function of time. 56
3-6 Conceptual illustration of flow regime vs. operating point. 59
3-7 Flow map for the present work and other microreactors [56] [43] [12]. 59
3-8 Illustration of the best- (orange) and worst- (green) case scenario wetting fronts for the plug, annular, and churn flow regimes. 62
3-9 Illustration of the gas liquid separator pores (side view) in the steady-state and transient timescales. 65
3-10 (a) Illustration of microSOG in tefzel package; (b) 1-D thermal model of microSOG with an equivalent thermal circuit. 68
3-11 Illustration of lateral temperature variation across the microSOG, package, and ambient. 70

4-1 MicroSOG backside with various inlet and outlet ports. 74
4-2 The microSOG package consists of two Tefzel plates, clamped together by Tefzel screws and bolts. The inlet and outlet ports are sealed by Kalrez and Simriz O-rings and gaskets. 76
4-3 Upon exiting the microSOG, the gaseous products enter a quartz cuvette where the optical emission measurements are conducted. 77
4-4 Schematic of the microSOG test rig. The liquid and gas flow paths are denoted by blue and red arrows respectively. The overlap between the paths is shown in magenta. MFC = Mass Flow controller; BPC = Back Pressure Controller; GCMS = Gas Chromatography-Mass Spectrometer. 77
4-5 (a) Photograph of the microSOG testing rig highlighting gas and liquid flow paths; (b) Deconstructed view of the glass-lined pressurized vessel used to mix and store BHP; (c) Close-up view of the microSOG packaging with video camera, quartz cell, and thermocouples. 79
4-6 Schematic of the PSI optical diagnostic. Collimated optics sample a cylindrical volume in the quartz cuvette. 80

4-7 Photograph illustrating the MIT optical emission diagnostic. 81

5-1 Plot of gas-liquid separator performance for various liquid delivery pressures and 150 sccm of He flow. The points refer to pressure drops below which the separator is unable to prevent liquid from spilling into the gas outlet. ΔP refers to the pressure drop across the pores. 86

5-2 Measured heat removal capacity of the cooling channels versus internal chip temperature. For this plot, the heat source was provided by the ambient environment surrounding the device. 87

5-3 Mass spectrometer data illustrating rise in O_2 partial pressure corresponding to Cl_2 pulses into the chip. 89

5-4 The glow resulting from the dimol emission is visible in (A) the quartz cuvette and in (B) the reaction channels. 90

5-5 Spectrum captured by the MIT diagnostic, with a peak denoting the $O_2(a) \rightarrow O_2(X)$ transition. 91

5-6 MicroSOG emission spectrum for run 6 as captured by the PSI spectrometer. The scans were taken in 5 second increments, and the intensity has arbitrary units. 92

5-7 Spectra indicating the dimol emission from the microSOG. 92

5-8 Potential energy curves for the bound states of O_2 [52]. 95

5-9 Clogging was observed at several points in the microSOG. 99

5-10 Sum of squared errors for runs 1, 2, 6, and 7 plotted against the scalar parameter Λ. 101

5-11 Best fit of runs 1, 2, 6, and 7 to the adjusted constant Λk_*. 101

5-12 Definition of reactor area as it is used in Tables 5.5 and 5.6. 105

6-1 Mach number for various gas flow rates and cross-sectional geometries. 109

6-2 Yield and chlorine utilization versus a. 111

6-3 Chemical efficiency for different reaction channel geometries. 113

6-4 Pressure drop as a function of reaction channel geometry. 114

6-5 Simulation results for parameter sub-space. 114

6-6 Molar flow rates of the Cl_2 and O_2 species as a function of flow length in the proposed microSOG design. 115

6-7 Conceptual drawing of the proposed microSOG device. 119

7-1 Illustration of microSOGs integrated into a full COIL system [11]. . . 123

7-2 High pressure MEMS packaging concept from the MIT microrocket project [46]. 124

7-3 Conceptual view of a MEMS based jet SOG. 126

B-1 (Process flow by which the middle wafer of the microSOG is fabricated. The process flow starts with a DSP p-Si <100> wafer (a). The wafer is oxidized, and alignment marks are transferred to both sides of the wafer (b). The wafer is then coated with 0.5 m of LPCVD silicon-rich silicon nitride, and the film on the top of the wafer is stripped using an RIE step (c). The silicon oxide film on the top surface of the wafer is patterned with the layouts of the pressure drop channels, the liquid inlet manifold, the reaction channels without the packed beds, and the region occupied by the separator (d). The reactor packed beds and an opening in the region that the separator will eventually occupy are then patterned in a resist and etched by DRIE (e). The photoresist film is stripped, and the features etched on the silicon oxide film on the top surface of the wafer are transferred to the silicon substrate using a DRIE step, while etching 20 μm. The wafer is then oxidized (f), and the silicon-rich silicon nitride on the backside of the wafer is stripped using hot phosphoric acid (g). Finally, the layouts of the chip ports and the capillary separator are patterned in a resist on the back side of the wafer, are transferred into the back-side silicon oxide layer with BOE, and are transferred to the silicon with DRIE. The photoresist film is stripped (h) [19]. 138

B-2 Process flow that fabricates the bottom wafer of the SOG. (a) The process flow starts with a DSP p-Si <100> wafer. (b) The wafer is oxidized, and alignment marks are transferred to both sides of the wafer. The wafer is then coated with 4 μm of PECVD silicon oxide on both sides of the wafer and annealed at 950 C in a nitrogen atmosphere (c). The resist is applied to both sides of the wafer. The resist film on the top of the wafer is patterned photolithographically with the layouts of the heat exchanger and the gas inlet manifold, whereas the bottom film is patterned with the layouts of the chip ports. The layouts of both resist films are transferred to the silicon oxide films using a cycled RIE plasma recipe (d). The top of the wafer is then etched with DRIE to a depth of 325 μm (e). Finally, the wafer is flipped over and mounted on top of a quartz wafer, and the chip ports are etched with DRIE (f) [19]. 139

B-3 Process flow to finalize the fabrication of the microSOG. The micro-fabricated middle and bottom wafers (a) are immersed in a 49% HF bath to strip the silicon oxide films (b). The two silicon wafers are fusion bonded (c). Then, a 0.4-μm-thick LPCVD silicon-rich nitride is conformally deposited on the silicon wafer stack (d). Next, the silicon wafer stack is anodically bonded to an unpatterned Pyrex wafer (e). The wafer stack is then die sawed to extract the SOG chips [19]. . . . 140

List of Tables

1.1 COIL versus other high-energy laser technologies. *The efficiency entries for the HF/DF and COIL lasers refer to a chemical rather than an electrical efficiency. 25

3.1 Summary of SOG Kinetics 46

3.2 Expected contact area per unit volume. 63

3.3 Thermal properties of model layers. 67

3.4 Thermal properties of Syltherm coolant at -10°C. 67

5.1 Operating points for the microSOG experiments 88

5.2 Mass spectrometer data for the microSOG experiments 90

5.3 Measured Concentrations from the PSI and MIT diagnostics, along with chemical efficiencies at the measurement point for runs 1-15. . . 94

5.4 Rotational temperatures assuming T=296K. 97

5.5 Table summarizing extrapolated data with adjusted k_*. The superscript e denotes a value extrapolated to the microSOG gas outlet, while the superscript m denotes a model prediction. 105

5.6 Comparison of molar flow rate values between the microSOG and macroscale SOG implementations [28], [21], [18], [41]. 106

6.1 Comparison of dimensions and performance in the old and new reaction channels. * - data refers to the best performance demonstrated in the original microSOG. 116

6.2 Comparison of dimensions in the old and new pressure drop channels 116

6.3 Dimensions for the old and new cooling channels. 118

Nomenclature

Greek Characters

β	calibration factor	N/A
ϵ	void fraction	N/A
σ	surface tension	dynes/cm
λ	wavelength	nm
Λ	fitting parameter	N/A
ρ_x	density of material x	g/cm^3
μ_x	viscosity of material x	g/cm/sec
θ	contact angle	degrees
θ_{rot}	rotational temperature	Kelvin
χ_{detach}	detachment yield loss	N/A
ζ	deactivation probability	N/A
ν	photon frequency	Hz

Other Constants

a	contact area per unit volume	cm^{-1}
a_c	cross sectional area	cm^2
C_i	concentration of species i	cm^{-3}
D_y^x	diffusivity of y in x	cm^2/sec
D_p	post diameter	cm (μm)
D_h	hydraulic diameter	cm (μm)
E_{coil}	overall COIL efficiency	N/A
E_{chem}	SOG chemical efficiency	N/A
F_x	molar flow rate of species x	mol/sec
G,L	gas and liquid mass velocities	g/cm^{2}sec
k_L	mass transfer coefficient	cm/sec
k_x	reaction coefficient	cm^3/sec (cm^3/mol/sec)
L_e	entrance length	cm
L_x	diffusion length of species x	cm
Q	volumetric flow rate	cm^3/sec
r_x	rate of appearance/consumption of species x	cm^3/sec
y_x	mole fraction of species x	N/A
Y_{th}	threshold O_2(a) yield	%

Dimensionless Numbers

M	Mach Number
Bo	Bond Number
Re	Reynolds Number
We	Weber Number
Bi	Biot Number

Chapter 1

Introduction

This chapter provides motivation and background information on the use of microchemical reactors in Chemical Oxygen-Iodine Laser (COIL) systems. First, the COIL concept is described in detail and compared with competing laser technologies. Next, the focus shifts to the singlet delta oxygen generator component of COIL, with a discussion of macro-scale SOGs as well as the most commonly used performance metrics. A survey of the previous work in both the microreactor and COIL fields is provided as context for the reader. Lastly, the contributions of the thesis are stated and the chapters are outlined.

1.1 What is COIL?

Chemical Oxygen Iodine Lasers (COIL) are flowing gas lasers that are scalable to high powers. In COIL systems singlet-delta oxygen (or $O_2(a)$) molecules serve as the pump source, exciting the gain medium of iodine atoms through inter-species collisions. Because the transition between the energetic $O_2(a)$ state and ground state O_2 (or $O_2(X)$) is forbidden according to selection rules, the $O_2(a)$ state is relatively long-lived. This property makes it an excellent energy carrier. The $O_2(a)$ molecule is well suited to transfer energy into iodine because of the similarity in energy gaps between $O_2(a)$ and $O_2(X)$ and the $I(^2P_{1/2})$ and $I(^2P_{3/2})$ states. These gaps are illustrated in Figure 1-1. Since the energy difference ΔE between the oxygen and iodine states is

only about 0.03 eV, energy can theoretically be transferred very efficiently between them. The $O_2(b)$ state shown in Figure 1-1 is a short-lived energetic state whose kinetics are briefly discussed in Chapter 2.

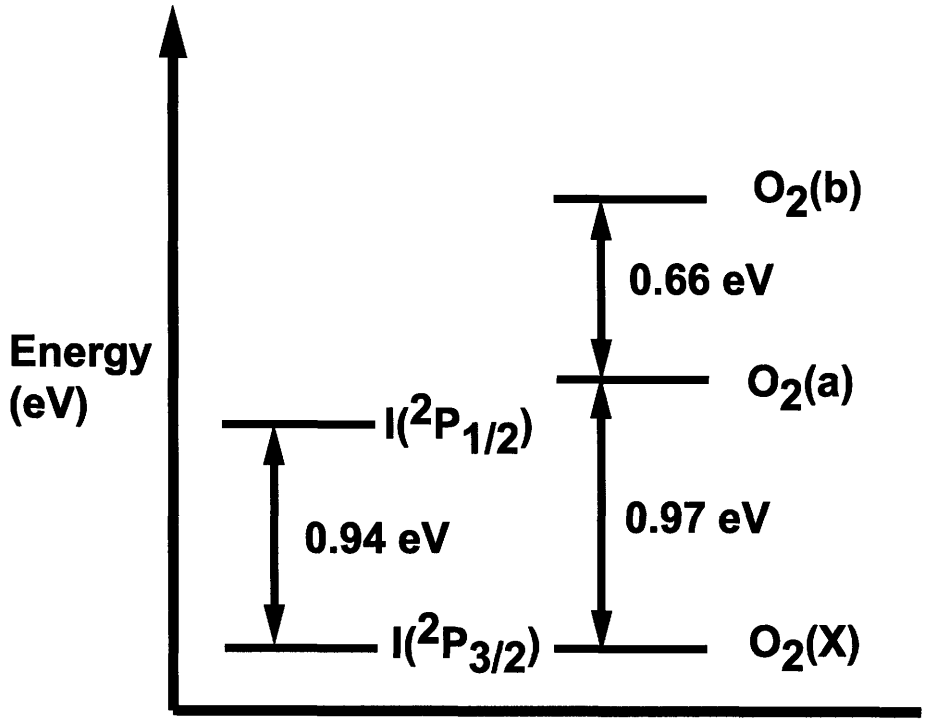

Figure 1-1: Illustration of the energy transitions in an oxygen-iodine system.

All COIL systems contain four components, schematically shown in Figure 1-2: an $O_2(a)$ generator, a mixing nozzle, an optical cavity, and a vacuum pump. The $O_2(a)$ generator supplies a gas stream of $O_2(a)$ that fuels the lasing process in the subsequent stages. In the nozzle stage the $O_2(a)$ molecules transfer their energy to iodine atoms through elastic collisions. Also, some of the $O_2(a)$ energy is expended in order to dissociate I_2 molecules into individual atoms. The I/O_2 mixture is forced through a converging/diverging nozzle, which both cools the gas and increases its velocity. Because the laser gain is inversely related to the temperature of system, cooling the gas mixture enhances COIL performance [32]. COIL systems exhibiting both subsonic and supersonic flow in the nozzle stage have been demonstrated [55]. If the amount of $O_2(a)$ at the nozzle stage is above a certain threshold yield, defined

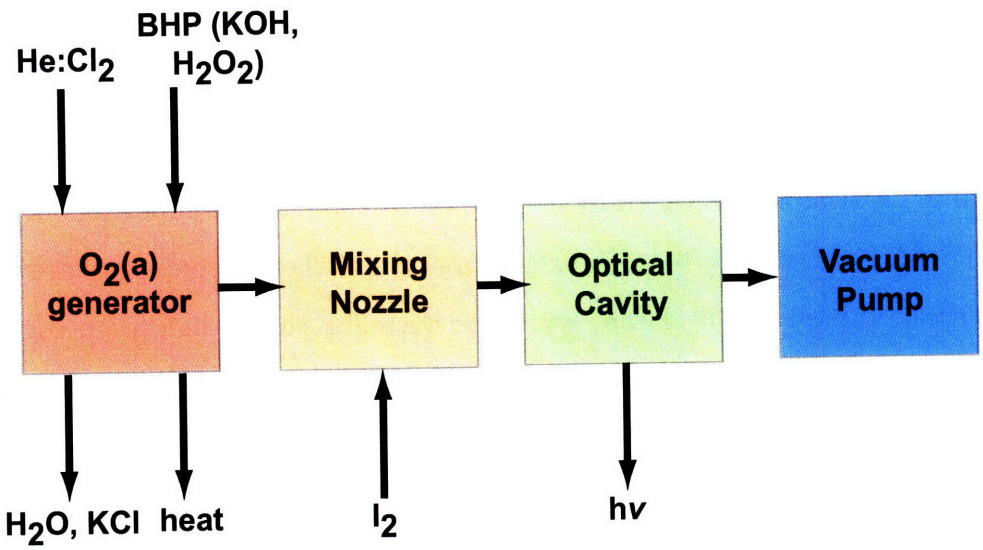

Figure 1-2: Block diagram of a COIL system.

Table 1.1: COIL versus other high-energy laser technologies. *The efficiency entries for the HF/DF and COIL lasers refer to a chemical rather than an electrical efficiency.

Laser Technology	λ (μm)	Steel Reflectivity	Efficiency (%)	Published Power (kW)
CO_2	10.6	>0.8	10-20	25
YAG	1.5	0.55	3.8	5
COIL	1.3	0.6	40* [60]	30 [11]
HF/DF	3-4	0.7-0.8	20*	2200

in [35] as

$$Y_{threshold} = \frac{1}{1 + 1.5 \cdot exp(403/T)}, \tag{1.1}$$

iodine lasing at a wavelength of 1.315 μm occurs. The vacuum pump maintains gas flow through the other three stages, which operate at sub-atmospheric pressures. The overall chemical efficiency of a COIL system,

$$E_{coil} = \frac{Photons\ out}{Cl_2\ molecules\ in}, \tag{1.2}$$

is defined as the ratio between photons out and Cl_2 molecules into the system. The best performing COIL systems have an overall efficiency of approximately 40% [60].

Oxygen-Iodine lasers are well suited to a variety of high-power uses. The most

commonly mentioned of these applications are kW-class metal-cutting systems and MW-class airborne laser systems. These applications require scalability to high powers, good coupling to metals, and a high chemical or electrical efficiency. CO_2, HF, DF, and YAG lasers are generally considered as the major competitors of COIL for high energy applications [31]. The key properties of these technologies are compared to COIL in Table 1.1. CO_2 lasers, which are currently the leading technology in welding and machining applications, are limited by a high characteristic wavelength. The CO_2 wavelength is an order of magnitude larger than the competitor technologies, which results in an inherently larger spot size. Additionally, the beam cannot be used in conjunction with conventional glass optical fibers or focusing optics. The 10.6 μm wavelength also couples poorly to metal substrates; this fact is illustrated by the high reflectivity with steel listed in Table 1.1. In other words, less than 20% of the beam power is transferred to a steel target in a CO_2 laser-based machining system. While YAG lasers feature a wavelength that is compatible with conventional optics, they are limited by poor efficiency. Since the YAG is a solid state laser the output power is proportional to the crystal size, which makes scaling the YAG to powers beyond 5kW difficult due to the challenge of volume to surface heat removal [31]. The HF and DF lasers are the only technology that has been demonstrated at powers necessary for the airborne laser application; however, this system is unattractive due to the production of HF as a waste product.

One of the most critical shortcomings of current COIL systems is size. The need for compact COIL systems is especially critical in missile defense systems, where all of the components and reactants should fit comfortably inside a 747-sized aircraft. Higher efficiency COIL systems will result in lower system size and weight (including the reactants). This thesis aims to make progress towards the development of compact, lightweight COIL systems.

1.2 What is Singlet Oxygen?

The first excited state of O_2, or O_2(a), differs from ground state (triplet or O_2(X)) oxygen because of the spin configuration of its electrons. The difference is illustrated in Figure 1-3; the O_2(X) state has three electrons in the spin-up state and one in the spin-down state (or vice-versa), while O_2(a) features two electrons in each configuration. The O_2(a) state is sometimes written as $O_2(^1\Delta)$, where the superscript refers to the spin degeneracy, and Δ refers to the molecular orbital. The relaxation of the O_2(a) state is theoretically forbidden due to its lack of an electric dipole moment [34]. However, in reality a weak magnetic dipole exists which allows the transition to occur. The molecular structure of the O_2(a) molecule is discussed in greater detail in Chapter 5. The O_2(a) molecule can be generated through the catalyzed reaction of

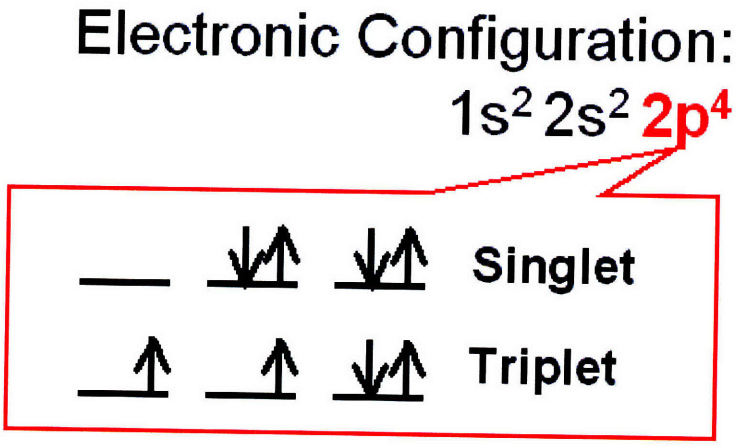

Figure 1-3: Spin configuration of singlet oxygen.

hydrogen peroxide and chlorine, written as

$$H_2O_2 + 2KOH + Cl_2 \longrightarrow 2H_2O + 2KCl + O_2(a). \tag{1.3}$$

In many instances Cl_2 flows in pulses into the system, with He or N_2 used as a buffer gas. The solution of H_2O_2 and KOH used in the reaction is often referred to as "basic hydrogen peroxide" or BHP. The reaction kinetics are discussed extensively in

Chapter 2. Singlet oxygen may also be generated in the discharge of an O_2 plasma. However, this method generates many other species, making it difficult to achieve gain in a scaled-up laser system [15].

1.3 Performance Metrics

The performance of a SOG is evaluated using several performance metrics. The first is O_2(a) yield,

$$Y_{O_2(a)} = \frac{[O_2(a)]}{[O_2(a)] + [O_2(b)] + [O_2(X)]}, \tag{1.4}$$

which measures the fraction of O_2 in the "a" spin configuration. An O_2 molecule that has deactivated to the O_2(X) state has no excess energy to contribute to pumping the iodine atoms in the laser nozzle. The second metric is the chlorine utilization, or the conversion rate of the Cl_2 reactant molecules into O_2 molecules. The microSOG chemical efficiency (E_{chem}) is defined as the product of the yield and chlorine utilization. A high chlorine utilization is important as any remaining Cl_2 in the SOG output stream will deactivate the $I(^2P_{1/2})$ in the cavity stage. The final metric is molar flow of O_2(a) per unit reactor volume. Because of the push to make SOGs more compact and efficient, this value should be as high as possible.

1.4 Previous Work

Researchers in the early 20th century became interested in O_2 because of its emission bands, which were observed in flames and in the upper atmosphere [3]. The dipole-based theory behind the long lifetime of the O_2(a) state was established by the work of Herzberg [34]. Later, the visible luminescence of the O_2(a) molecule was studied by Arnold et al [27]. Derwent and Thrush were the first researchers to consider the possibility of pairing O_2 and I together in a lasing system [7]. The earliest demonstration of this idea was executed by McDermott et al in 1978 [29]. The SOG in this system was a simple sparger where Cl_2 was bubbled through a solution of BHP. The yield for this early generator was measured as $> 40\%$; similar yield values were

obtained in subsequent sparger designs [41]. The strength of the sparger design is its simplicity. However, high residence times in the liquid phase contribute to $O_2(a)$ deactivation and lower the yield. The lack of control of the residence times results in low E_{chem} values as well. Additionally, the BHP becomes diluted over time since it is not continuously cycled through the system as in later designs.

The early success of COIL spawned other versions of the SOG. Figure 1-4 illustrates the varieties of macroscale SOGs that have been used over the years. The rotary disk SOG utilizes a rotating wheel structure to produce $O_2(a)$. The wheel faces have a thin film of BHP, which reacts with Cl_2 fed into the structure. Rotary-based systems have been demonstrated with yields of greater than 50%, and lasers based on rotary SOGs have demonstrated a laser power value of 10 kW [18]. However, rotary disk SOGs are hindered by a small gas-liquid contact area.

The current state-of-the art generators are known as jet SOGs. These generators produce $O_2(a)$ by mixing a jet of BHP droplets with Cl_2. By varying the parameters of the jet stream, the BHP droplet size can be controlled. Jet SOGs have been operated with yields as high as 73% with chlorine utilization values ranging between 90-97% [28].

1.5 The MEMS approach

Recently there has been interest in silicon microtechnology as a means of improving chemical reaction processes [26]. Miniaturized features offer a high contact area per unit volume, resulting in better mixing of multiphase reactants. The high contact area, along with the high thermal conductivity of silicon, also allows microreactors to effectively remove heat generated by exothermic reactions. Silicon offers an added advantage as a lightweight material, potentially reducing the overall weight and volume of a scaled-up reactor. Using the batch fabrication processes perfected by the integrated circuit industry and expanded for other microscale devices, microreactors can be easily multiplexed for high-throughput applications. Additionally, it is possible to parallelize reactors onto a single chip. The miniaturized channel dimensions

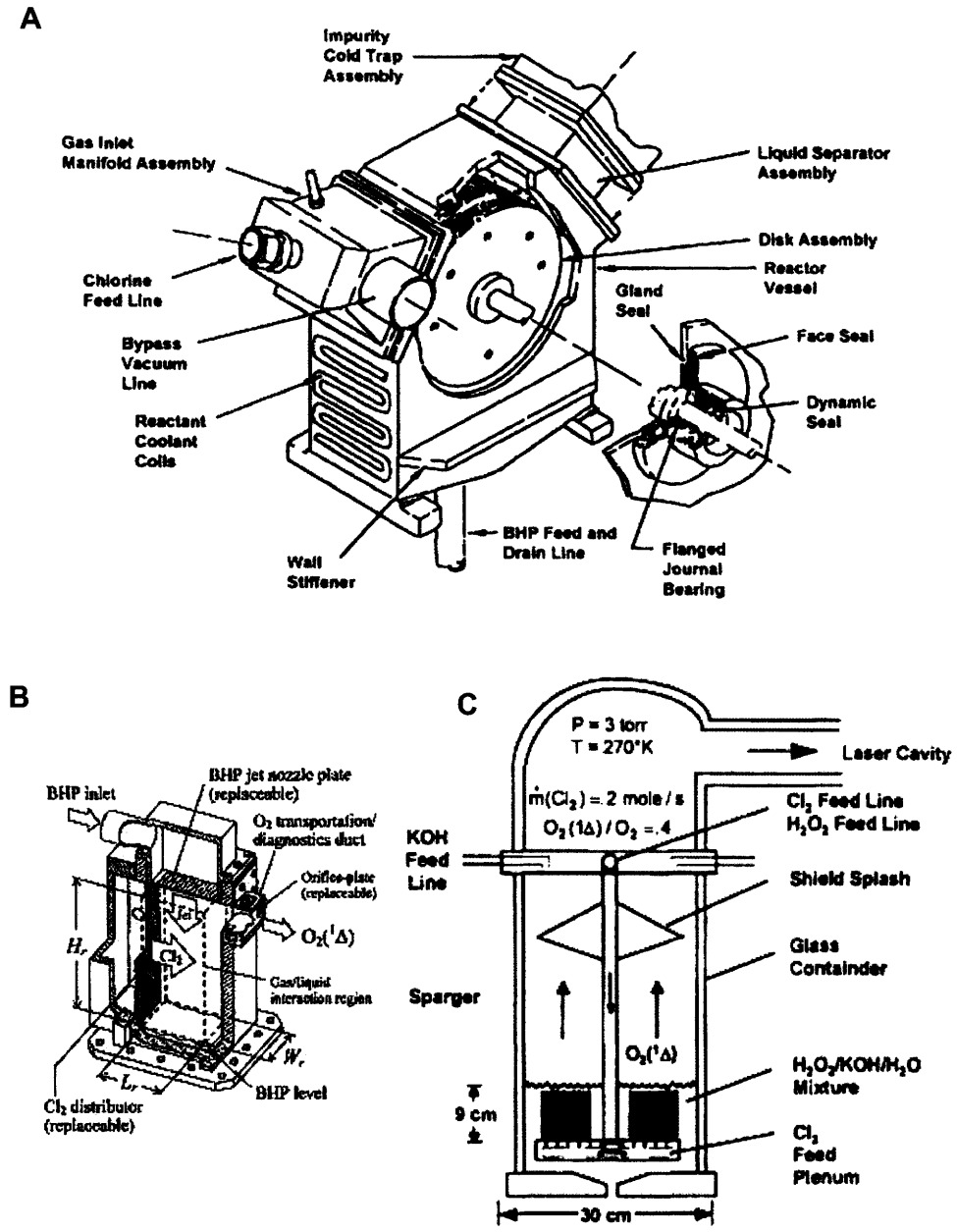

Figure 1-4: Illustrations of the rotary (A), jet (B), and sparger (C) SOG designs [55], [16].

negate the effects of gravity in the device, making the expected flow behavior more straightforward to model.

The theoretical promise of microreactor technology has been applied to real-world applications by MIT researchers over the last several years. Losey et al. fabricated a chip featuring a parallelized array of catalyst-packed channels, which was used for the hydrogenation of cyclohexene [22]. The measured mass transfer coefficient in the chip was two orders of magnitude larger than the values reported in the literature for large scale reactors. The work of Wada et al. used microreactor technology to perform a reaction with toxic reactants under controlled circumstances [56]. Also, Wada et al. demonstrates that the inclusions of posts in the reactor area can increase the rate of mass transfer in the chip.

These previously demonstrated scaling trends and a prior theoretical investigation suggests that MEMS technology can address the shortcomings of each component of a COIL system [11]. Wilhite et al. proposes a SOG design, conceptually illustrated in Figure 1-5, of parallelized reaction channels which are packed with thousands of microfabricated cylindrical posts. The reaction channels are fed by a network of narrow, shallow channels that ensure even reactant distribution. The gas and liquid products are separated by capillary forces. At its conclusion the study predicted each microSOG should be able to source enough $O_2(a)$ to drive about 2.3 W of laser output to a COIL system.

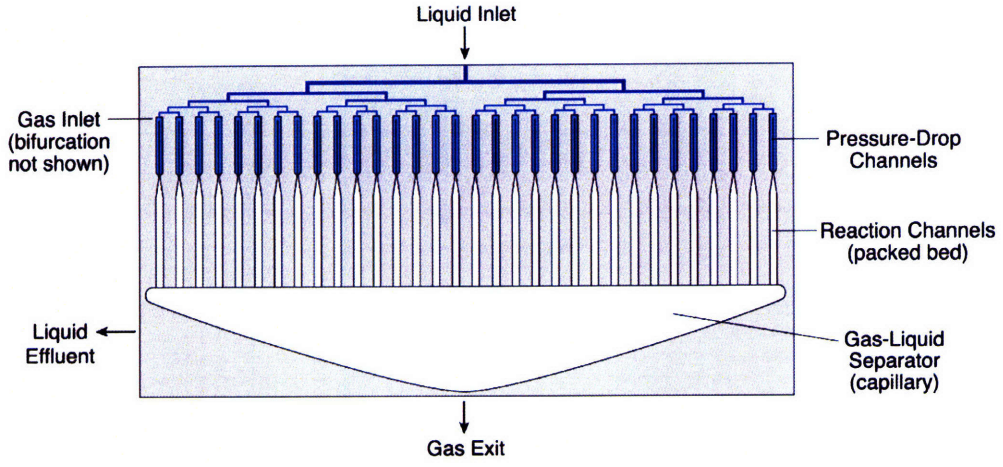

Figure 1-5: Conceptual illustration of the microSOG concept [11].

1.6 Thesis Contributions

This thesis builds on the work of Wilhite et al., with a focus on the SOG stage of the laser. First, the microSOG is realized as an actual device. After demonstrating and quantifying the successful generation of $O_2(a)$, the results are used to gain previously unknown insights into the quenching constants. The results are also used to develop an enhanced physical model of microSOG operation. Finally, the shortcomings of the original microSOG are addressed in a new design. Simulations of the proposed design suggest its performance will exceed that of any known SOG.

1.7 Thesis Outline

This thesis reports on the evaluation of MEMS technology as a method of generating $O_2(a)$ for the COIL application. To this end, Chapters 2 and 3 respectively describe the operational concept and physics of the first generation microSOG device. The testing rig and performance diagnostics are presented in Chapter 4, and Chapter 5 is dedicated to experiments and data analysis. After discussing the limitations of the fabricated microSOG, a better design is proposed in Chapter 6. Chapter 7 contains the thesis conclusions and ideas for future work.

Chapter 2

The First-Generation MicroSOG Device

In the previous chapter, the overall motivation and approach for a MEMS $O_2(a)$ generator were explained. In this chapter, the first generation device is described in detail. The functional requirements for a SOG are outlined, followed by a discussion of how the included features address each specific task. While the design choices behind the feature dimensions are presented here, most of the physics behind their operation is left for Chapter 3. The chapter concludes with a summary of the microSOG fabrication process.

2.1 Functional Requirements

In order to successfully power a COIL system, an $O_2(a)$ generator must meet several key functional requirements, which include:

- Mixing - The generator must provide adequate contact area and residence time for the BHP and Cl_2 to react and produce $O_2(a)$ in sufficient proportions to create gain in the optical cavity of the laser;
- Separation - After the reaction has taken place, the generator must separate the gas phase products, including $O_2(a)$, from the unwanted liquid products;

- Cooling - The generator must have a mechanism for removing both the heat generated from the reaction and the heat flowing into the chip from the outside environment.

The microSOG design must not only execute these functions, but also demonstrate better performance or efficiency than the macroscale alternatives. The following subsections will describe how these requirements are addressed in the initial design. The dimensions for the features are largely based on the theoretical study described in [11]. These functions are realized in the three-layer structure shown in Figure 2-1. The pyrex layer, depicted in blue, seals the device and allows for flow visualization. The other two layers are made of silicon. In the fabricated device all of the inlet and outlet ports are located on the bottom of the chip. The middle layer contains a bifurcated liquid inlet, which distributes the BHP to a parallelized array of reactors. Thousands of cylindrical pores, which are responsible for separation of the reaction products, are also located in this layer. A bifurcated gas inlet that distributes the gas reactants and is not visible in Figure 2-1, exists along with the cooling channels in the lower layer. The flow path of reactants and products through the microSOG is illustrated in Figure 2-2.

2.2 Mixing

Because the microSOG features a parallelized array of reactors, effective mixing involves not only high gas-liquid contact in the reaction area, but also even distribution of the reactants. The following section describes the three features responsible for these tasks: the reaction channels, the pressure drop channels, and the bifurcated inlets.

2.2.1 Reaction Channels

For the $O_2(a)$ reaction to occur successfully, the Cl_2 molecules and BHP must have both sufficient contact area and sufficient residence time to react with each other.

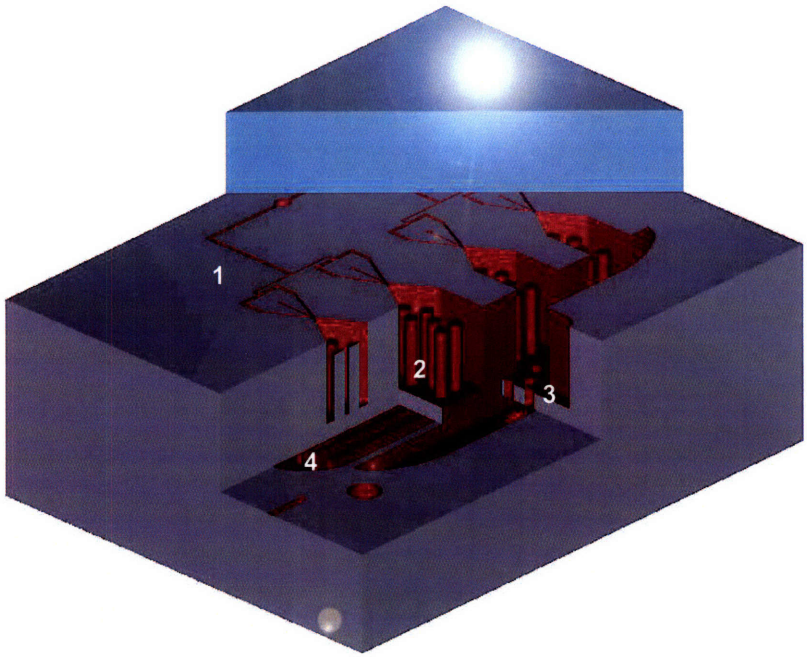

Figure 2-1: Cutaway view of the microSOG illustrating: (1) the bifurcated liquid inlet, (2) the reaction channels, (3) pores for product separation, and (4) cooling channels.

The microSOG design takes an approach similar to that of large-scale trickle bed reactors. These reactors rely on the unsteady flow of multiphase chemicals through a tube to produce a desired chemical reaction [6]. They are typically packed with obstacles (spheres, cylinders, or rings) to increase the contact area between the reactant phases. The tradeoff for this increased contact area is increased pressure drop across the length of the reactor. The first-generation microSOG is essentially a parallelized version of one of these reactors; it in fact contains many packed reactors operating in tandem. Parallelized reactor arrays offer the advantage of increased gas-liquid contact area for a given pressure drop. Also, narrower channels have more uniform heat and mass transfer properties across their widths [43]. However, the parallelized approach requires the inclusion of extra features to ensure uniform reactant distribution; this subject is discussed extensively in the following chapters. Another disadvantage of parallelization is a larger chip area, which lowers the $O_2(a)$ production rate per unit volume of reactor. As a compromise between these competing factors, a design featuring 32 reaction channels is chosen. The reaction channels of the microSOG, shown

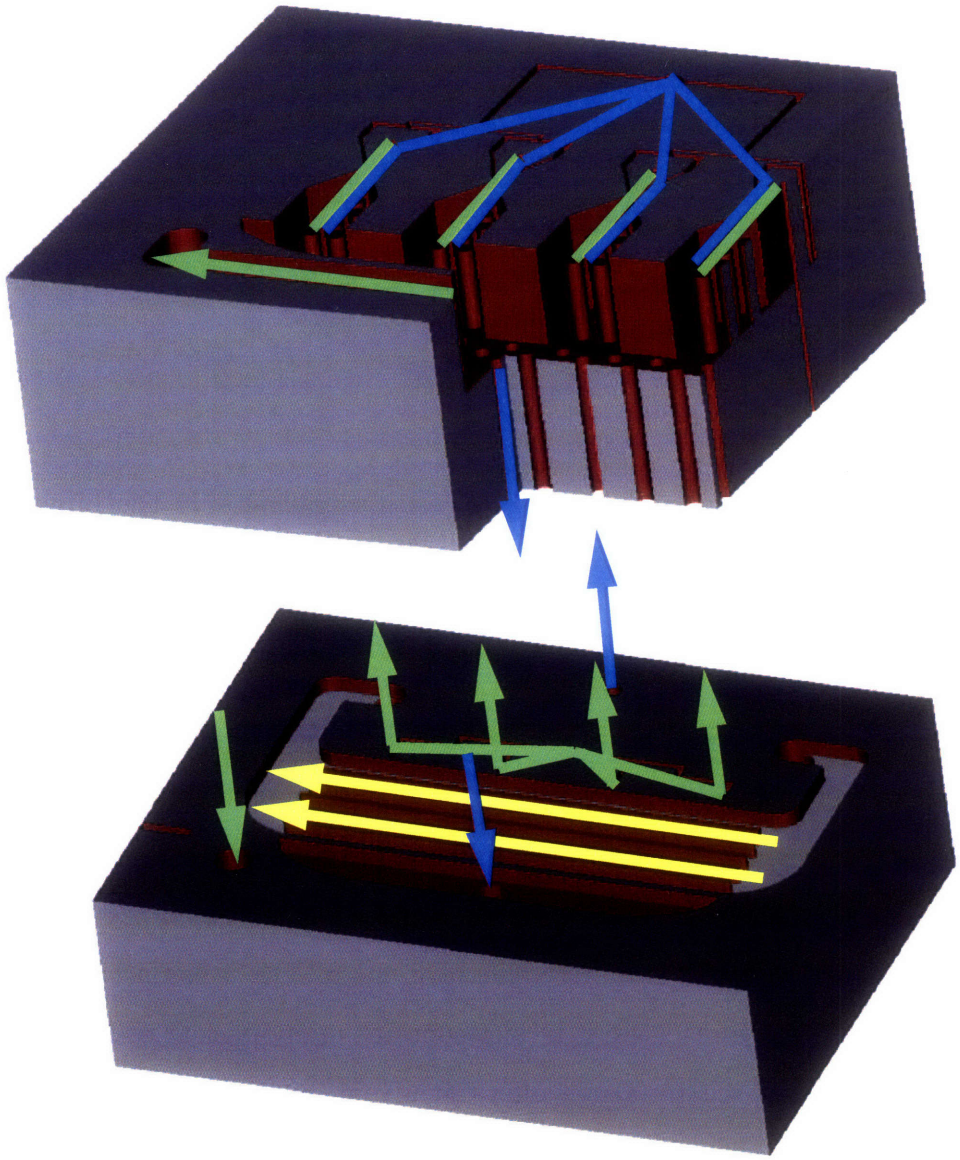

Figure 2-2: Deconstructed view of the silicon microSOG layers highlighting the gas (green), liquid (blue), and coolant (yellow) flow paths.

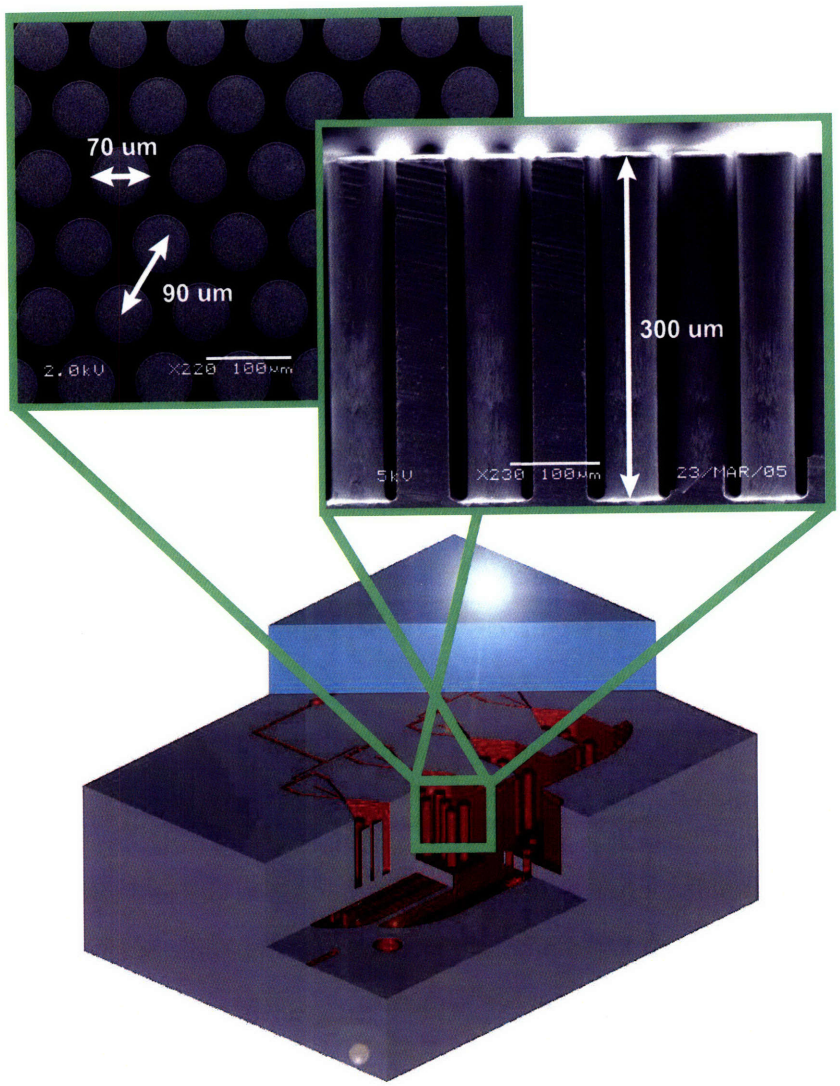

Figure 2-3: Schematic of microSOG with top and profile views of the posts in the reaction channels.

in Figure 2-3, are packed with thousands of individual posts, which are 70 μm in diameter and have a 90 μm pitch. This configuration results in a void fraction ϵ of 0.45, meaning that the other 55% of the the reaction channel volume is occupied by posts. The gas-liquid contact area is assumed to be 50 cm^{-1} based on the work of Losey et al; the actual value may be higher or lower based on geometrical differences between the current work and [43].

2.2.2 Bifurcated Inlets and Pressure Drop Channels

The parallelization of the reaction channels requires several additional features to ensure uniform reaction distribution. Specifically, bifurcated inlets and pressure drop channels are required to evenly divide reactants from the common inlet sources, which are placed on the lower wafer for ease of packaging and operation. The bifurcated inlets are responsible for delivery of the gas and liquid reactants from the common inlets to the inlets of the individual channels, and are carefully designed for symmetry. These features have respective depths and widths of 360 μm and 150 μm.

By having a much higher hydraulic resistance than the rest of the chip, the pressure drop channels control the amount of reactant that enters the reaction channels. Earlier work has demonstrated that parallelized reactors without pressure drop zones exhibited unpredictable and non-uniform behaviors, such as channels receiving no reactant and liquid being sucked backward through the gas manifold [22],[56]. If equal amounts of reactant flow into each channel, then both the flow regime behavior and the amount of $O_2(a)$ produced in each reaction channel should be identical. The pressure drop channel lengths for the liquid and gas phases are 2750 μm and 2428 μm respectively. The width and length for both phases were respectively 25 μm and 20 μm. The gas and liquid pressure drop channels are visible in Figure 2-1; the microSOG contains 32 and 64 gas and liquid pressure drop channels respectively.

2.2.3 Other Considerations

Several other issues exist regarding reactant mixing as it relates to the design. As was discussed in the Chapter 1, a critical percentage of O_2 produced needs to be in the singlet delta state at the SOG output for positive gain to occur in the COIL cavity. Additionally, as much Cl_2 as possible must be consumed by the end of the reaction channels, since any remaining molecules may deactivate the excited iodine species in the optical cavity. In an effort to satisfy these two requirements, the reaction channels were sized at a width of 630 μm, a depth of 340 μm, and a length of 6.1 mm. Finally, the microSOG needs to be chemically resistant to the reactants in order to be considered a serious alternative to macroscale SOGs. It is well known that KOH is an agressive etchant of silicon. Therefore, the internal features of the microSOG are coated with a 0.4 μm layer of pinhole-free silicon-rich silicon nitride. Since the etch rate of silicon nitride by KOH is negligibly small [58], the device is assumed to be impervious to KOH damage.

2.3 Separation

Both the gaseous and the remaining liquid products are present in the chip at the end of the reaction channels. At this point the microSOG needs to direct the former to the next stage of the laser and dispose of the latter. Separation between phases is accomplished by using capillary forces. A planar array of cylindrical pores, shown in Figure 2-4, is sized to draw in liquid without removing gas. This technology has been demonstrated in microreactors for other applications at atmospheric pressure [10], and has even been shown to operate independently of gravity. For the COIL application the microSOG operates at sub-atmospheric pressure, and the pores are expected to have a pressure drop ranging between 3-7 kPa across them. Each pore has a depth of 325 μm and a diameter of 20 μm. Like the reaction channel posts, the pores have a pitch of 90 μm. By comparing the volumetric flow capacity of one pore with the maximum BHP flow rate into the chip, it was determined that 2200 pores were needed to handle the flows proposed in [11]. However, the original design

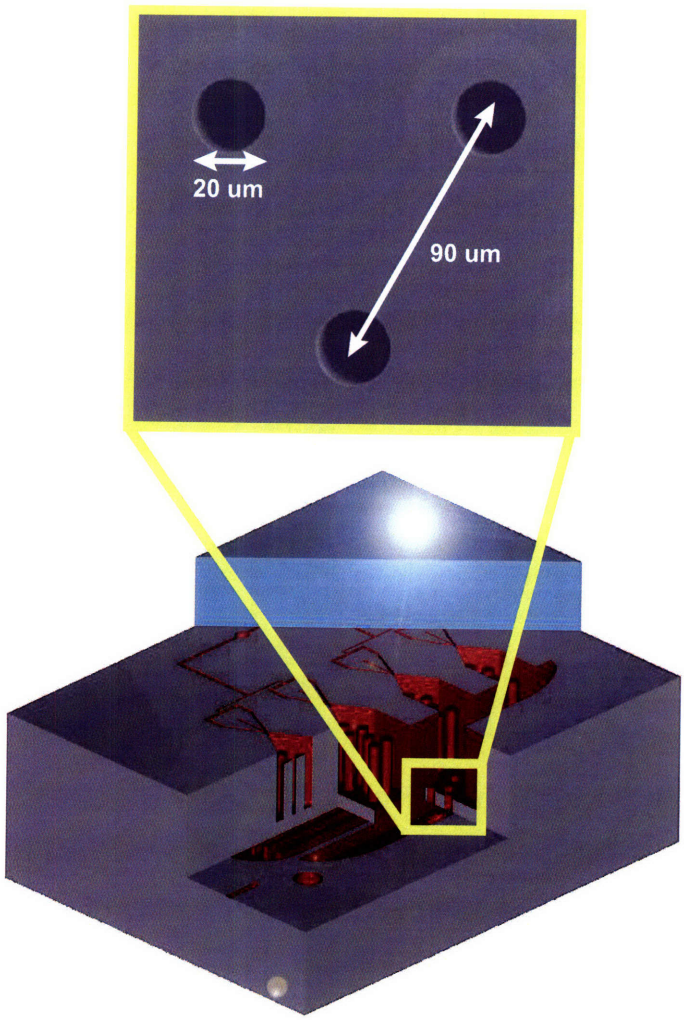

Figure 2-4: Illustration of the microSOG featuring the pores of the gas-liquid separator.

includes over 7600 because of initial concern about the success of the pore fabrication process. After the phases have been separated, the liquid exits through the lower layer while the gas exits through an elbowed exit path.

2.4 Heat Transfer

The final functional requirement for $O_2(a)$ generation is heat removal. The BHP solution needs to be kept near or below 0°C in the reaction channels in order to prevent both accelerated decomposition of H_2O_2 and the introduction of water vapor into the gas stream, which can cause iodine deactivation. The reaction of Equation 1.3 is highly exothermic, releasing 110 kJ/mol of heat along with its products. This enthalpy value results in a heat load of 8.8 W when applied to the maximum reactant flow rates proposed in [11]. Additionally, the ambient surrounding the chip acts as an a heat source.

The use of an insulating package, which is described in Chapter 4, prevents most of the ambient heat from entering the microSOG. The removal of heat associated with the $O_2(a)$ reaction is accomplished through the incorporation of cooling channels. Together with the reaction channels, the 19 cooling channels, which are 2.39 cm long and 300 μm wide and deep, form a cross-flow heat exchanger. Heat generated during the reaction is first transferred to the silicon through sidewall convection, then flows through the silicon via thermal conduction, and is finally removed from the device through sidewall convection into the cooling channels.

2.5 Fabrication Process

The first generation microSOG devices, one of which is shown in Figure 2-5, were fabricated in the Microsystems Technology Laboratories at MIT. The starting materials for the microSOG are three wafers, each 6 inches in diameter. The Pyrex wafer (Bullen Ultrasonics, Eaton, OH) was 2 mm thick while the two (DSP) p-Si <100> wafers (Silicon Quest, San Jose, CA) were 625 $\pm$ 20 μm thick. The Pyrex

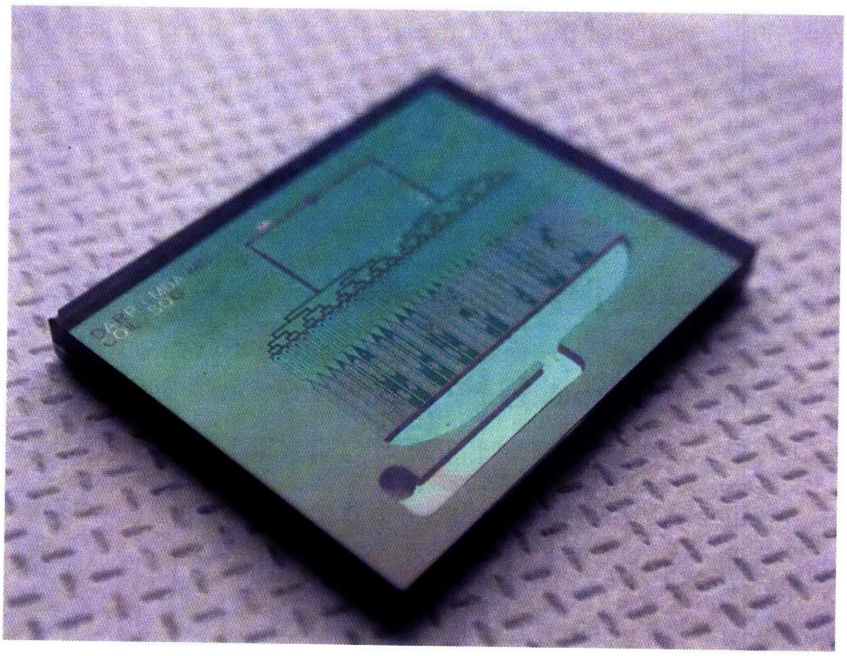

Figure 2-5: Photograph of first generation microSOG device

wafer is thicker than the other layers, providing greater stiffness and higher pressure capability. However, devices with Pyrex wafers 625 μm thick were also successfully fabricated and tested. The features in both layers are formed by Deep Reactive Ion Etching (DRIE). A nested mask process was used in the upper layer to produce features of differing depths (pressure drop and reaction channels). The microSOG is made chemically resistant through an LPCVD nitride deposition over the internal surfaces. Lastly, the layers were joined together through a combination of fusion and anodic bonding. With a die size of 3.6 cm x 2.8 cm, 8 devices were fabricated per wafer stack. The process is described in greater detail in [19] and in the appendices.

2.6 Summary

The device described in this section is designed to produce O_2(a), separate the resulting gas and liquid products, and operate at a temperature several degrees below 0°C. The middle layer contains a bifurcated inlet for liquid distribution, packed bed channels for the BHP-Cl_2 reaction, and thousands of pores for product separation. The lower layer contains the gas distribution system and cooling channels for heat

removal. The testing procedure and performance of the microSOG are discussed in Chapters 4 and 5.

Chapter 3

A Physical Model for the MicroSOG

This chapter presents a physical model explaining the operation of the microSOG. The physical behavior of the device can be broadly grouped into three domains: chemical, fluidic, and thermal. First the chemical kinetics in the reaction channels are discussed, followed by the various $O_2(a)$ deactivation mechanisms. Next, the hydraulics of the device features are detailed. Finally, a microSOG heat transfer model is presented.

3.1 Chemical Model

$O_2(a)$ is formed through the reaction of H_2O_2, KOH, and Cl_2, shown in reaction R1 of Table 3.1. The collection of reactions R1-R12 comprise the standard kinetics package used by the COIL research community [47]. The supporting sub-reactions of R1 (R1a-R1d) have been studied in detail [49], [33], [1]; it is believed that $O_2(a)$ forms from the decomposition of the chlorite ion, which is in turn formed by the reaction of the peroxide ion O_2H^- with HOOCl. Physically these reactions correspond to the events shown in Figure 3-1: the diffusion of Cl_2 molecules into the liquid phase, the formation of $O_2(a)$, and finally the diffusion of the newly-created $O_2(a)$ back into the

Table 3.1: Summary of SOG Kinetics

no.	Expression	Rate Coefficient ($cm^3/mol/s$)
R1	$H_2O_2 + 2KOH + Cl_2 \longrightarrow 2H_2O + 2KCl + O_2(a)$	N/A
R1a	$OH^- + H_2O_2 \longrightarrow O_2H^- + H_2O$	$k_{eq} \geq 10^4$
R1b	$O_2H^- + Cl_2 \longrightarrow HOOCl + Cl^-$	$k_1 = 2.7 \times 10^{10}$
R1c	$O_2H^- + HOOCl \longrightarrow ClO_2^- + H_2O_2$	k = infinity
R1d	$ClO_2^- \longrightarrow Cl^- + O_2(a)$	k = infinity
R1e	$O_2(a) \longrightarrow O_2(X)$	$k = 5 \times 10^5\ s^{-1}$
R2	$O_2(a) + O_2(a) \longrightarrow O_2(b) + O_2(X)$	$k_2 = 1.63 \times 10^7$
R3	$O_2(a) + O_2(a) \longrightarrow O_2(X) + O_2(X)$	$k_3 = 1.02 \times 10^7$
R4	$O_2(b) + O_2(X) \longrightarrow O_2(a) + O_2(X)$	$k_4 = 2.35 \times 10^7$
R5	$O_2(b) + H_2O \longrightarrow O_2(a) + H_2O$	$k_5 = 4.03 \times 10^{12}$
R6	$O_2(b) + Cl_2 \longrightarrow O_2(a) + Cl_2$	$k_6 = 9.03 \times 10^8$
R7	$O_2(b) + H_2O_2 \longrightarrow O_2(a) + H_2O_2$	$k_7 = 1.99 \times 10^{11}$
R8	$O_2(b) + He \longrightarrow O_2(a) + He$	$k_8 = 6.02 \times 10^6$
R9	$O_2(a) + O_2(X) \longrightarrow O_2(X) + O_2(X)$	$k_9 = 9.64 \times 10^5$
R10	$O_2(a) + H_2O \longrightarrow O_2(X) + H_2O$	$k_{10} = 2.41 \times 10^6$
R11	$O_2(a) + Cl_2 \longrightarrow O_2(X) + Cl_2$	$k_{11} = 3.61 \times 10^6$
R12	$O_2(a) + He \longrightarrow O_2(X) + He$	$k_{12} = 4.82 \times 10^3$

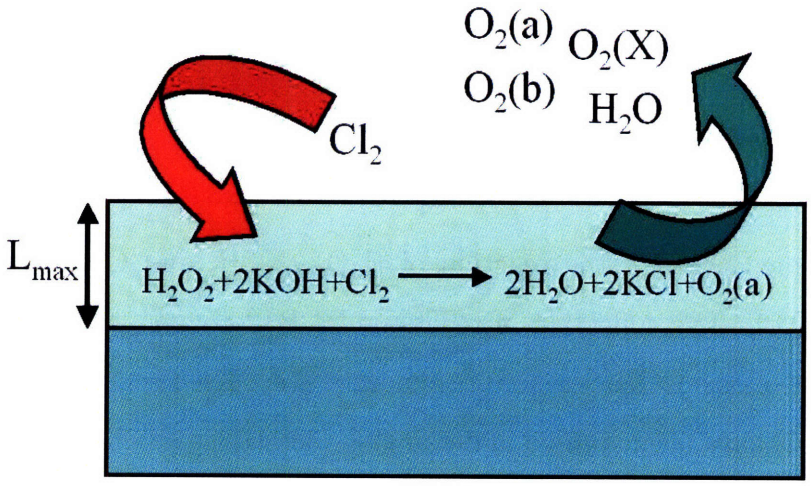

Figure 3-1: Cartoon depicting Cl_2 diffusion into BHP film, $O_2(a)$ reaction, and diffusion of the gaseous products out of the liquid.

gas phase. The mass transfer coefficient across the gas-liquid interface is

$$k_L = \sqrt{k_1 D^l_{Cl_2}[O_2H^-]}, \tag{3.1}$$

where k_1 is the R1b reaction coefficient, $D^l_{Cl_2}$ is the diffusivity of Cl_2 in BHP, and $[O_2H^-]$ is the peroxide ion concentration. The coefficient k_L, which has units of cm/sec, can be thought of as the velocity of Cl_2 atoms crossing into the liquid phase. The $O_2(a)$ reaction occurs in a thin layer of BHP just below the gas-liquid interface, the thickness of which is at most

$$L_{Cl_2} = \sqrt{\frac{D^l_{Cl_2}}{k_1[O_2H^-]}}, \tag{3.2}$$

and is also shown in Figure 3-1. Taking $D^l_{Cl_2}$ to be 10^{-5} cm^2/s and k_1 to be 2.7 x 10^{10} $cm^3/mol/s$ [11], the thickness of the BHP surface layer in which the chlorine reaction occurs is estimated to be about 10 nm. This layer needs to be as thin as possible to prevent liquid phase deactivation of $O_2(a)$, which has an aqueous lifetime of 2 μs. KOH is added to the liquid solution to catalyze the H_2O_2 decomposition into O_2H^-, which in turn raises the reaction rate $k_1[O_2H^-][Cl_2]$ and keeps L_{max} small.

The chemical model presented in this section is an outgrowth of the work in [11]. Wilhite begins with the standard COIL kinetics presented in [47] and recasts the chemical equations using an ideal plug (or piston) flow analysis. In an ideal plug flow reactor, a plug of reactant that enters the channel stays intact throughout its journey to the exit [45]. The plug flow reactor (PFR) approximation requires a uniform lateral velocity in the channel, and allows the reaction kinetics to be modeled with a uniaxial system of equations. For the microSOG case, the PFR assumption can be imagined with a multiphase plug of BHP, Cl_2, and He entering a reaction channel at time t_o. While there is diffusion and reaction across the gas-liquid interface within the plug, it maintains its shape and does not interact with any preceding or succeeding plugs

in the channel. The rate of Cl_2 consumption within a hypothetical plug is

$$r_{Cl_2} = k_L a[Cl_2]_{gas}, \tag{3.3}$$

where a is the gas-liquid contact area per unit volume. This equation can be further simplified by applying the ideal gas law for the chlorine, which yields

$$r_{Cl_2} = k_L \cdot a \cdot y_{Cl_2} \frac{P}{RT}, \tag{3.4}$$

where P is the total pressure, y_{Cl_2} is the chlorine molar fraction, R is the universal gas constant, and T is the temperature of the gas. The molar fraction of a species x is defined as the moles of x in the gas stream divided by the total number of moles in the gas stream. The rate of increase of O_2(a) in the gas phase is given by

$$r_{O_2(a)} = k_L \cdot a \cdot \chi_{detach} \cdot \frac{y_{Cl_2} \cdot P}{RT} + B\left(\frac{P}{N_t \cdot RT}\right)^2, \tag{3.5}$$

where N_t is the total number of moles of gas in the channel, and χ_{detach} is the percentage of generated O_2(a) that appears in the gas phase. The first term of Equation 3.5 represents the liquid phase processes, including Cl_2 conversion, while the second term reflects the gas phase deactivation mechanisms described in Table 3.1. The coefficient B in the second term can be expressed as

$$\begin{aligned} B = -2k_2 y_{O_2(a)}^2 \; - 2k_3 y_{O_2(a)}^2 + \\ k_4 y_{O_2(b)} y_{O_2(X)} + k_5 y_{O_2(b)} y_{H_2O} + \\ k_6 y_{O_2(b)} y_{Cl_2} + k_7 y_{O_2(b)} y_{H_2O_2} + \\ k_8 y_{O_2(b)} y_{He} - k_9 y_{O_2(a)} y_{O_2(X)} - \\ k_{10} y_{O_2(a)} y_{H_2O} - k_{11} y_{O_2(a)} y_{Cl_2} - \\ k_{12} y_{O_2(a)} y_{He}, \end{aligned} \tag{3.6}$$

where y_x is the molar fraction of the species x in the gas stream and each k coefficient is the particular reaction constant between two specific species as given in Table 3.1.

The first term is similar to the chlorine consumption described in Equation 3.4, but with the addition of the factor χ_{detach}.

The concept of detachment yield arises from O_2(a) molecules deactivating as they diffuse across the reaction depth to the gas-liquid interface, and O_2(a) molecules in the gas phase deactivating upon re-diffusion into the liquid phase. Several approaches to determining the detachment yield have been described in the literature [14], [54], [13], [16], [4]. These approaches produce similar but not identical estimates of detachment yield by describing similar mechanisms in various levels of detail. In all of these approaches, uncertainties in the physical constants (for example as reported in [20], [54], [49] [50], [23], [24]) can result in significant uncertainties in the calculated detachment yields. In the present work, an initial estimate of the O_2(a) loss due to liquid phase deactivation is made by comparing the timescale for O_2(a) quenching in the liquid to the timescale for O_2(a) diffusion back through the reaction layer [54]. Again, assuming that the diffusivities of oxygen and chlorine in BHP are 10^{-5} cm^2/s, the deactivation timescale is 40 times greater than the diffusion time, suggesting a loss of about 2.5% of the O_2(a) en route to the liquid/gas interface. A more detailed approximation of χ_{detach} was obtained using the method of [16]. In this approach the detachment yield is defined as

$$\chi_{detach} = \frac{R_{O_2}^{liq} \cdot L_{O_2}}{R_{O_2}^{T} \cdot (L_{O_2} + L_{Cl_2})}, \tag{3.7}$$

where L_{O_2} is the characteristic diffusion length for O_2, and $R_{O_2}^{T}$ and $R_{O_2}^{liq}$ are respectively the total and liquid mass transport resistances of O_2. This expression takes into account both the deactivation by R1e and the surface detachment processes [16], [4], [14]. Using the same values for the diffusivities that are used above, this method produces a χ_{detach} of 94%; alternatively, using the parameter values given in [16] would produce a χ_{detach} of 90%. These methods suggest that the detachment yield is in the range of 90% to 97.5%. Although a 5% to 10% yield loss would correspond to a large difference in O_2(a) concentration in the reaction channels themselves, the change in concentration at the measurement point is only on the order of 10^{14} cm^{-3} because

of gas phase deactivation. It will be seen that this difference is below the detection limit of the optical emission diagnostic described in Chapters 4 and 5. As a result the model used here approximates $\chi_{detach} = 1$.

The pressure drop across the reaction channels is modeled using the Ergun equation [9], written as

$$\frac{dP}{dz} = -\frac{F_t \cdot RT}{D_p \cdot P \cdot a_c} \cdot \left(\frac{1-\epsilon}{\epsilon^3}\right) \cdot \left[\frac{150 \cdot (1-\epsilon) \cdot \mu_g}{D_p} + 1.75 \cdot MW_g \cdot \frac{F_t^2 \cdot RT}{P \cdot a_c}\right] \tag{3.8}$$

for the gas phase and by

$$\frac{dP}{dz} = -\frac{v_l^o}{D_p} \cdot \left(\frac{1-\epsilon}{\epsilon^3}\right) \cdot \left[\frac{150 \cdot (1-\epsilon) \cdot \mu_l}{D_p} + 1.75 \cdot \rho_l \cdot v_l^o\right] \tag{3.9}$$

in the liquid phase, where z is the distance along the reaction channel, F_t is the total molar flow rate (constant), D_p is the packing diameter in the channels, a_c is the cross sectional area of the reaction channels, ϵ is the void fraction, μ_g is the viscosity of the gas, v_l^o is the liquid phase velocity, and MW_g is the molecular weight of the gas. The overall multiphase pressure drop per unit reaction length is given by the correlation of Larkins et al. [25], which is

$$log_{10}\left(\frac{\frac{dP}{dz}}{\frac{dP}{dz_g} + \frac{dP}{dz_l}}\right) = \frac{0.146}{(log\chi)^2 + 0.666}, \tag{3.10}$$

where

$$\chi = \left(\frac{\frac{dP}{dz}}{\frac{dP}{dz}}\right)^{0.5}. \tag{3.11}$$

Assuming ideal plug flow in the channels, the relationship between molar flow rate

(F) and species production (r) for O_2(a) is

$$\frac{1}{\epsilon_g \cdot a_c} \cdot \frac{dF_{O_2(a)}}{dz} = v_l \cdot \frac{d[O_2(a)]}{dz} = r_{O_2(a)} \tag{3.12}$$

where ϵ_g is the fraction of the volume in the reaction channels that is occupied by the gas phase. As outlined in [11], substituting Equation 3.5 into Equation 3.12 yields

$$\frac{dF_{O_2(a)}}{dz} = \epsilon_g \cdot a_c \cdot a \cdot k_l \cdot \frac{y_{Cl_2} \cdot P}{RT} + \epsilon_g \cdot a_c \cdot B\left(\frac{P}{F_t RT}\right)^2 \tag{3.13}$$

Because of the interrelated chemical relationships described in Table 3.1, it is necessary to keep track of species other than O_2(a) as a function of reactor length. Following the same method used to obtain Equations 3.13, the expressions for $[O_2H^-]$, Cl_2, O_2(b), O_2(X), H_2O, and H_2O_2 are

$$\frac{d[O_2H^-]}{dz} = -\frac{\epsilon_l \cdot a \cdot \sqrt{k_l \cdot [O_2H^-] \cdot D_{Cl2}}}{v_l^o} \cdot \frac{P \cdot F_t}{R \cdot T} \tag{3.14}$$

$$\frac{dF_{Cl2}}{dz} = -\epsilon_g \cdot a_c \cdot a \cdot \sqrt{k_l \cdot [O_2H^-] \cdot D_{Cl2}} \cdot \frac{F_{Cl2} \cdot P}{F_t \cdot RT} \tag{3.15}$$

$$\frac{dF_{O_2(b)}}{dz} = \epsilon_g \cdot a_c \cdot C\left(\frac{P}{F_t RT}\right)^2 \tag{3.16}$$

$$\frac{dF_{O_2(X)}}{dz} = \epsilon_g \cdot a_c \cdot D\left(\frac{P}{F_t RT}\right)^2 \tag{3.17}$$

$$\frac{dF_{H_2O}}{dz} = k_g \cdot a \cdot \frac{P}{RT} \cdot \left(\frac{x^l_{H2O} \cdot \alpha_{H2O} \cdot P^{sat}_{H2O}}{P} - \frac{F_{H2O}}{F_t}\right) \tag{3.18}$$

$$\frac{dF_{H_2O2}}{dz} = k_g \cdot a \cdot \frac{P}{RT} \cdot \left(\frac{x^l_{H2O2} \cdot \alpha_{H2O2} \cdot P^{sat}_{H2O2}}{P} - \frac{F_{H2O2}}{F_t}\right), \tag{3.19}$$

where

$$C = k_2 y^2_{O_2(a)} - k_4 y_{O_2(b)} y_{O_2(X)} - k_5 y_{O_2(b)} y_{H_2O} - k_6 y_{Cl_2} y_{O_2(b)} - k_7 y_{Cl_2} y_{O_2(b)} - k_8 y_{O_2(b)} y_{He} \tag{3.20}$$

and

$$D = k_2 y_{O_2(a)}^2 + 2k_3 y_{O_2(a)}^2 + k_9 y_{O_2(a)} y_{O_2(X)} + k_{10} y_{O_2(b)} y_{H_2O} + k_{11} y_{Cl_2} y_{O_2(a)} + k_{12} y_{O_2(a)} y_{He}. \quad (3.21)$$

Equation 3.14 is cast in terms of concentration rather than molar flow rate because the peroxide ion concentration is the quantity needed to calculate k_L in Equation 3.1. In order to solve for molar flow rate as a function of reactor length, Equations 3.13 - 3.19 are implemented as coupled ordinary differential equations in MATLAB. The equations are then solved using the Runge-Kutta method for moderately stiff systems. For the microSOG geometry described in Chapter 3, the species profiles are shown in

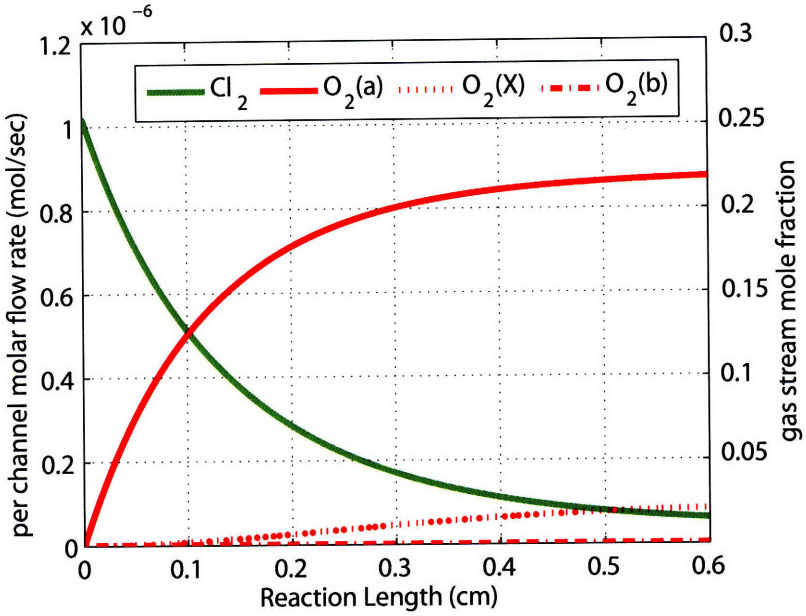

Figure 3-2: Species profile per reaction channel length, assuming Q_{gas} of 175 sccm, Q_l of 1 ml/min, and a gas outlet pressure of 100 torr.

Figure 3-2. The per-channel molar flow rate is plotted on the left axis, while the right axis shows the results in terms of mole fraction. Most of the gas stream is comprised of helium; its mole fraction is constant due to its properties as an inert noble gas. As expected, the Cl_2 flow rate declines as the O_2 profiles increase. Additionally, the O_2(b) flow rate is low due to its rapid deactivation described in R5 of Table 3.1. Figure 3-3 illustrates the rise in the H_2O and H_2O_2 in the gas phase as a function of

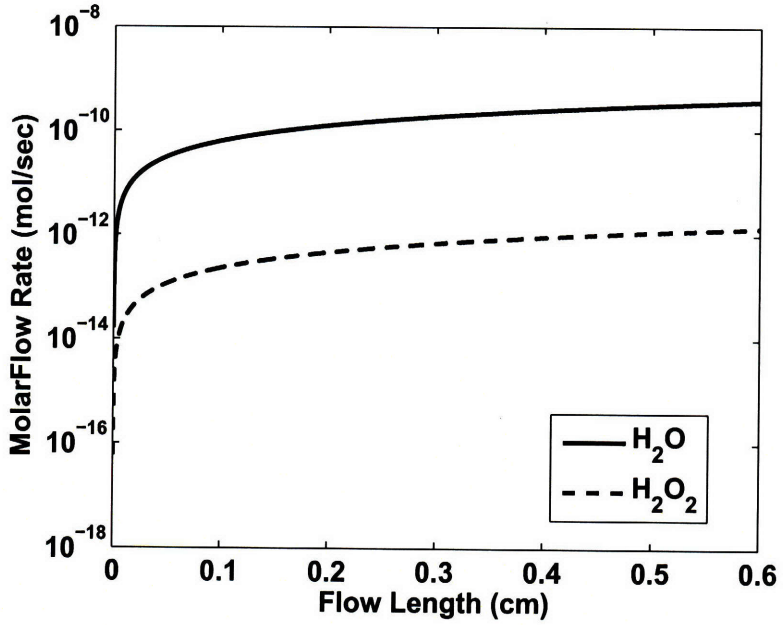

Figure 3-3: Per-channel water and hydrogen peroxide gas molar flow rates as function of reactor length.

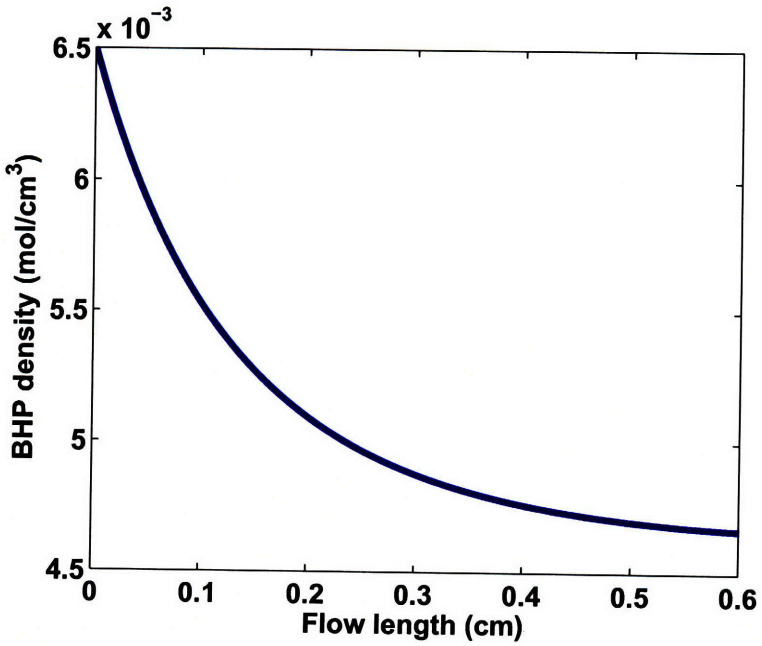

Figure 3-4: Liquid-phase peroxide ion density in the BHP as a function of reactor length.

reaction channel length; the molar flow rates of these two species are still well below those of Cl_2 and O_2. The change in the liquid phase O_2H^- concentration is shown in Figure 3-4. It is clear from the plot that BHP solution is not fully depleted by the end of the reaction channels, which is consistent with Cl_2 being the limiting reagent of the O_2(a) reaction. Figures 3-2 - 3-4 all assume a microSOG outlet pressure of 100 torr.

3.1.1 Deactivation Model

Because the amount of O_2 that remains in the singlet delta state is critically important to efficiently transfer energy to I atoms in a COIL system, it is important to keep track of O_2(a) deactivation upon collision with other species. The reactions that are most relevant to deactivation are R2, R3, and R5 in Table 3.1, along with sidewall deactivation, modeled as

$$\begin{aligned} O_2(a) + wall &\longrightarrow O_2(X) + wall, \\ k_{wall} &= 0.25 \cdot \zeta \cdot v_{th} \cdot (S/V), \end{aligned} \tag{3.22}$$

where ζ represents the probability of O_2(a) deactivating during a single wall collision, v_{th} represents the thermal velocity, and (S/V) is the surface area to volume ratio of the volume containing the gas. Combining these four equations yields

$$\frac{O_2(a)}{dt} = -2(k_2 + k_3)[O_2(a)]^2 + k_5[O_2(b)][H_2O] - k_{wall}[O_2(a)]. \tag{3.23}$$

which relates the change in [O_2(a)] to the various reaction rate coefficients. Equation 3.23 can be simplified by recognizing that the reaction rate of R5 in Table 3.1, k_5[O_2(b)][H_2O], greatly exceeds the reaction rates in R2 and R3, meaning that O_2(b) decays into O_2(a) almost instantaneously with respect to the timescales governing O_2(a) deactivation. This observation is consistent with the low values of O_2(b) in Figure 3-2. If the O_2(b) profile is then approximated as constant, then its rates of

creation and destruction can be equated. This new expression,

$$k_5[O_2(b)][H_2O] = k_2[O_2(a)]^2, \tag{3.24}$$

can be substituted into Equation 3.23, which now simplifies to

$$\frac{d[O_2(a)]}{dt} = -(2k_3 + k_2)[O_2(a)]^2 - k_{wall}[O_2(a)]. \tag{3.25}$$

When Equation 3.25 is integrated and solved, the solution is given by

$$[O_2(a)](t) = \frac{k_{wall}[O_2(a)]_o}{(k_{wall} + k^*[O_2(a)]_o)e^{k_{wall}t} - k^*[O_2(a)]_o}, \tag{3.26}$$

which models the decay rate of the O_2(a) concentration as a function of time t, $[O_2(a)]_o$ (the concentration at time t=0), k_{wall}, and k^*, which is equal to $2k_3 + k_2$. For geometries and materials resulting in low k_{wall} values, Equation 3.26 further simplifies to

$$[O_2(a)](t) = \frac{[O_2(a)]_o}{1 + k^*[O_2(a)]_o t}. \tag{3.27}$$

This equation is plotted in Figure 3-5 for values of $[O_2(a)]_o$ ranging from 5 x 10^{16} cm^{-3} to 5 x 10^{18} cm^{-3}.

3.2 Fluidic Model

One of the main objectives of the microSOG design presented in Chapter 3 is to achieve operational uniformity across the 32 reaction channels. The following sections will discuss the hydrodynamics of the pressure drop and reaction channels and connect them to the observed flow regime behaviors. Specifically, the importance of allowing the pressure drop channels to dominate the hydraulics will be highlighted. Later, the operation of the gas-liquid separator will be discussed.

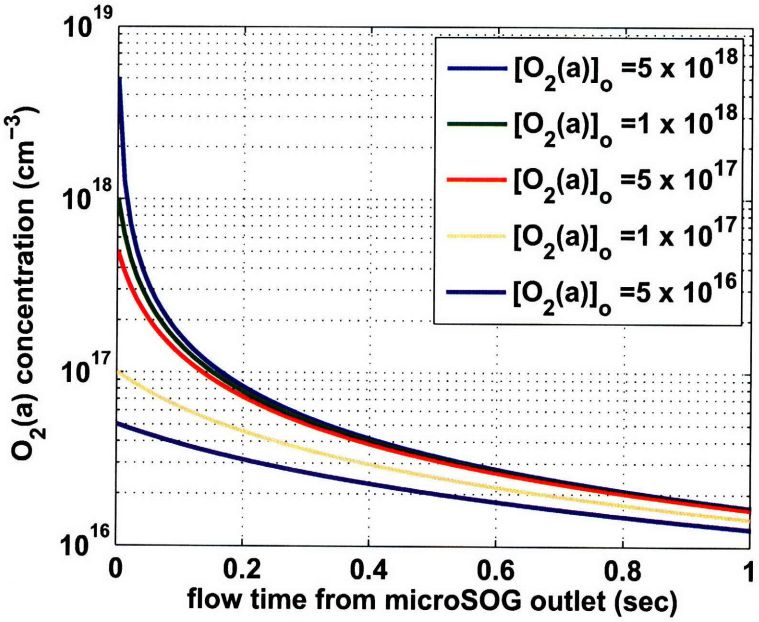

Figure 3-5: Decay of $O_2(a)$ concentration as a function of time.

3.2.1 Hydrodynamics of a Parallelized Reactor

The pressure drop channels are tasked with regulating the gas and liquid flow rates into the subsequent reaction channels. Because of the complex behavior of the reaction channels, described in Equations 3.8 - 3.10, it is desirable for the pressure drop channels, which have somewhat simpler hydrodynamics, to dominate the system hydraulics. Well-designed pressure drop channels should exert enough control over the chip to force all 32 reaction channels to behave the same way.

For a rectangularly cross-sectioned channel the volumetric flow rate is

$$Q = \frac{W \cdot h^3 \cdot \Delta P}{12\mu L}\left[1 - \frac{192 \cdot h}{\pi^5 \cdot W}\sum_{n=0}^{\infty}\frac{tanh((2n+1)\frac{\pi \cdot W}{2 \cdot h})}{(2n+1)^5}\right], \tag{3.28}$$

where W, h, and L are the respective width, height, and length of the channel, μ is the reactant viscosity, and ΔP is the resulting pressure drop. Because the infinite series term has a quintic dependence, truncating it to a few terms can give an excellent approximate result. An even simpler expression,

$$Q = \frac{W^4 \Delta P}{12\mu \cdot L} \cdot 0.42173 \tag{3.29}$$

is obtained for designs in which h equals W. It is important to note that both Equations 3.28 and 3.29 assume fully-developed, laminar, and incompressible flow. Laminar flow, characterized by a relatively slow velocity, uniform streamlines, and a thin boundary layer, is defined as having a Reynolds number

$$Re = \frac{\rho \cdot v \cdot L}{\mu} \tag{3.30}$$

below 2300. Incompressibility refers to the assumption of constant density in the fluid. At high velocities, defined by the Mach number as

$$M = \frac{v}{v_{sound}} \geq 0.3, \tag{3.31}$$

this approximation can no longer be made. Compressible flow is more difficult to model because the fluid density (and thus the volumetric flow rate) is different at every point in the channel.

Finally, at the inlet of each pressure drop channel, there is a transitional region in which the flow profile is not yet fully-developed. This entrance length is

$$L_e \approx 0.06 \cdot Re \cdot D \tag{3.32}$$

and is usually defined in terms of channel diameters; for Equation 3.29 to be valid, the channel needs to be longer than L_e. In summary, the hydraulics of the pressure drop channels have been shown to be much simpler than those of the reaction channels. Therefore, by ensuring that the majority of the pressure drop in the microSOG falls across the pressure drop channels, the amount of reactant flowing into the reaction channels becomes easily determined and independent of small variations in reaction area geometry.

3.2.2 Reaction Channel Flow Regime Model

The preceding discussion is important because it motivates the discussion of fluid behavior in the reaction channels. The observed flow behavior is dependent on the

forces in the channel and the proportions of gas and liquid flow (Q_g and Q_l), and can be categorized into five possibilities:

- Spray - This behavior occurs at high Q_g:Q_l ratios and is characterized by sparse liquid droplets being blown down the channel length by abundant gas flow. The gas-liquid interfacial area occurs on the outer surface of the droplets, and is relatively small;

- Plug - This behavior occurs at intermediate Q_g:Q_l ratios and is characterized by alternating plugs of gas and liquid phase reactants flowing through the reaction channels. The O_2(a) reaction for this regime takes place at the boundary between the plugs;

- Annular - In this regime the driving forces overwhelm the resistive forces, and the liquid in the channels is pushed to the outer walls. Here the size of the gas-liquid interface is directly proportional to the reactor geometry;

- Churn - In this region the reactant flow is highly unsteady and unpredictable;

- Bubbling - When the resistive forces (mainly surface tension) are dominant, the liquid reactant will minimize the gas-liquid interface in order to lower the expended free energy. The lowest-energy interface in this regime corresponds to gas bubbles appearing in a channel otherwise flooded with liquid, which occurs at low Q_g:Q_l ratios.

A sixth possibility exists in which the liquid phase flows at the bottom of the reaction channel (due to gravity) and the gas phase flows directly above it. However, the dimensions of the microSOG ensure that the effects of gravity are dominated by the surface tension. This claim is supported by the Bond number,

$$Bo = \frac{\rho \cdot g \cdot h}{\sigma}, \tag{3.33}$$

where ρ and σ are the density and surface tension of the liquid respectively, and g is the acceleration of gravity. For the dimensions of the original microSOG, Bo is

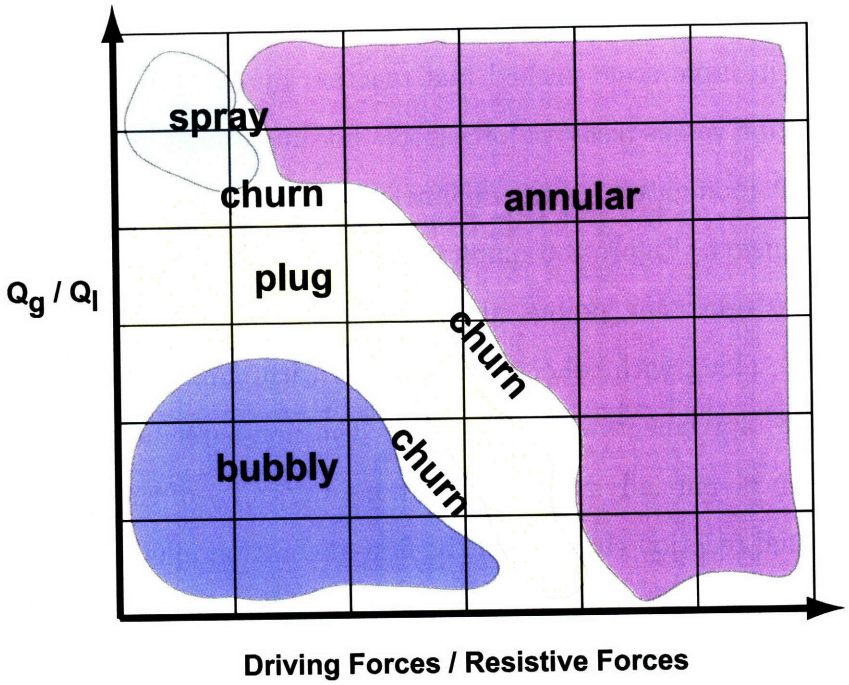

Figure 3-6: Conceptual illustration of flow regime vs. operating point.

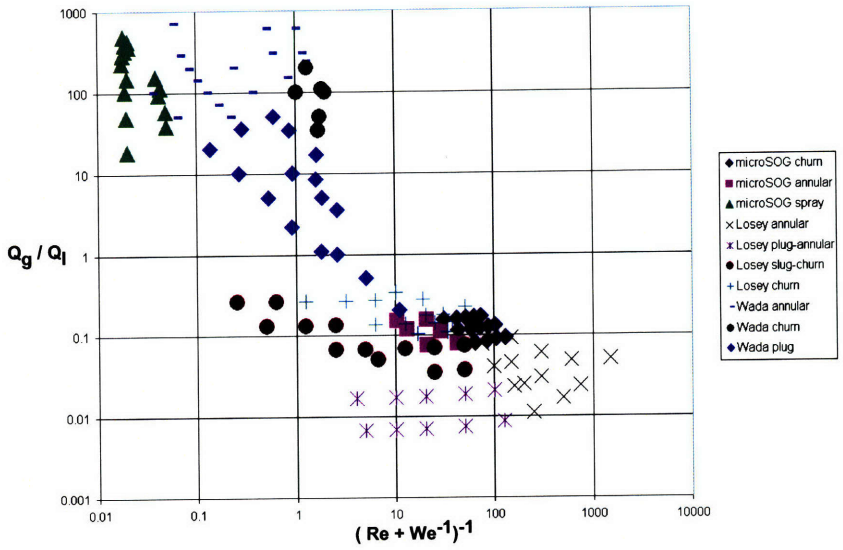

Figure 3-7: Flow map for the present work and other microreactors [56] [43] [12].

calculated to be 0.016, meaning that surface tension in the channels dominate over gravitational forces by two orders of magnitude. The flow regimes described above were mapped in large scale packed bed reactors by Talmor as a function of Q_g:Q_l ratios and driving versus resistive forces [53]. For microreactors "driving forces" refers to the reactant momentum in the channel, while the "resistive forces" are viscosity and surface tension. Figure 3-6 qualitatively illustrates how the different behaviors map to various operating points. Figure 3-7 contains actual flow regime data for the microSOG, along with other microreactors with similar dimensions. Figure 3-7 mostly exhibits agreement with Figure 3-6; the non-agreement of the annular and churn flows can be partially attributed to non-uniformity of the reactant distribution to the individual reaction channels of the first-generation microSOG. This flaw in the original design is addressed in the redesign proposed in Chapter 6. Talmor developed modified forms for the Reynolds and Weber numbers,

$$Re_{Talmor} = \frac{D_h(L+G)}{\mu_{lg}} \tag{3.34}$$

and

$$We_{Talmor} = \frac{D_h(L+G)^2 v_{lg}}{\sigma}, \tag{3.35}$$

to describe the multiphase nature of the flow. The parameters L and G refer to the liquid and gas superficial mass velocities, defined as the mass flow rate divided by the cross-sectional area of a channel. The terms v_{lg}, μ_{lg}, and D_h refer to the composite reactant velocity, composite viscosity, and hydraulic diameter respectively, and are defined in [53] as

$$\mu_{LG} = \mu_L \cdot \frac{L/G}{1+L/G} + \mu_G \cdot \frac{1}{1+L/G}, \tag{3.36}$$

$$v_{LG} = v_L \cdot \frac{L/G}{1+L/G} + v_G \cdot \frac{1}{1+L/G}, \tag{3.37}$$

and

$$D_h = \frac{2\epsilon W_{chan}}{2+3(1-\epsilon)(W_{chan}/D_p)}. \tag{3.38}$$

Because the microSOG operates with excess helium buffer flow, the operating points of interest lie in the upper left quadrant of Figure 3-7.

3.2.3 A Geometric Contact Area Model

Figure 3-7 is useful for determining the flow regime at a given operating point, which greatly affects the gas-liquid contact area in the reaction channels. Of the six flow regimes described in the previous sections, only three have high enough contact area to be useful in multiphase reactions. These regimes are plug, churn, and annular, and they are illustrated in Figure 3-8. The best and worst case wetting fronts for each regime are highlighted in orange and green respectively.

For plug flow the post pitch is identical for the both the straight and zigzag wetting profiles. Therefore, the zigzag profile offers more contact area since its total meniscus length is twice the length of the straight profile. The contact area per unit volume is

$$a_{plug,min} = \frac{2n}{\epsilon \cdot L_{chan}} \cdot \left(\frac{\delta - D_p}{\delta} \right) \tag{3.39}$$

for the straight wetting front and

$$a_{plug,max} = \frac{4n}{\epsilon \cdot L_{chan}} \cdot \left(\frac{\delta - D_p}{\delta} \right) \tag{3.40}$$

for the zigzag wetting front, where D_p is the post diameter, n is the number of plugs present, and δ is the pitch between posts. It is important to note that Equations 3.39 and 3.40 only differ by a factor of two.

The posts in the reaction channels are arranged in an ABAB packing, forming the points of equilateral triangles with their nearest neighbors. As a result, the meniscus length is set by the post pitch δ for the zigzag profile in the annular regime. However the post pitch in the vertical direction has the larger value of $\delta \cdot \sqrt{3}$, making the meniscus length longer for the vertical wetting profile. The contact area per unit

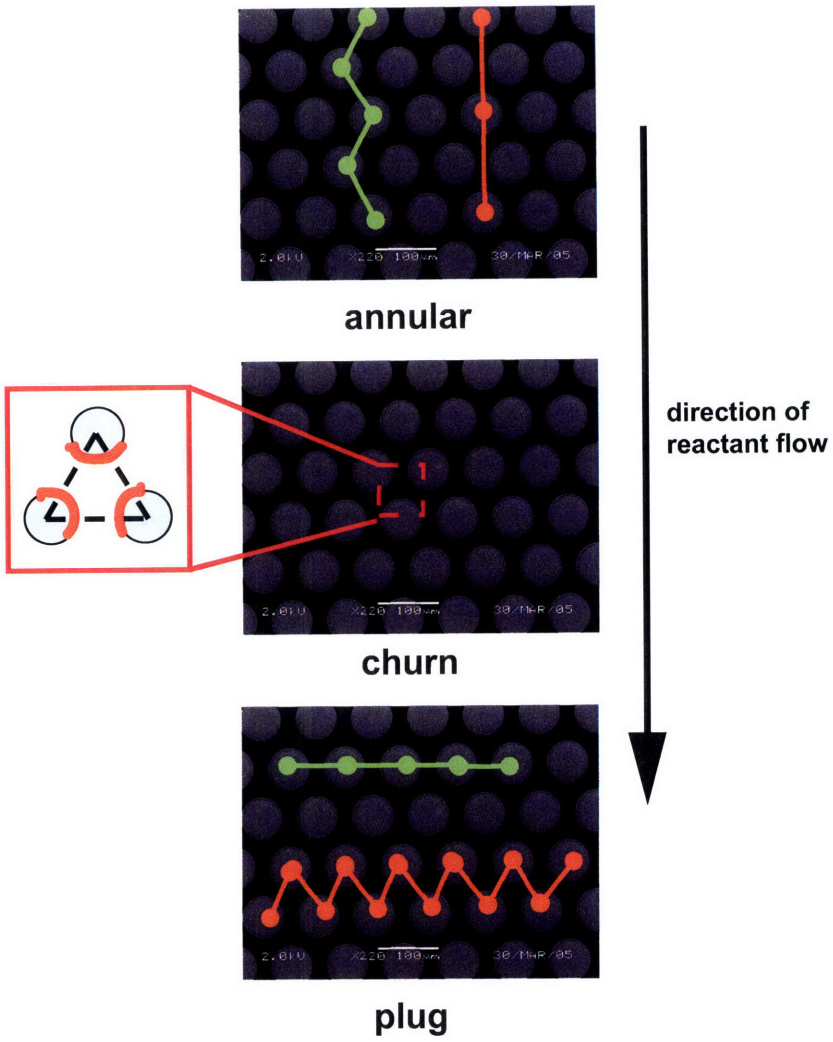

Figure 3-8: Illustration of the best- (orange) and worst- (green) case scenario wetting fronts for the plug, annular, and churn flow regimes.

Table 3.2: Expected contact area per unit volume.

regime	a (cm^{-1}) min	a (cm^{-1}) max
plug	5	10
annular	20	40
churn	0	170

volume is

$$a_{annular,min} = \frac{4(\delta - D_p)}{\epsilon \cdot W_{chan}.\delta\sqrt{3}} \tag{3.41}$$

for the zigzag profile and

$$a_{annular,max} = \frac{2(\delta\sqrt{3} - D_p)}{\epsilon \cdot W_{chan}\delta\sqrt{3}}. \tag{3.42}$$

for the straight profile.

The churn regime by far has the highest potential contact area per unit volume, corresponding to the entire post area being wetted by a thin film of BHP. However, this situation is unlikely because at most operating points capillary forces should hold-up some of the BHP into the spaces between the posts. The contact area per unit volume for the churn regime,

$$a_{churn} = X \cdot \frac{2(1-\epsilon)\pi D_p}{\delta^2\sqrt{3}}, \tag{3.43}$$

is scaled by an efficiency factor X, which can range from 0 to 1. Table 3.2 reports the expected values of a for the plug, annular, and churn flow regimes, based on the reactor geometry described in Chapter 2 and helium-water characterizations of the fabricated devices.

3.2.4 Gas - Liquid Separator

Multiphase separation has been demonstrated in other microdevices [10], [40], the phenomenon is explained here. The behavior of the gas-liquid separator can be understood by dividing it into transient and steady-state timescales. This division is

illustrated in Figure 3-9.

At steady state stationary plugs exist in the pores. These plugs are formed when the liquid by-products get sucked in due to surface tension effects, which implies that the inner surface of the pore is wettable. The relationship between the angle θ at which the liquid contacts the pore's opening, the surface tension σ, the pore diameter D_c, and the pressure drop across the pore is given by

$$\Delta P_{ss} = \frac{4\sigma cos\theta}{D_c}. \tag{3.44}$$

In order for the separator to block gas from flowing through the pores the contact angle θ must be greater than zero. This constraint results in a maximum pressure drop P_{max} that can fall across the pores (when θ is equal to zero). For 20 μm wide capillaries and given the surface tension of water (72 dynes/cm), the maximum pressure drop that the meniscus can withstand is 14 kPa. Fortunately since the microSOG gas outlet pressure is designed for values as low as 7 kPa, the pores are only expected to have a 3 kPa drop across them.

On the transient time scale the dynamic wetting front of the reaction channel flow floods the pores with more fluid. This effect is also shown in Figure 3-9. The force of the excess fluid flow creates an impulse of pressure drop across a given pore that forces liquid out through its lower end. The dynamic flooding events occur on the same timescale as the reactant residence time in the reaction channels, which is approximately one one-hundredth of a second for a gas flow rate of 200 sccm. As a result of the superposition of the transient and steady state cases, the gas-liquid separator is able to allow liquid to pass while screening out the gaseous products.

The pressure drop across the pores can be related to liquid flow rate through Hagen-Poiseuille equation if steady state, fully developed flow is assumed and the liquid is Newtonian, with pressure losses produced by viscosity. In this case the volumetric flow rate Q through each capillary is given by [26]

$$Q = \frac{\pi \cdot P_{ss} D_c^4}{128\mu \cdot L_{pore}}, \tag{3.45}$$

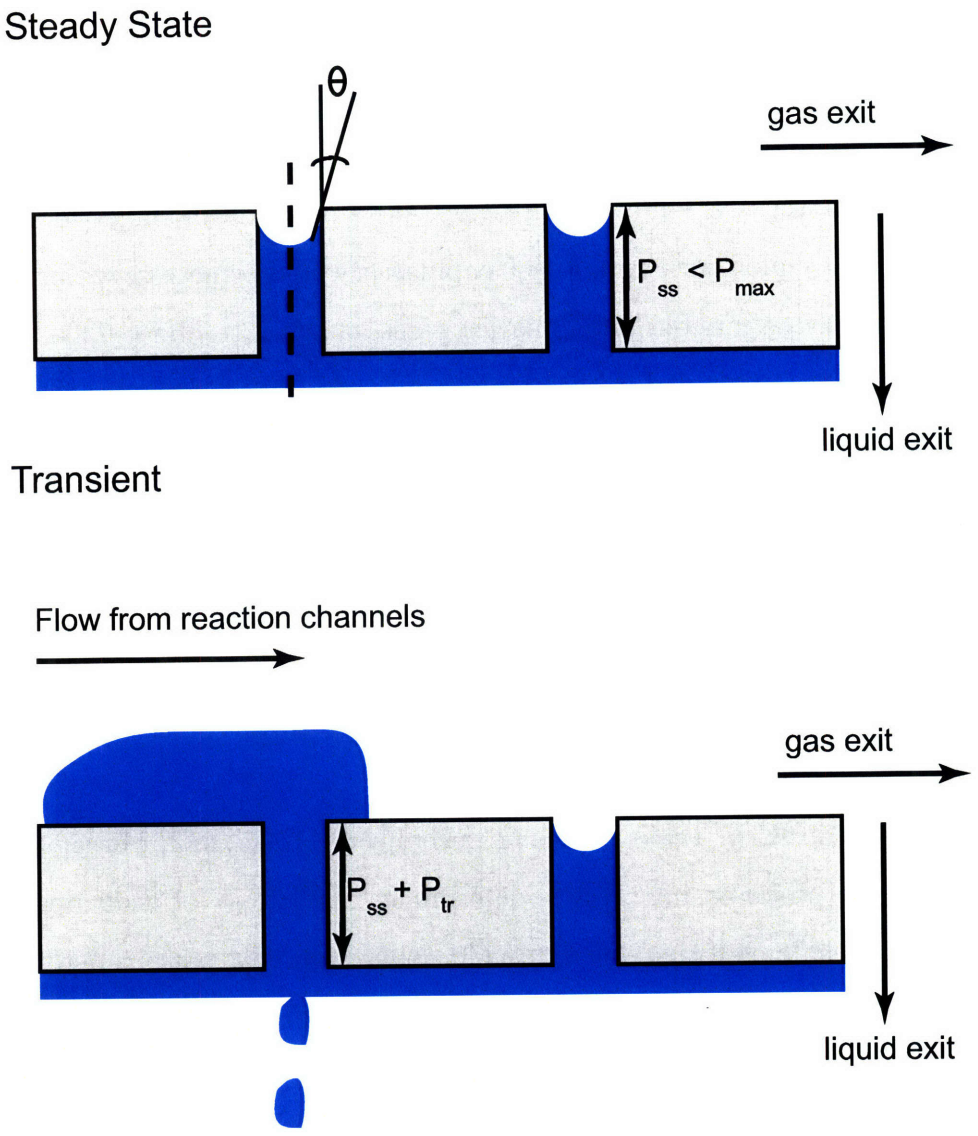

Figure 3-9: Illustration of the gas liquid separator pores (side view) in the steady-state and transient timescales.

where L_{pore} is the pore length. For a given pressure drop across the separator, the number of pores needed to transport the liquid by-products can be found by dividing the total liquid molar flowrate Q_t by Q. Q_t is expressed as

$$Q_t = \frac{10 Q_g y_{Cl_2}}{[O_2H^-]} \tag{3.46}$$

where Q_g is the total gas molar flow rate and y_{Cl_2} is the chlorine fraction of the entering gas stream. Equation 3.46 assumes a 10:1 peroxide ion to Cl_2 ratio. For a gas flow rate of 50 sccm, a 3 kPa pressure drop, and a peroxide ion molar concentration $[O_2H^-]$ of 6.5×10^{-3} mol/cm^3, around 430 capillaries would be necessary; for a gas flow rate of 250 sccm, the number of capillaries necessary rises to about 2200. However, more than 7000 were included in the actual devices due to concerns about how many functioning pores would be successfully produced in the DRIE steps. Also, it was desired to have some redundancy in the separator in case clogging occurred during testing of the chip.

3.3 Thermal Model

The O_2(a) reaction R1 in Table 3.1 has an enthalpy of 110 kJ/mol. For the maximum He:Cl_2 flow rate proposed in [11] it is determined that 8.8 W of heat are generated in the reaction channels, assuming 100% Cl_2 conversion. For reasons detailed in the next chapter, the microSOG is operated at less than half of this maximum flow rate, which reduces the thermal load in the experiments. The microSOG must also be able to remove any heat introduced from the ambient. The magnitude of the ambient heat source is a complex function of the external temperature, chip dimensions, and packaging. The need to determine this value motivates the thermal model discussed in this section. The model can also predict the silicon and BHP temperatures at a given operating point.

A 1-D layered model, conceptually illustrated in Figure 3-10, is proposed to simulate heat transfer in the microSOG. The model takes into account heat transfer

Table 3.3: Thermal properties of model layers.

Layer	Material	thickness	k $\frac{W}{cmK}$	h $\frac{W}{cm^2K}$
	air/tefzel	N/A	N/A	0.0025
1	tefzel	1.2 cm	0.0024	N/A
2	pyrex	0.2 cm	0.011	N/A
	pyrex/BHP	N/A	N/A	0.89
3	BHP/Cl_2	300 μm	5.8 x 10^{-3}	N/A
	BHP/silicon	N/A	N/A	0.89
4	silicon	325 μm	1.3	N/A
	silicon/coolant	N/A	N/A	3.42
5	coolant	300 μm	1.18 x 10^{-3}	N/A
	coolant/silicon	N/A	N/A	3.42
6	silicon	325 μm	1.3	N/A
7	tefzel	1.2 cm	0.0024	N/A
	tefzel/air	N/A	N/A	0.0025

Table 3.4: Thermal properties of Syltherm coolant at -10°C.

Property	Value
Density	0.87 g/cm^3
Specific Heat	1.572 J/(g · K)
Viscosity	2.5 mPa-s
Prandtl Number	33.4

through a slice of the structure, and employs a thermal circuit analogy to solve for temperatures and heat flows. In other words, the layers are assigned thermal resistances and the structure is solved as if it were a DC circuit. With this analogy temperature maps to voltage and heat flow (in Watts) maps to current.

The thermal model for the microSOG consists of seven layers. The thermal properties of each layer are summarized in Table 3.3. Only the area of microSOG directly above or below the reaction channels is considered in the calculations. This assumption may substantially understate the amount of ambient heat flowing in the microSOG; however, even if the ambient heat flow were several times larger it would still be insignificant compared to the heat of reaction occurring in the chip. The coolant in the cooling channel layer is dimethyl polysiloxane, a high performance coolant sold under the trade name Syltherm (Dow Chemical, Midland, MI). The

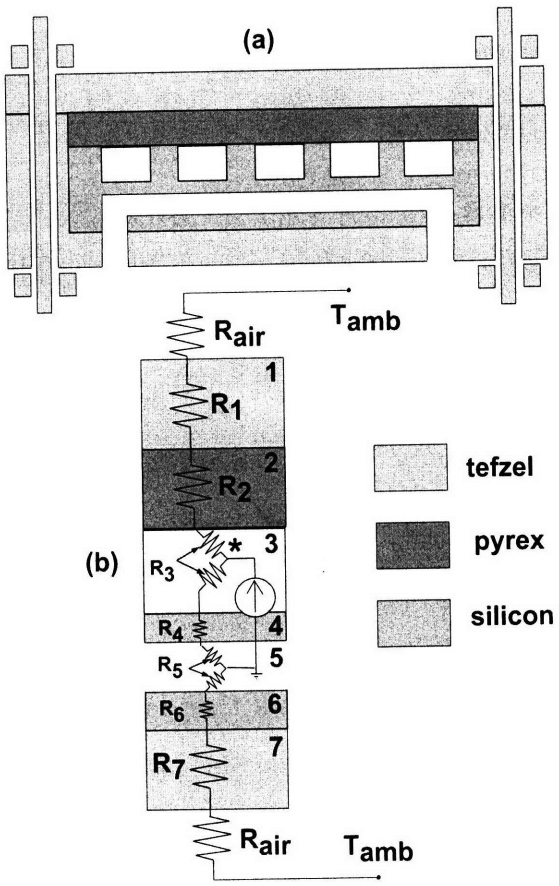

Figure 3-10: (a) Illustration of microSOG in tefzel package; (b) 1-D thermal model of microSOG with an equivalent thermal circuit.

thermal properties of Syltherm are provided for reference in Table 3.4. The transfer of heat between the ambient and the packaging layer, the reaction channels and the silicon, and the silicon and the coolant is dominated by convection. Convection is modeled as

$$q_{conv} = h \cdot A \cdot \Delta T, \tag{3.47}$$

where h is the heat transfer coefficient, A is the area of the microSOG slice that is perpendicular to the direction of 1-D heat flow, and ΔT is the temperature difference across the fluid layer. Estimations of the heat transfer coefficients for the reaction channels and cooling channels are respectively made from the Nusselt number correlations of Whitaker and Sieder-Tate [57], [51]. Heat flow through the solid layers is described by conduction, written as

$$q_{cond} = k \cdot A \cdot \frac{dT}{dx}, \tag{3.48}$$

where k is the thermal conductivity of the material. Finally, the cooling channel heat removal capacity is modeled by

$$q_{cool} = m^* \cdot C_p \cdot \Delta T, \tag{3.49}$$

where m^* is the mass flow rate of the coolant and C_p is the specific heat of the coolant. For the experiments presented in this thesis the coolant flow is constrained by the chiller, which can provide a maximum delivery pressure of 69 kPa to the chip.

For the purposes of the microSOG thermal model the silicon in the chip is assumed to be isothermal. This claim is supported by comparing the temperature drop across the silicon in its widest dimension to the temperature drop across the environment surrounding the microSOG. The widest silicon dimension is in the lateral direction; the pertinent layers and directions are illustrated in Figure 3-11. Utilizing Equations 3.48 and 3.47 the heat flow across the lateral layers of Figure 3-11 can be

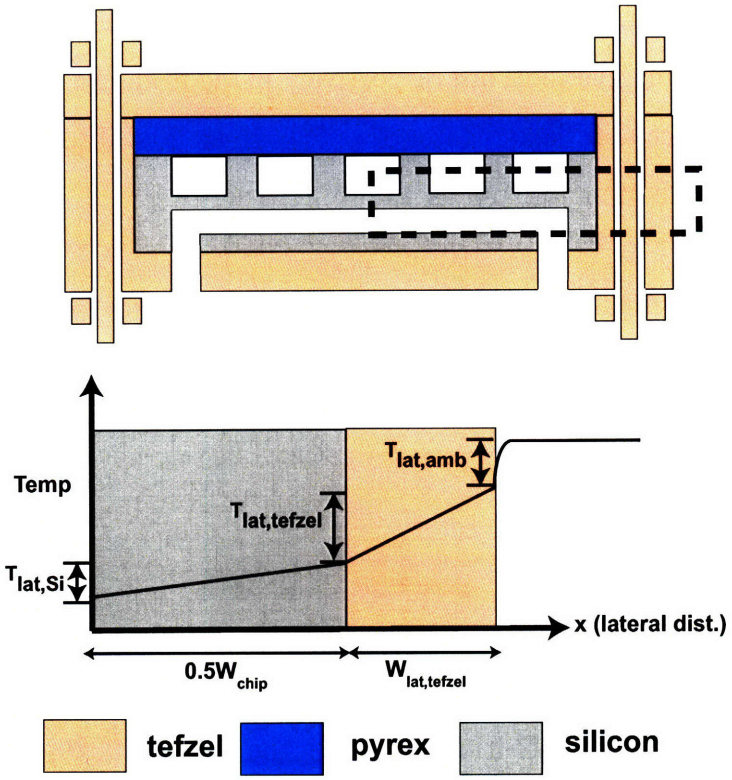

Figure 3-11: Illustration of lateral temperature variation across the microSOG, package, and ambient.

equated as

$$h_{amb} \cdot A \cdot T_{lat,amb} = k_{tefzel} \cdot A \cdot \frac{T_{lat,tefzel}}{W_{lat,tefzel}} = k_{Si} \cdot A \cdot \frac{T_{lat,Si}}{0.5W_{chip}}. \tag{3.50}$$

The cross-sectional area A is identical for all three layers, and therefore cancels out of the equation. Only half of the lateral chip width is considered because of the symmetry of the layers. By rearranging the terms of Equation 3.50 we obtain

$$\frac{T_{lat,Si}}{T_{lat,amb}} = \frac{h_{amb} \cdot 0.5W_{chip}}{k_{Si}} = Bi. \tag{3.51}$$

This non-dimensional formulation is referred to as the Biot number (Bi) of the system. Using the values in Table 3.3, Bi is determined to be 0.09. This means that the lateral temperature drop across the silicon is a factor of 10 smaller than the drop across the ambient thermal boundary layer. It is generally accepted that a layer can be treated as isothermal with minimal error in the subsequent thermal analysis if Bi $\leq$ 0.1 [38].

The relationships in Equations 3.47 and 3.48 can also be recast for the thermal circuit model with

$$R_{cond} = \frac{L}{kA} \tag{3.52}$$

and

$$R_{conv} = \frac{1}{hA} \tag{3.53}$$

representing resistances due to conduction and convection respectively. In this circuit voltage is calculated in degrees Kelvin and current has units of Watts. Consequently, the heat resulting from the reaction is modeled as a current source, while the ambient temperature is represented by the constant voltage T_{amb}. The circuit ground is the lowest temperature in the system, in this case the coolant temperature T_{gnd}. In order to solve the circuit, the temperature directly above the current source, corresponding in this case to the BHP temperature needs to be determined. An expression for T_* is obtained by applying Kirchoff's current law at this node,

$$\frac{T_{amb} - T_*}{R_{air} + R_1 + R_2 + R_3} + P_{rxn} = \frac{T_* - T_{gnd}}{R_3 + R_4 + R_5}, \tag{3.54}$$

where P_{rxn} represents the heat flowing in due to the reaction, and T_* represents the temperature at the node of interest. The expression

$$\frac{T_{amb} - T_{gnd}}{R_{air} + R_7 + R_6 + R_5} = P_{lower} \tag{3.55}$$

can be used to determine how much heat is flowing into the cooling channels from the lower layers of the microSOG. Finally the total power is found by combining Equations 3.54 and 3.55 into

$$P_{total} = \frac{T_{amb} - T_*}{R_{air} + R_1 + R_2 + R_3} + P_{rxn} + P_{lower}. \tag{3.56}$$

The thermal circuit is solved assuming an ambient temperature of 293K and a coolant temperature of 263K. For the maximum theoretical He:Cl_2 flow rate of 430 sccm that was proposed in [11], the BHP and silicon temperatures are respectively found to be 272K and 265K. Also, 8.9 W flows into the coolant from all sources; 99% of the heat comes from the reaction channels.

The final step in the thermal analysis is to verify that the cooling channels have enough flow capacity to remove the amount of heat calculated from the thermal circuit. This task is accomplished with Equation 3.49. With the cooling channel dimensions given in Chapter 2 and the specific heat of Table 3.4, the cooling channels should be able to remove 8.9 W from the device with a 1.5K temperature gradient across the channels. Since the chiller can provide coolant at temperatures as low as 223K, this requirement is well within the capabilities of the testing rig.

Chapter 4

Experimental Techniques and Measurements

This chapter details the testing apparatus and the testing methodology for the microSOG. First, the packaging solution and testing rig are described. Next, the spontaneous optical emission and mass spectroscopy diagnostics are discussed. Lastly, the experimental protocol is summarized.

4.1 Packaging

For the sake of simplicity, all of the inlet and outlet ports, shown in Figure 4-1, are placed underneath the lower layer of the microSOG. The design in Chapter 2 calls for reactant inlets that can operate at up to 227 kPa and coolant connections that can handle 165 kPa of delivery pressure. Conversely, the BHP and gas outlets of the microSOG operate in the respective sub-atmospheric pressure ranges of 4-24 kPa and 7-27 kPa. Therefore, any packaging solution for the microSOG must be able to handle a range of inlet/outlet conditions simultaneously. In addition, the package should both be chemically resistant to the reactants and cause minimal $O_2(a)$ deactivation. Finally the package should provide thermal insulation, reducing ambient heat flow into the microSOG. These challenges are overcome by the package design, which consists of Tefzel plates which are clamped around the chip. Tefzel

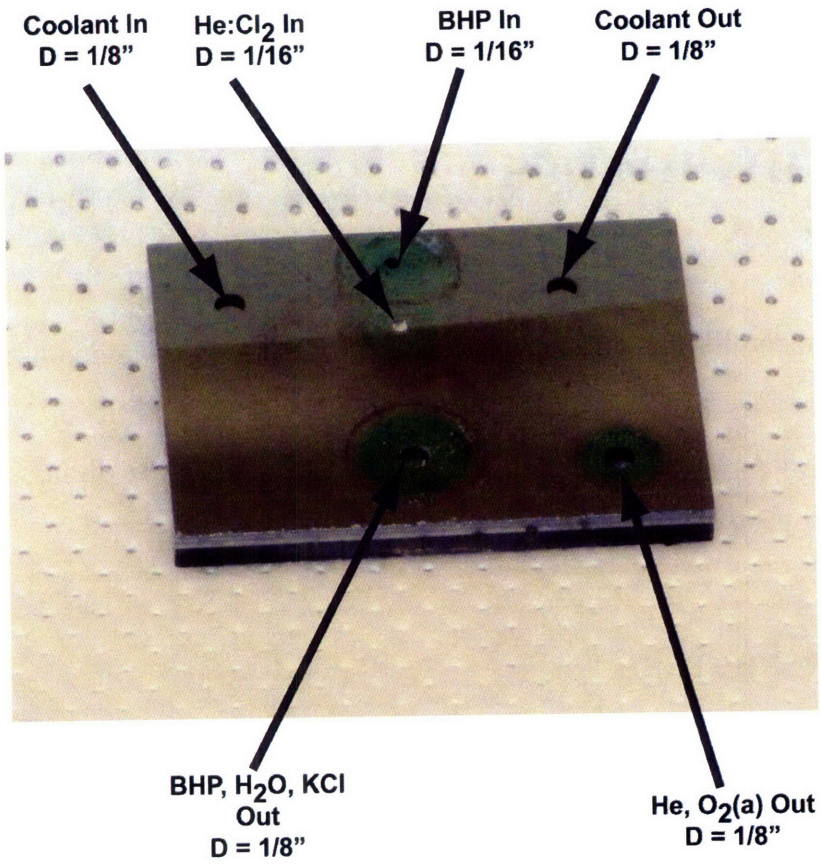

Figure 4-1: MicroSOG backside with various inlet and outlet ports.

is a form of teflon commonly used in molding and machining applications, and it is chosen for its chemical resistance to the reactants. The plates, shown in Figure 4-2, have recesses to allow O-ring sealing around the ports. The reactants are delivered to the package by teflon tubing, which connects to the plates through finger-tight Tefzel fittings (Bio-Chem Valve Inc., Boonton, NJ). Initial data were taken by using an epoxy to attach tubing to the silicon; as expected, these connections were not robust and very quickly failed. The $O_2(a)$ outlet of the microSOG is the only port that is not connected by teflon tubing. Instead, it connects to a quartz cuvette (Starna, Atascadero, CA) where the optical diagnostics are performed. Quartz is chosen for both its low $O_2(a)$ wall deactivation coefficient and its greater than 90% optical transmission rate at infrared wavelengths. The cuvette, shown in Figure 4-3, is initially cylindrical (0.2 cm OD) and later expands to a square cross section 1 cm in internal width, providing ample path length for a strong optical signal.

4.2 Testing Rig

The experiments were performed inside a ventilated cabinet because of the toxic and corrosive nature of chlorine gas and BHP. The rig schematic in Figure 4-4 highlights the reactant flow paths. Helium and chlorine are stored in compressed gas cylinders below the experiment; their flow to the chip is controlled by manual valves. The pipes and connections outside of the package are made from 316 stainless steel 1/4" piping, Swagelok fittings, and Cajon fittings, all of which will corrode after extended Cl_2 exposure. To combat this problem, a cross purge assembly is included to periodically flush any remaining Cl_2 from the flow path at the conclusion of an experiment. The Cl_2 and He flow through separate mass flow controllers before flowing concurrently into the microSOG gas inlet. A video camera/VCR setup monitors flow through the reaction channels. Upon exiting the microSOG the gaseous outflow enters the optical diagnostic region. It then flows through a liquid nitrogen trap designed to condense any unreacted Cl_2 and water from the gas stream. The stream is sampled by a mass spectrometer, which is connected to the setup via a glass capillary line.

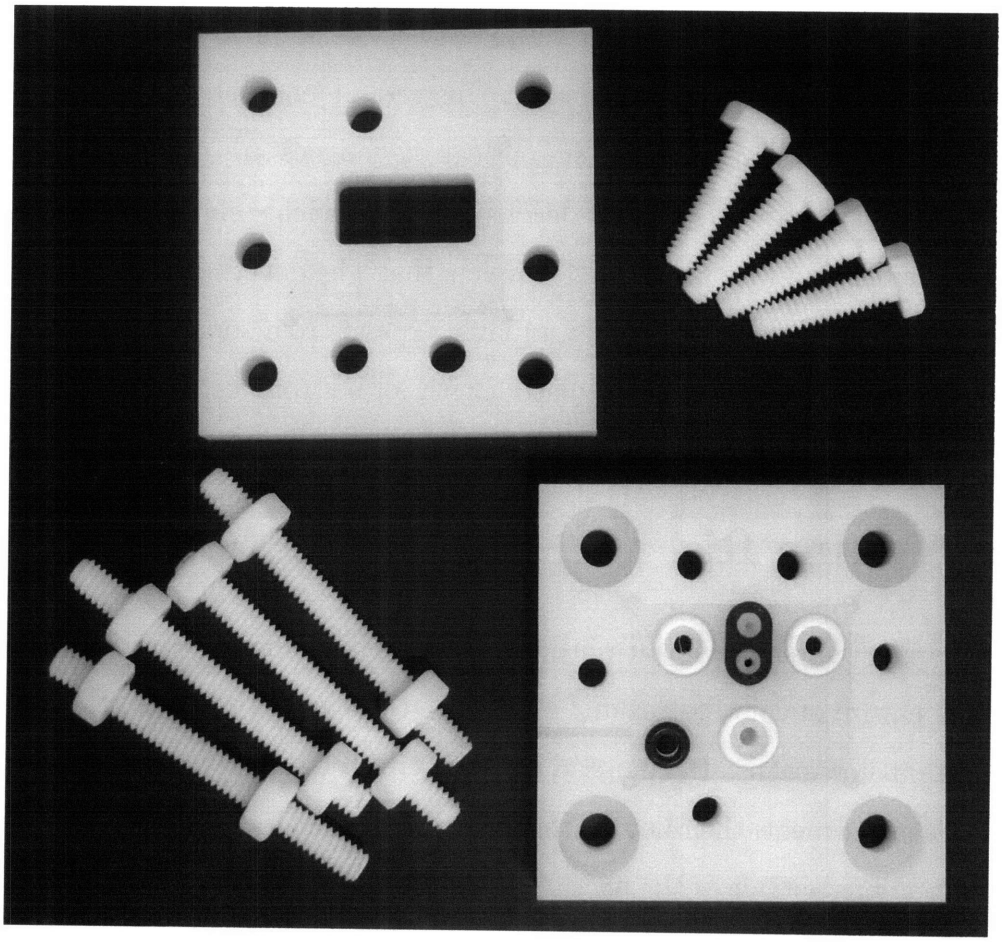

Figure 4-2: The microSOG package consists of two Tefzel plates, clamped together by Tefzel screws and bolts. The inlet and outlet ports are sealed by Kalrez and Simriz O-rings and gaskets.

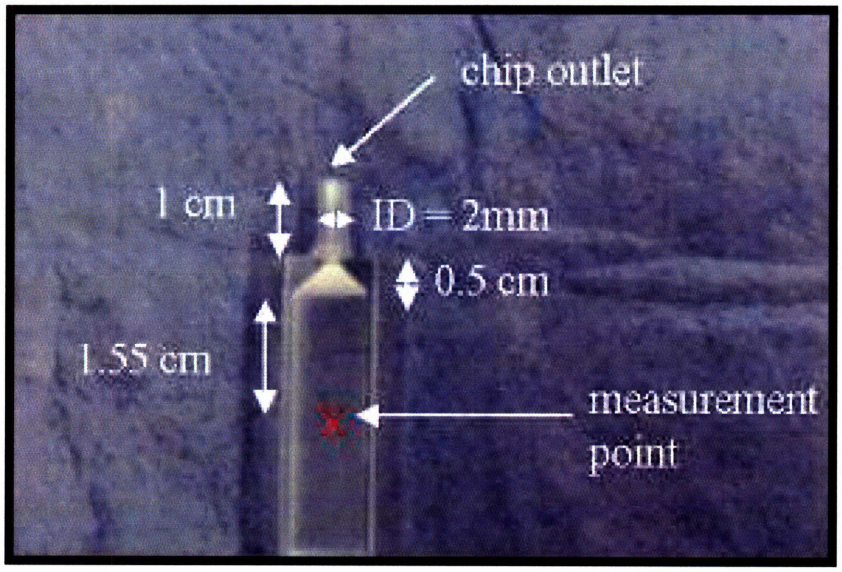

Figure 4-3: Upon exiting the microSOG, the gaseous products enter a quartz cuvette where the optical emission measurements are conducted.

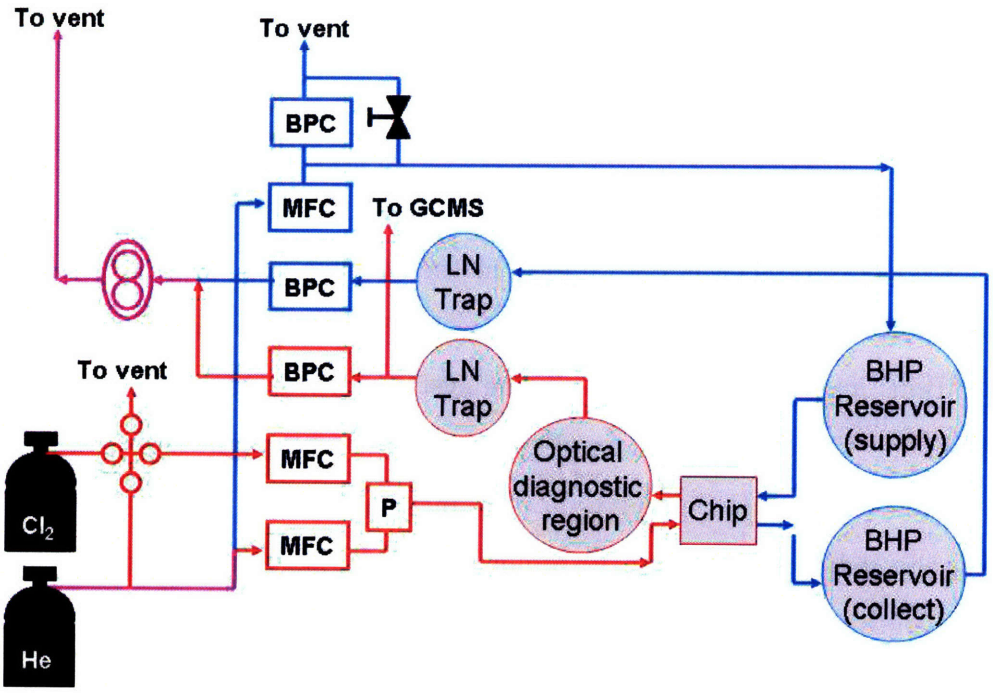

Figure 4-4: Schematic of the microSOG test rig. The liquid and gas flow paths are denoted by blue and red arrows respectively. The overlap between the paths is shown in magenta. MFC = Mass Flow controller; BPC = Back Pressure Controller; GCMS = Gas Chromatography-Mass Spectrometer.

Sub-atmospheric pressures in the flow path succeeding the microSOG are maintained by a vacuum pump. A photograph of the just-described testing rig is included in Figure 4-5. The BHP is stored in a glass-lined, stainless steel pressurized reservoir. Some of the He from the compressed tank is diverted into this reservior, which results in a pressurized feed of BHP into the microSOG. The helium pressure (and thus the BHP flow rate) is regulated by its own pressure controller (MKS Instruments, Wilmington, MA). The BHP reservoir and microSOG package are connected using teflon tubing and PEEK connectors (Upchurch Scientific, Oak Harbor, WA). The liquid by-products coming out of the chip are collected in a second reservoir. Both reservoirs are maintained at temperatures between -20°C and -10°C to minimize BHP decomposition. Temperatures throughout the testing rig are monitored using thermocouples. The entire setup is served by an external chiller (Julabo, Allentown, PA).

4.3 Optical Emission Setup

Although it is relatively straightforward to confirm $O_2(a)$ generation [19], quantitatively measuring the $O_2(a)$ concentration and yield are significant challenges. Typically SOG performance is determined in the context of a complete COIL system; heuristics are used to estimate yield from small signal gain and laser output along with various losses and efficiencies in the system [17]. In this work, a suite of more direct diagnostics were instead employed to obtain both qualitative and quantitative information on the $O_2(a)$ population. Production of $O_2(a)$ can be confirmed by observing the red glow of the $O_2(a)$ dimol emission. This emission produces photons of wavelengths 634 and 703 nm, depending on the vibrational state of the resulting $O_2(X)$ molecules, thus falling into the visible range [27]. However, since the Einstein coefficients relating to the dimol emission are not well characterized, drawing quantitative conclusions from it is difficult [5], [8]. In contrast, the decay of solitary $O_2(a)$ molecules into the triplet state, which produces photons in a molecular band centered at 1268 nm, can be used to determine $O_2(a)$ concentration because

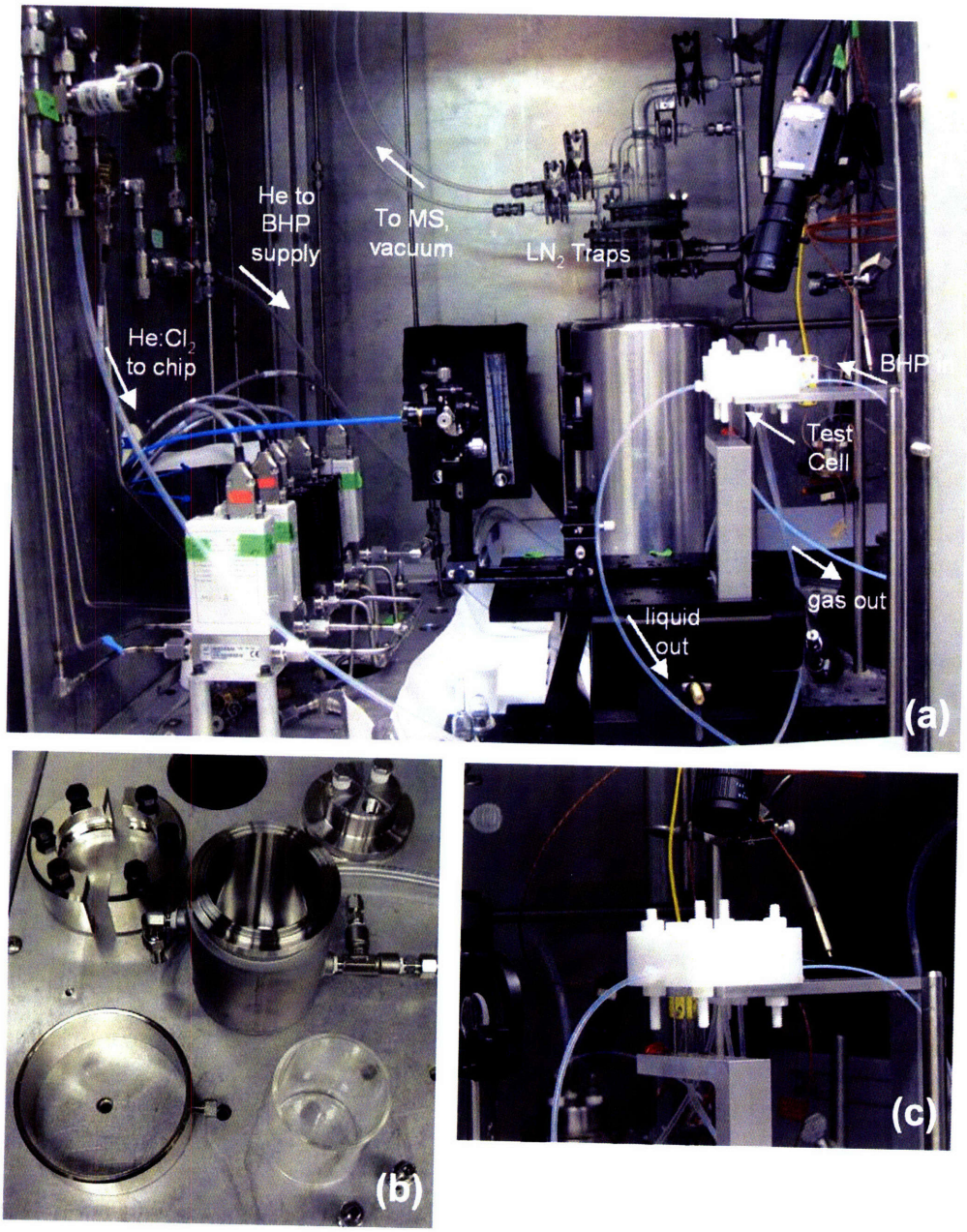

Figure 4-5: (a) Photograph of the microSOG testing rig highlighting gas and liquid flow paths; (b) Deconstructed view of the glass-lined pressurized vessel used to mix and store BHP; (c) Close-up view of the microSOG packaging with video camera, quartz cell, and thermocouples.

there is a one-to-one relationship between the photon emission rate and the number of $O_2(a)$ molecules in the field of view. Measurement of this electronic transition,

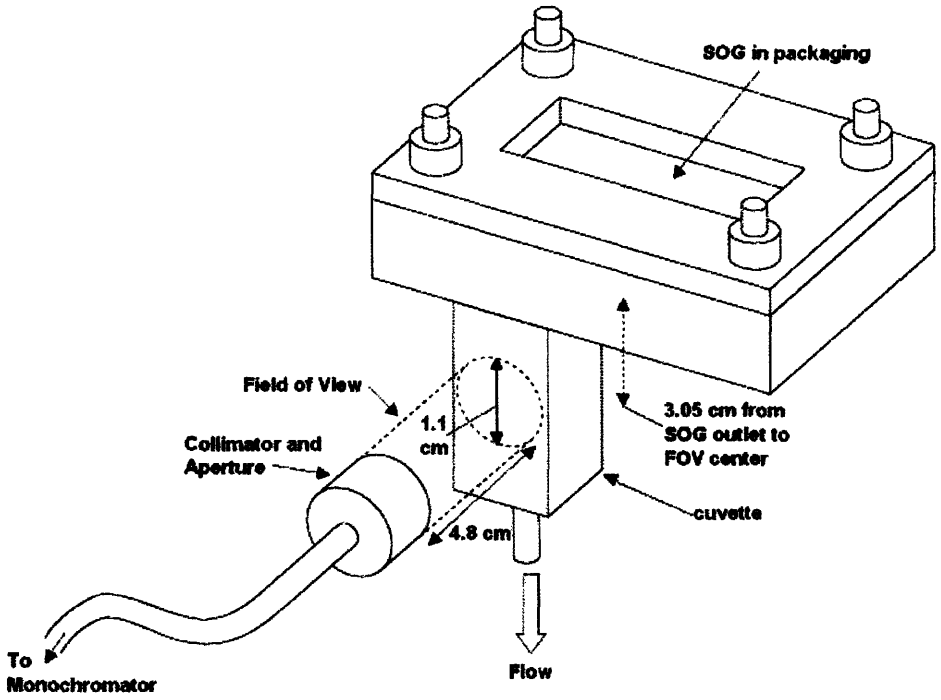

Figure 4-6: Schematic of the PSI optical diagnostic. Collimated optics sample a cylindrical volume in the quartz cuvette.

which has a better characterized spontaneous emission coefficient than that of the dimol emission [30], is accepted as the most precise $O_2(a)$ diagnostic by the COIL community. It can be measured via infrared spectrometer [48] or through the use of Ge detectors and optical filters [29]. In the current work two spectrometers are used. The first was owned and operated by Physical Sciences Inc. of Andover, MA, and its corresponding measurement setup is schematically shown in Figure 4-6. In this setup collimated optics, which are placed 4.8 cm from the center of the cuvette, capture the emission for a cylindrical cross section of the cuvette, yielding a 1.1 cm field of view. A liquid-nitrogen cooled InGaAs array spectrometer (Roper Scientific, Trenton, NJ) analyzes the photons collected by the collimator. For the integration of time of 5 seconds used with the spectrometer, the lower $[O_2(a)]$ detection limit is $1x10^{15}cm^{-3}$. The intensity of the spectrometer signal is calibrated to the spectral radiance of a blackbody source at 1000 K. The second diagnostic was built at MIT. In the MIT di-

agnostic, a lens (f/# 1.9) is placed 13.1 cm from the cuvette and 8.1 cm from the fiber input of the spectrometer. The lens samples a cone of the cuvette volume, and the collected photons are analyzed by an Ocean Optics (Dunedin, FL) NIR512 InGaAs array spectrometer. The MIT setup, shown in Figure 4-7, was initially calibrated using an infrared LED, but was later calibrated to the PSI diagnostic during simultaneous measurements. During the measurements the microSOG package is clamped to an aluminum bracket, which is in turn attached to a 2D stage. The quartz cuvette is held by a second bracket, ensuring consistent and repeatable alignment of the MIT setup. Finally, an uncalibrated spectrometer is used to observed the dimol emission described earlier.

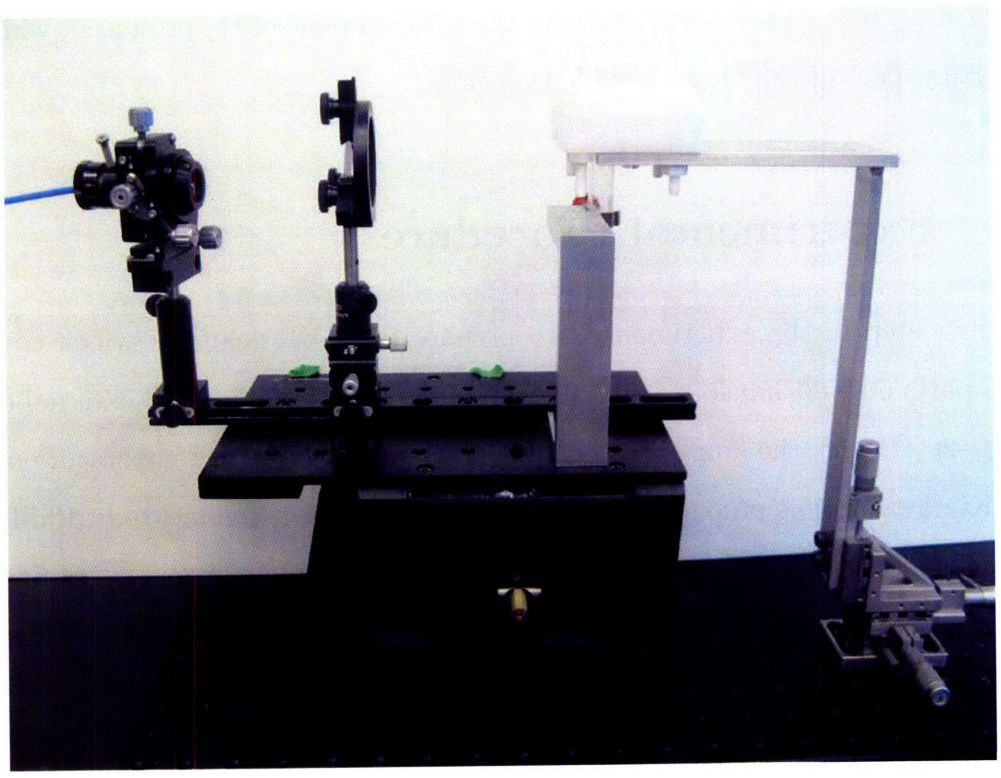

Figure 4-7: Photograph illustrating the MIT optical emission diagnostic.

4.4 Mass Spectroscopy

In addition to the optical emission setup discussed in the previous section, a mass spectrometer (MS) monitors the microSOG output stream. When gas enters the MS

from the glass capillary line, it is immediately ionized by an ion source. The ion source consists of a filament that generates an "emission current" of electrons when heated. Next a quadrupole filters the ions. This task is accomplished by biasing the quadrupole electrodes, which in turn control the trajectory of an ion according to its mass-to-charge ratio. Varying the electrode potential allows the MS to sweep the sample gas for an array of molecular species. The influx of filtered ions is then collected by an ion detector. The resulting ion current can be used to calculate the partial pressure or mole fraction of a given constituent gas species. The MS used in the microSOG experiments was calibrated using a compressed tank with known proportions of O_2 and He. Although the MS cannot distinguish between the various states of O_2 it is useful in determining the total amount of O_2 produced, which is an important part of the O_2(a) yield calculation.

4.5 Experimental Procedure

The first step in the experiment is to prepare the BHP solution, which consists of equal parts 50 wt% aqueous KOH solution and 50 wt% H_2O_2. The external chiller is set at -20°C, with the aim of the coolant reaching the rig at a temperature of -15°C. The KOH solution is prepared by dissolving KOH pellets (Mallinckrodt, Phillipsburg, NJ) in de-ionized water. The KOH solution is then added to 50 ml of H_2O_2 in 5 ml increments to ensure that the solution temperature never exceeds 25°C. At this point most of the coolant is diverted away from the chip in an effort to slow H_2O_2 decomposition in the BHP vessel. The jacketed vessel that collects the BHP outflow from the microSOG is cooled as well.

First, helium flow is introduced into the chip at atmospheric pressure, followed by BHP flow. Gas and liquid flow is immediately visible in the reaction channels, and the capillary separator functions correctly at the outset. Pressure controllers monitor conditions both above and below the separator pores; their set points are gradually lowered until the desired operating point is reached (generally 7-27 kPa at the microSOG gas outlet with a 3 kPa drop across the pores). As the pressure is being

lowered, coolant flow is introduced into the microSOG and increased until it reaches its set point at around -5°C. Once the desired pressures are reached, chlorine, flowing concurrently with helium with a 3:1 He:Cl_2 ratio, is injected into the chip in pulses that are 1-2 minutes in duration. The emission resulting from spontaneous $O_2(a)$ decay is captured and analyzed by the diagnostics described in the previous sections. After a number of runs, the remaining BHP is collected, diluted, neutralized, and disposed of as hazardous waste. The microSOG is brought back to room temperature while flowing water through the reaction channels to remove any KCl that may have precipitated onto the microSOG features. After a few minutes of water flow, the chip is dismounted from the package, dried out for 30 minutes using an oven, and stored for future use. Very little of the capillary separator area appears to be in use during the experiments, which is expected from the considerable over-sizing of the separator described in Chapter 2. Also, crystals of KCl are observed to form in the device channels after a number of runs (and in particular after runs with very high ratios of chlorine gas to BHP) and eventually lead to clogging in the device channels. The clogging in turn lessens the intensity of the spectral peaks with successive chlorine pulses. The observed clogging has important implications for the data analysis presented in Chapter 5. The detailed experimental instructions for the microSOG are included for reference in the appendices.

Chapter 5

Experimental Results and Analysis

This chapter reports on the measured performance of the first-generation microSOG device. First, the range of operating points explored is defined. Next, the data from the mass spectroscopy measurements are presented. Finally, the optical emission results are discussed, along with a modification to the model presented in Chapter 3.

5.1 Preliminary Characterization

Before the experiments were conducted, preliminary runs with He and water were performed to test the capabilities of the testing rig and to refine the experimental protocol. Additionally, the capacity of the cooling channels was explored.

5.1.1 Helium and Water Flows

The experiments with preliminary flows serve two purposes: to determine the parameter space to be used in the experiments, and to observe and catalog the reaction channel behavior given in Figure 3-7. Helium and water are chosen for their inertness and viscosities, which are similar to the actual reactants. For an operating point to be used in the actual experiment, the separator had to perform adequately and the package had to adequately seal the microSOG inlets and outlets. The performance of the gas-liquid separator was separately tested and is summarized in Figure 5-1. The

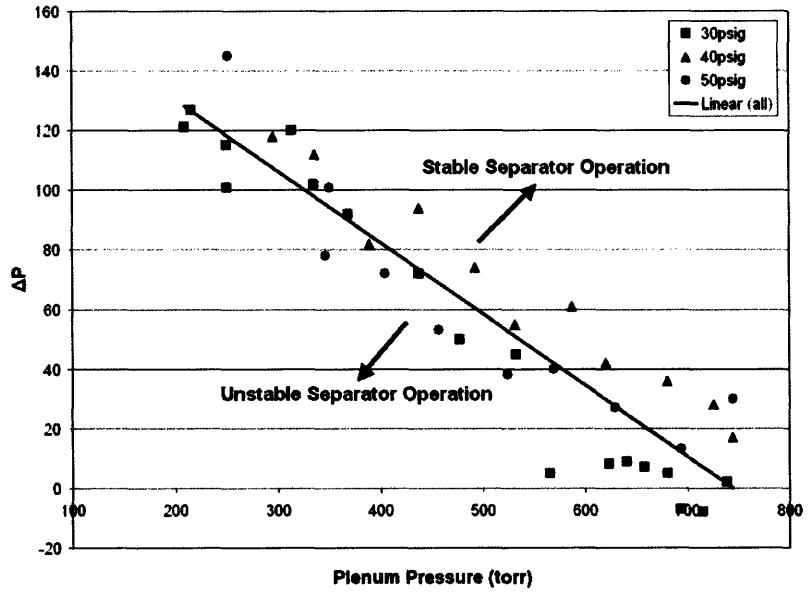

Figure 5-1: Plot of gas-liquid separator performance for various liquid delivery pressures and 150 sccm of He flow. The points refer to pressure drops below which the separator is unable to prevent liquid from spilling into the gas outlet. ΔP refers to the pressure drop across the pores.

gas outlet (plenum) pressure was varied between atmospheric pressure and 100 torr for several liquid delivery pressures. The He flow rate was held constant at 150 sccm. The points refer to pressure drops below which the separator is unable to prevent liquid from spilling into the gas outlet. At lower gas outlet pressures, a larger drop across the pores is needed for the separator to behave correctly.

5.1.2 Cooling Channel Characterization

The heat removal capacity of the cooling channels was empirically verified before attempting to produce $O_2(a)$. Using thermocouples to monitor the coolant and silicon temperatures, the specific heat equation was used to calculate the total heat removed. The heat source in this experiment is the ambient environment. Figure 5-2 illustrates the measured heat removal capacity of the channels as a function of the silicon temperature. The heat removal capacity was calculated using Equation 3.49. The curve in Figure 5-2 confirms that the cooling channels are capable of removing up to 10 W of heat while keeping the silicon temperature several degrees below 0°C. This curve

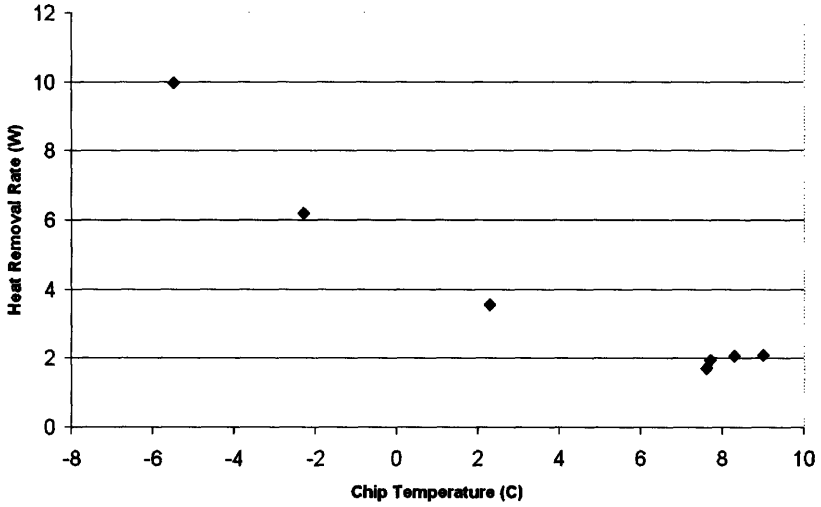

Figure 5-2: Measured heat removal capacity of the cooling channels versus internal chip temperature. For this plot, the heat source was provided by the ambient environment surrounding the device.

was generated in the microSOG without the insulating Tefzel package surrounding it; had the package been included the curve would likely be shifted downward. In other words, a lower rate of heat removal would have been required to keep the microSOG at a given temperature.

5.2 Operating Points and Parameter Space

In [11] the theoretical performance of a microSOG is simulated with gas feed rates ranging from 4-430 sccm, BHP feed rates ranging from 0.1-7 ml/min, and gas outlet pressures ranging from 7-40 kPa. The liquid feed rate is set to ensure that there is a 10:1 O_2H^-:Cl_2 ratio in the reaction channels. For the current work a smaller parameter space is used, which is shown in Table 5.1 and largely based on the achievable He/H_2O flows mentioned in the previous section. The run numbers correspond to measurements done with both the PSI and MIT diagnostics simultaneously. Some experiments were also performed using solely the MIT setup; for these the operating point in run 3 was used. Temperatures ranged from 269K-279K in the microSOG and from 266K-269K in the BHP reservoirs. The experiments described here were conducted over a three-day period, with five runs occurring per day.

Table 5.1: Operating points for the microSOG experiments

Run #	He flow sccm	Cl_2 flow sccm	BHP flow (cm^3/min)	P_{outlet} kPa	T_{chip} C	T_{supply} C	$T_{collector}$ C
1	37	13	0.95	13	4	-6	-5
2	56.75	18.75	1.32	13	N/A	N/A	N/A
3	75	25	1.31	13	N/A	N/A	N/A
4	37	13	0.95	13	N/A	N/A	N/A
5	56.75	18.75	1.32	13	N/A	N/A	N/A
6	75	25	1.3	27	6.1	-4.2	-5.5
7	75	25	1.3	20	5.3	-4.9	- 5.7
8	93.75	31.25	1.3	13	4.7	-5.6	-5.5
9	112.5	37.5	1.29	13	4.3	-6.2	-4.5
10	131.25	43.75	1.29	13	4.2	-6.4	-4.8
11	125	25	1.29	13	4.3	-5.5	-5.3
12	175	25	1.28	13	4.0	-5.9	-5.2
13	75	25	1.32	7	4.0	-6.2	-5.1
14	75	25	1.32	7	-0.9	-6.5	N/A
15	37	13	1.34	7	-4.0	-7.6	N/A

5.3 Mass Spectroscopy Results

The emission current data from the mass spectrometer were used to calculate the O_2 partial pressure rise from the O_2(a) reaction. The O_2 partial pressure rises in response to the chlorine pulses pumped into the chip. This behavior is clearly shown in Figure 5-3, in which the observed rise corresponds to the conditions of run 3. For several runs the data were used to calculate the rate of Cl_2 conversion into O_2,

$$Cl_{util,ms} = \frac{\Delta P_{O_2}}{P_{Cl_2'}}, \tag{5.1}$$

where ΔP_{O_2} is the rise of the O_2 partial pressure at the microSOG outlet in torr, and $P_{Cl_2'}$ is the hypothetical partial pressure of Cl_2 at the outlet if no Cl_2 had reacted. Chlorine conversion data are provided for selected runs in Table 5.2. The calculated values range from approximately 20-50%, with a maximum occurring in run 9. Several runs are omitted from the table due to the lack of a stable O_2 baseline in the data. The error in the columns of Table 5.2 originates from propagation of the 4% uncertainty in the O_2 mole fraction of the calibration tank.

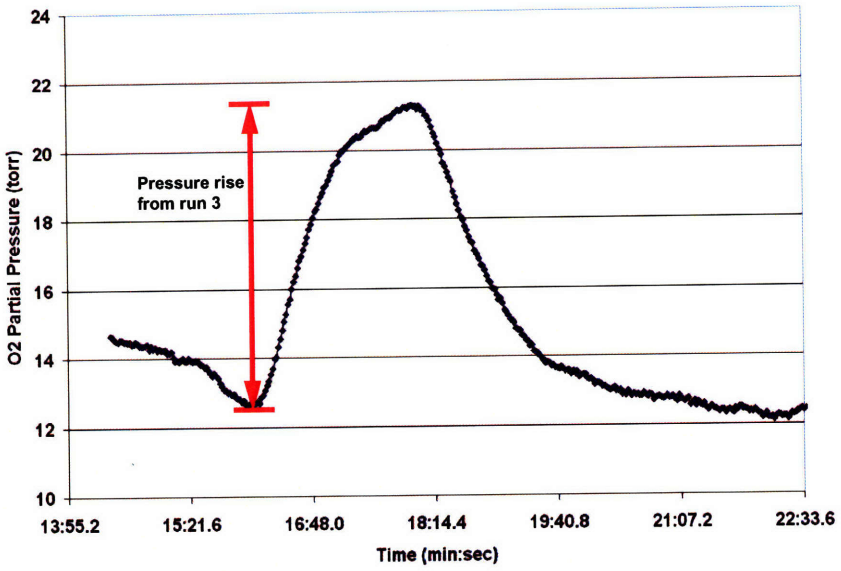

Figure 5-3: Mass spectrometer data illustrating rise in O_2 partial pressure corresponding to Cl_2 pulses into the chip.

Due to limitations in the testing rig, the data presented in Table 5.2 understate the true amount of oxygen produced. Specifically the data above, assuming that all of the observed O_2 was at some point $O_2(a)$, suggest concentrations significantly below the values obtained from the emission results presented elsewhere in this chapter. The causes for this discrepancy relate to the testing rig design and experimental protocol. First, the flow path between the microSOG outlet and the MS input is many times longer than the flow path through the chip, and the operating pressure and He flow rate were modified between runs in the interest of exploring the parameter space. These two factors most likely distorted the pulse shape as well as contributed to the difficulty in maintaining a constant O_2 baseline. Second, the liquid nitrogen traps condense oxygen along with Cl_2 out of the gas stream, as evidenced by the blue liquid found in them after some of the experimental runs. Any liquid O_2 in the traps would have reduced the partial pressure rises observed in the data. Therefore, the MS data can only be taken as a lower bound of the Cl_2 conversion rate, and cannot be used to directly calculate the $O_2(a)$ yield.

Table 5.2: Mass spectrometer data for the microSOG experiments

Run	Δ P_{O_2} (torr)	Cl_2 conversion (%)
3	8 +0.68/-0.16	32 +3/-1
4	9.5 +0.69/-0.19	37 +3/-1
5	4.6 +0.75/-0.09	18 +3/-0.3
6	8.4 +1.16/-0.16	17 +2/-0.3
7	8.4 +0.82/-0.18	22 +2/-0.5
8	6.8 +0.57/-0.17	23 +2/-1
9	12 +0.62/-0.22	48 +2.5/-1
13	4.7 +0.3/-0.09	38 +2.5/-1
14	5.7 +0./-0.12	46 +2.4/-1
15	4 +0.32/-0.08	32 +2.5/-1

5.4 Spontaneous Emission Results

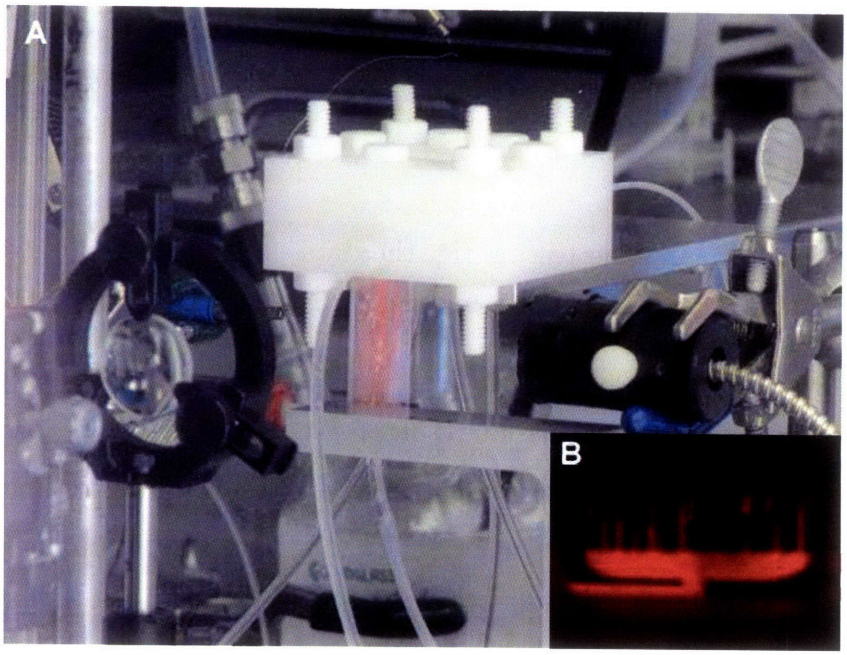

Figure 5-4: The glow resulting from the dimol emission is visible in (A) the quartz cuvette and in (B) the reaction channels.

The emission measurement data confirm the successful production of O_2(a) by the microSOG. After initiating the Cl_2 flow the signature red glow of the dimol emission is immediately visible both inside and outside of the chip, as illustrated by Figure 5-4. The glow sometimes continued well after the end of the pulse; this can be attributed to lingering Cl_2 in the flow path. The production of O_2(a) is also suggested by the

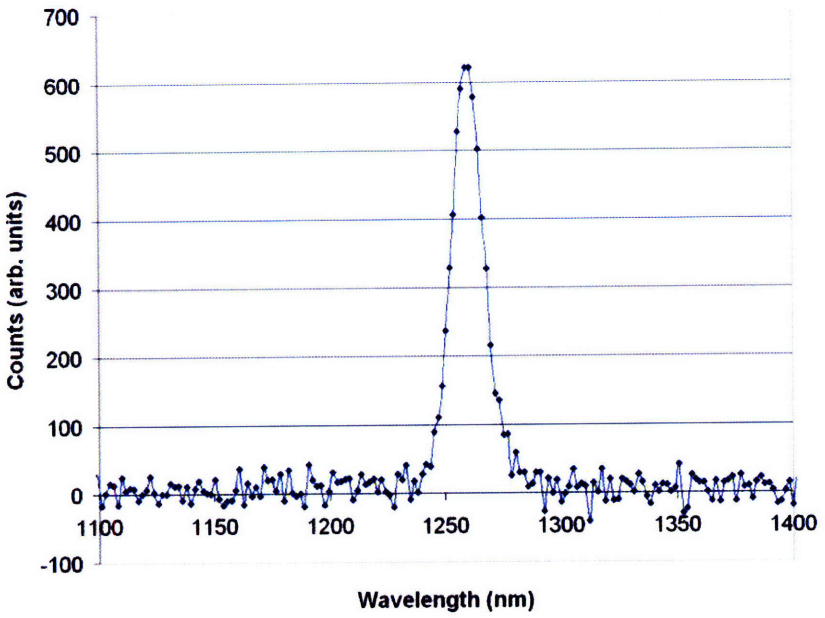

Figure 5-5: Spectrum captured by the MIT diagnostic, with a peak denoting the $O_2(a) \rightarrow O_2(X)$ transition.

spectra obtained with the optical diagnostic tools. A strong peak corresponding to the $O_2(a)$ spontaneous emission is seen in Figure 5-5. This peak, which was obtained using a 3-second integration time, is slightly shifted from the expected center of 1268 nm. This effect is attributed to nonidealities in the grating and CCD array rather than a uniquely different emission, since it is also seen during simultaneous measurements with the PSI diagnostic. The spectra from the PSI diagnostic in Figure 5-6 show that the microSOG quickly reaches steady-state operation after the Cl_2 flow begins. The increase in intensity after scan 20 is due to a reduction in the He flow rate, which in turn increases the Cl_2 residence time in the inlet lines. Finally, a third spectrometer was used to qualitatively observe the dimol emission. The two peaks in Figure 5-7 respectively correspond to the (0-0) and (0-1) simultaneous vibrational transitions of $O_2(a)$ molecules into their lowest electronic state ($O_2(X)$).

5.4.1 Determination of $O_2(a)$ Concentration

The spectra reported in the previous section are used to determine $O_2(a)$ concentrations. This is accomplished for both emission setups by first scaling the spectrometer

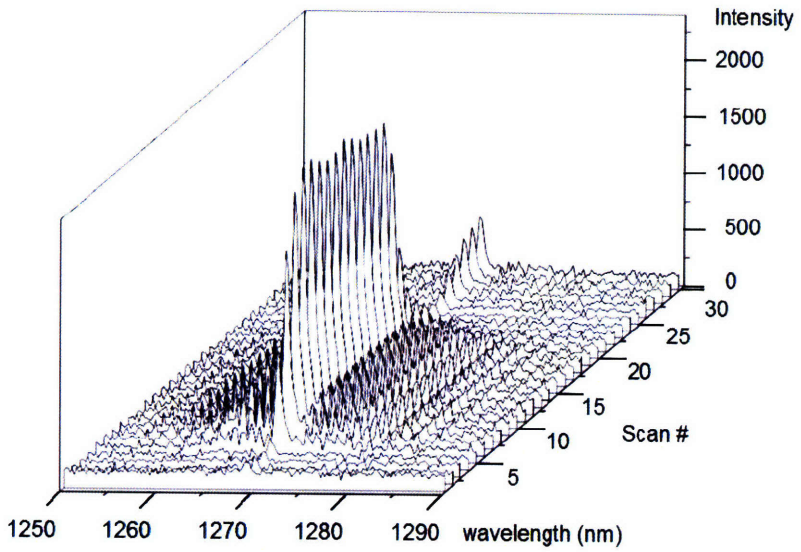

Figure 5-6: MicroSOG emission spectrum for run 6 as captured by the PSI spectrometer. The scans were taken in 5 second increments, and the intensity has arbitrary units.

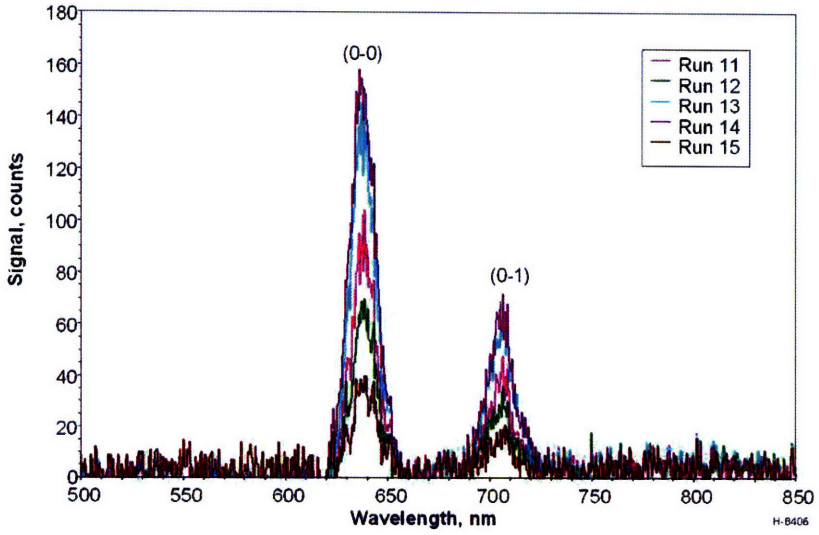

Figure 5-7: Spectra indicating the dimol emission from the microSOG.

counts by a calibration factor, then applying field of view and time correction factors, and finally integrating across the wavelengths of interest. This process, also reported in [48] and [35], is summarized by the integral

$$[O_2(a)] = \int \frac{C_{O_2(a)} \cdot I(\lambda, T) \cdot 4\pi \cdot A_{FOV} \cdot \tau_{exp}}{C_{BB} \cdot A_{12} \cdot L \cdot \tau_{calib}} d\lambda, \tag{5.2}$$

where $C_{O_2(a)}$ and C_{BB} respectively represent spectrometer and blackbody counts at a given wavelength λ, $I(\lambda, T)$ is the Planck blackbody function, A_{FOV} is a correction factor for the field of view, τ_{exp} and τ_{calib} are the integration times for the experiment and calibration respectively, A_{12} is the O_2(a) Einstein coefficent for spontaneous emission, and L is the path length.

In the PSI setup the collimator samples a cylindrical field of view of diameter 1.1 cm, which is 0.1 cm larger than the cuvette width. This mismatch results in a 5.5% reduction in the actual field of view, or an A_{FOV} value of 0.945. Also, the spectrometer used an integration time τ_{exp} of 5 seconds for runs 1-15 and an integration time τ_{calib} of 0.01 seconds for the blackbody calibration. A_{12} has recently been reported in the literature as 2.2 x $10^{-4}s^{-1}$ [30]. In this case, the path length L refers to the depth of the cuvette perpendicular to the direction of gas flow, which is 1 cm. It is important to note that the integral of Equation 5.2 is calculated numerically with the trapezoidal rule, since the spectrometer samples at discrete wavelengths rather than continuously. The error in the concentration measurement originates primarily from uncertainty in A_{12} ($\pm$10%) and A_{FOV} ($\pm$2.6%), with a total sum of squared errors of $\pm$13%. The resulting concentrations for each of the 15 runs are listed in Table 5.3. The measured values range from 5x10^{16} to 10^{17} cm^{-3}.

Concentration values are obtained for the MIT diagnostic data using Equation 5.2, with the addition of a function $\beta(\lambda)$ relating counts between the two spectrometers. $\beta(\lambda)$ is obtained by comparing data taken simultaneously by the two spectrometers, and introduces a $\pm$25% error into the measurement. As a result, the concentrations measured with the MIT diagnostic have a total sum of squared errors of $\pm$27%. The results from the MIT diagnostic for runs 1-15 are also listed in Table 5.3. The MIT

Table 5.3: Measured Concentrations from the PSI and MIT diagnostics, along with chemical efficiencies at the measurement point for runs 1-15.

Run	$[O_2(a)]_{PSI}$ cm^{-3}	$[O_2(a)]_{MIT}$ cm^{-3}	E_{chem} %
1	7.2 x 10^{16}	1.7 x 10^{16}	9.5
2	1.04 x 10^{17}	2.4 x 10^{16}	14.4
3	9.5 x 10^{16}	1.5 x 10^{16}	13.2
4	7.6 x 10^{16}	1.6 x 10^{16}	10
5	7.2 x 10^{16}	1.8 x 10^{16}	9.6
6	8.5 x 10^{16}	1 x 10^{17}	5.7
7	10^{17}	1.5 x 10^{17}	9.1
8	9.2 x 10^{16}	9.1 x 10^{16}	12.6
9	7.7 x 10^{16}	1.1 x 10^{17}	9.9
10	7.7 x 10^{16}	1.3 x 10^{17}	9.7
11	8.6 x 10^{16}	1.2 x 10^{17}	15.9
12	7 x 10^{16}	1.2 x 10^{17}	16.7
13	9 x 10^{16}	2.2 x 10^{17}	22.5
14	9.5 x 10^{16}	1.4 x 10^{17}	23.2
15	5 x 10^{16}	8 x 10^{16}	11.6

data indicate significantly lower $O_2(a)$ concentrations than their PSI counterparts for runs 1-5. The low concentrations on this first day of testing can be attributed to a disturbance in the optical path of the MIT setup, which is extremely sensitive to small changes in the optical working distances. The data from both setups for runs 6-15 are in general agreement.

The PSI data are used to calculate an overall chemical efficiency at the measurement point for the microSOG, defined as

$$E_{chem} = \frac{[O_2(a)]_x}{[Cl_2]'}, \tag{5.3}$$

where $[O_2(a)]_x$ is the concentration of oxygen in the $O_2(a)$ state at a point of interest x, and $[Cl_2]'$ is the theoretical concentration of Cl_2 that would exist at point x if no reaction had taken place. In other words, E_{chem} is a ratio of $O_2(a)$ molecules at point x versus Cl_2 molecules at the input of the microSOG. The values for E_{chem} at the measurement point range from 9%-23% for runs 1-15.

5.4.2 Fine Structure of Oxygen

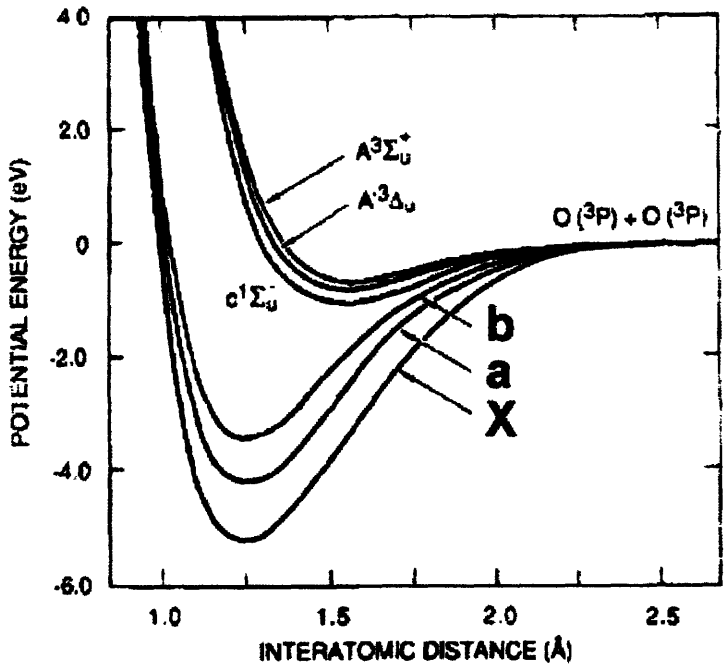

Figure 5-8: Potential energy curves for the bound states of O_2 [52].

The spectra of Figures 5-5 and 5-6 contain information beyond simply O_2(a) concentration. By analyzing the microSOG spectra, data about the electronic, vibrational, and rotational components of O_2(a) molecules can be obtained. The electronic energy of a diatomic molecule's molecular state depends on the atomic spacing and is obtained by using a Hamiltonian to operate on its specific molecular wavefunction. Figure 5-8 illustrates the relationship between potential energy and atomic spacing for the lowest states of O_2. The negative values of energy for the states indicate an attractive force between the atoms. The electronic energy difference between the O_2(a) and O_2(X) states at the lowest-energy inter-atomic distance corresponds to a wavelength of 1268 nm [34]. The electronic component of the energy has by far the largest magnitude. Rotational and vibrational transitions may occur within a given electronic state, but the optical diagnostics are only designed to observe them occurring in tandem with changes in electronic energy.

In order to model the vibrational states of O_2(a), the molecule is imagined as two

point masses connected by a massless spring. Such a system is well modeled by a harmonic oscillator in which the energy of a specific state is given by

$$E_{vib} = h\nu_{osc}(\nu + 1/2) + \omega_e x_e + ..., \tag{5.4}$$

where ν and ν_{osc} respectively represent the vibrational quantum number and the fundamental frequency of oscillation. The parameters ω_e and x_e represent anharmonicity coefficients, needed because the potential energy curves in Figure 5-8 are not perfectly parabolic. The spectra in Figures 5-5 and 5-6 feature the 0-0 transition band; in other words no change in the vibrational state between the O_2(a) and O_2(X) states of O_2 is observed.

The rotational behavior of the O_2 can be modeled using a rigid rotator model, in which the molecule is approximated as two masses joined by a rigid beam and allowed to rotate about its x, y, and z axes. The solution to this model, detailed in [34], relates the rotor energy

$$E_{rot} = \frac{h^2 \cdot J(J+1)}{8\pi^2 I} \tag{5.5}$$

to J, the resultant momentum vector for a given molecular electronic state. The parameter h refers to Planck's constant and I is the moment of inertia for the molecule. Equation 5.5 is often simplified through the introduction of the rotational constant

$$B = \frac{h}{8\pi^2 cI}, \tag{5.6}$$

where c is the speed of light in vacuum. Selection rules require J to be an integer, and furthermore limit ΔJ to values of 0, 1, or 2 during rotational transitions. The family of transitions in which ΔJ equals -2, -1, 0, +1, or +2 are respectively referred to as the S, R, Q, P, and O branches of the spectrum. In Figure 5-6 the Q branch is the strongest, with weaker P and R branches visible to the left and right respectively. The location and relative intensity of the individual rotational transitions that make

Table 5.4: Rotational temperatures assuming T=296K.

Run	θ_{rot}, K
1	330
2	335
3	335
4	330
5	320
6	325
7	335
8	333
9	310
10	305
11	300
12	285
13	300
14	298
15	295

up the branches are governed by a partition function, defined in [44] as

$$q_{rot} = \sum_{J=0}^{\infty}(2J+1)exp(\frac{\theta_{rot}J(J+1)}{T}), \tag{5.7}$$

where T is the temperature in Kelvin and the rotational temperature is defined as

$$\theta_{rot} = \frac{hB}{k_B}, \tag{5.8}$$

where k_B is the Boltzmann constant. It is important to note that θ_{rot} is not a temperature but rather a distribution parameter. By assuming an actual temperature of 296K in the gas, the location and relative magnitude of the spectral branches are fit to rotational temperatures, listed in Table 5.4.

5.5 Kinetics Analysis

Ideally, the O_2(a) concentration would be measured at the gas outlet, since that is the point at which the next stage of the laser system would be connected. Measure-

ments are made further down the cuvette in this case in order to ensure that the field of view of the collimated optics is not obscured by the package or other parts of the test apparatus. Fortunately, Equation 3.27 can be used to extrapolate the $O_2(a)$ concentration and E_{chem} anywhere along the flow path given a concentration value downstream from that point, albeit with increasingly large error bars. In this analysis, Equation 3.27 is used to extrapolate the measured concentration and E_{chem} product up to the chip's gas outlet. As was mentioned above, the values at the chip's outlet are expected to be a better predictor of the performance of the microSOG chip in a complete MEMS COIL system than the value at the current measurement point is. The scale mismatch between the microSOG and the external diagnostic region in this case leads to low flow velocities in the cuvette and much greater $O_2(a)$ losses than would occur in a MEMS COIL system in which the other components were integrated at the MEMS scale. When the measured values are extrapolated to the chip's outlet using Equation 3.27, the resulting values are substantially higher, with chemical efficiencies approaching 80% and with the concentrations in most runs in excess of 10^{17} cm^{-3}. When the concentrations extrapolated from the raw data are compared with those predicted by the baseline kinetics model described earlier, it becomes evident that some modification to the baseline model will be necessary in order to adequately explain the results. In most of the experimental runs, the extrapolation of the measured data produced higher but plausible values of the concentration and chemical efficiency values; however, in runs 1, 2, 6, and 7 the extrapolation produced values of concentration and chemical efficiency that are physically impossible. In those four cases, the extrapolation indicates that there is more than one $O_2(a)$ appearing at the chip's gas outlet for each Cl_2 entering at the input, which is not possible. In some of these cases, even extrapolating the lower error bar for the measurement point produces unphysically high values for $O_2(a)$ concentration at the chip's outlet.

5.5.1 Modifications to the Model

Three sources of error are identified as potential contributors to this discrepancy. The first is clogging in the pressure drop and reaction channels, caused by KOH crystal

precipitation and KCl salting respectively. The second is the possibility that some of the output gas is sucked through open pores in the gas-liquid separator rather than exiting through the gas outlet. The third is the documented uncertainty in the kinetics rate coefficients k_2 and k_3 that are lumped into the pooling coefficient k_* in Equation 3.27 [42]. Each of these three error mechanisms is discussed below; it will be seen that only the uncertainty in the pooling rate coefficients provides an adequate explanation of the discrepancy between the baseline model and the results.

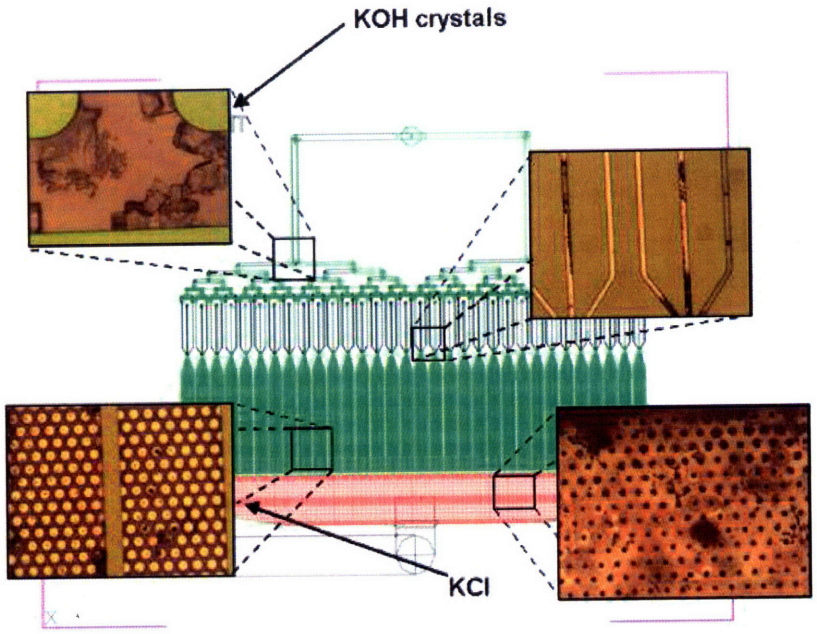

Figure 5-9: Clogging was observed at several points in the microSOG.

Clogging of the flow channels is observed under two general conditions: when the chip operates for long periods of time with moderately high ratios of chlorine to BHP, and when the chip operates even for short times with particularly high ratios of chlorine to BHP. During operation, clogging is evidenced by a pressure rise on the gas feed lines for a given mass flow rate of feed gas. It is not surprising that clogging occurred in some of the runs. The microSOG was designed to operate with a ratio of BHP to chlorine that corresponds to a 10:1 ratio of peroxide ions to chlorine as compared with a many tens to one ratio that is used to prevent clogging in macroscale SOGs; a lower ratio corresponds to more efficient reactant usage. At lower ratios the product solution becomes oversaturated and begins to precipitate

KCl. In these experiments the chip is usually operated with a ratio of peroxide ions to chlorine in the range of approximately 3.7 to 13. It is reasonable to expect that some clogging would occur under these conditions, and to expect that increasing the BHP flow rate by a factor of two for a given chlorine flow rate would reduce or eliminate the clogging. The occurrence of clogging in some conditions and not in others also means that some of the runs may be considered to be a better indication of clog-free operation than others. In general, the data that are taken towards the beginning of a given day's measurements, that are not accompanied by a rise in gas feed pressure for given mass flow rate, and that are taken at higher ratios of peroxide ion to chlorine are considered to be the most reliable data. When the fifteen runs are judged according to these criteria, the four runs that yielded unphysically high extrapolated values of $O_2(a)$ at the chip's outlet are found to suffer from the least clogging. It is therefore expected that clogging will not provide an explanation for the observed discrepancy. In addition, the expected effect of clogging is not to increase the concentration of $O_2(a)$ at the chip's outlet, but rather to decrease it. For a given mass flow rate set by the mass flow controllers, the effect of clogged channels like those shown in Figure 5-9 is to increase the gas and liquid velocities within the remaining channels. Additionally, some channels may be so clogged that they are completely prevented from producing $O_2(a)$. Clogging reduces the reactants' residence time in the channels so that less $O_2(a)$ would be produced. Since the observed discrepancy is in the other direction (anomalously high concentrations), and since the runs with anomalously high concentrations are relatively free of clogging, clogging is rejected as an explanation for the observed discrepancy.

The other two potential sources of error (loss of $O_2(a)$ through the capillary separator and error in the pooling rate coefficient) are assessed by including them in a revised microSOG model and assessing whether including these effects could remove the discrepancy. In order to ensure that clogging is not affecting the comparison between model and experiments, the comparison is made only for the four runs that were deemed to be the most free of clogging and for which the discrepancy was largest. Two revisions to the baseline model are necessary. A fluidic circuit analogy is used to

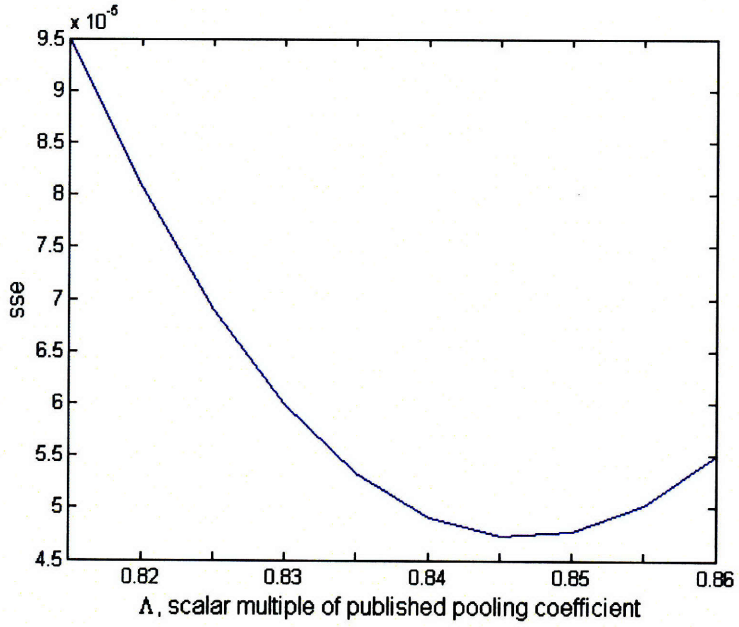

Figure 5-10: Sum of squared errors for runs 1, 2, 6, and 7 plotted against the scalar parameter Λ.

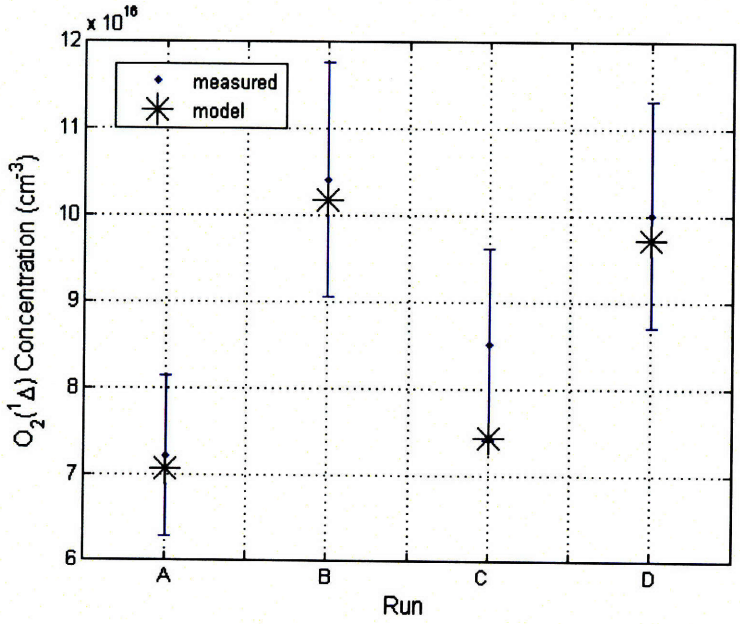

Figure 5-11: Best fit of runs 1, 2, 6, and 7 to the adjusted constant Λk_*.

estimate the percentage of gas that is sucked through the separator holes along with the liquid waste. The fluidic circuit assumes incompressible, fully developed flow in both the liquid and gas phases with a variable number of open holes N. The resulting loss of gas through the liquid separator is then accounted for in the calculation of the flow rates in the gas exit flow path. The model is also modified to account for the uncertainty of the pooling rate coefficients by scaling the effective pooling rate coefficient $2k_3+k_2$ (or equivalently, k_*) by a variable parameter Λ. In order to determine the best values for Λ and N, both parameters are varied independently and the sum of squared errors between the model's predicted concentrations at the measurement point and the measurements themselves are calculated for the four highest confidence runs. The best agreement between the kinetics model and the measured data, shown in Figure 5-10, occurs when Λ is chosen to scale k_* down to 84.5% of the published value and gas leakage through the capillary separator is negligible. These corrected values for the rate coefficients fall within the error bars of the cited source reference for the kinetic constants [42]. Figure 5-10 shows a pronounced change in the error as the scalar multiplier Λ is varied. This is not a unique minimization in the two dimensional (Λ, N) space. Similar minima are obtained for nonzero values of N, but they correspond to still smaller values of the pooling rate coefficient. The best agreement occurs (and minimum modification to Λ from one is necessary) when N approaches zero, suggesting that the occasional gas bubbles that were observed flowing through the separator's liquid outlet line have a negligible effect on the measurement. In other words, if significant O_2(a) flow were sucked in by the separator, the flow velocity in the gas outlet would be still smaller. As a result, k_2 and k_3 would also need to be even smaller to give physically meaningful predictions at the chip's O_2(a) outlet. However, it is possible to have a small gas-liquid separator leak and still have pooling rate coefficient values that fall within the error bars of [42] and yield essentially the same minimum error. As was described before, only a small fraction of the separator seems to be covered by the dynamic wetting front of the liquid by-products. Given the pressure difference applied across the capillary separator, even a small number of capillaries (5% of the total number) that were not filled with liquid would have

been enough to suck in most of the O_2(a) and prevent any observation of O_2(a) at the measurement point. The experimental performance suggests that the separator worked as designed, and the capillaries that didn't appear to be used during operation were nonetheless plugged with a stationary film of BHP that was put in place when BHP was first flowed through the chip. In all cases, the pressure difference across the separator is not enough to overcome the surface tension effects and clear the capillaries of liquid to allow for penetration of gas into the liquid exit flow.

5.5.2 Results with Adjusted Constant

The adjusted value for the pooling rate coefficient k_* is used to calculate molar flow rates per unit of reactor volume and power in the O_2(a) flow as well as the chemical efficiency and O_2(a) concentration at the chip's gas outlet. These values are shown in Table 5.5. The superscripts e and m respectively refer to extrapolated at model values at the microSOG outlet. The maximum chemical efficiency at the chip's gas outlet is determined to be 78% (+21%/-43%). This is theoretically consistent with a chlorine conversion rate of 100% and a yield of 78%, a chlorine conversion rate of 78% and a yield of 100%, or anywhere between. The lack of quantitative mass spectrometer data makes independent determination of the yield and chlorine utilization impossible. However, given that some pooling losses must have taken place between the end of the reaction channels and the chip's gas outlet, it is reasonable to conclude that this corresponds to a chlorine utilization of near 100% and a yield of about 78%. This yield is in line with state-of-the-art jet SOG generators, which have been reported to perform with yields as high as 73% [28], [36]. High yield is particularly important in COIL reactors because some O_2(a) is consumed in the dissociation of I_2 and, of the remainder, only O_2(a) above the threshold yield of about 7% can contribute at all to laser output in a COIL system; incremental increases above the onset of lasing offer significant increases in power because of the dynamics of the COIL system. A comparison of O_2(a) molar flow rate per unit volume between the microSOG and other technologies is given in Table 5.6. The maximum molar flow rate of O_2(a) per unit reactor volume is about $6.7\text{x}10^{-2}$ mol/L/s. This value includes that part of the

volume of the microSOG that hosts the pressure drop channels, reaction channels, and capillary separator; its boundaries, which are illustrated in Figure 5-12, do not include any volume that is devoted solely to single-chip packaging or the volume that is devoted to chip cooling. For the geometry of the microSOG, the reaction volume is 2.18 x 10^{-4} L. The per volume flow rate compares favorably with the molar flow rate of $O_2(a)$ per unit of internal reactor volume as reported for various types of published SOGs as reported in the literature. The molar flow rate per unit of internal reactor volume for modern jet SOGs is about 0.13-0.17 mol/L/sec [28], [21], nearly three times as large as the molar flow rate per unit of reactor hardware volume reported here for the microSOG chip. However, it should be noted that the microSOG volume includes the pressure drop channels as well as some of the surrounding silicon, while the jet SOG values only take the internal reaction volume into account. Using the jet SOG metric, the per-volume $O_2(a)$ molar flow rate of the microSOG is 0.19 mol/L/sec. It is the belief of this author that the molar flow rate per volume excluding the hardware is a less relevant metric because it may overstate the compactness of a given SOG implementation. Specifically, a SOG could have a very high $O_2(a)$ flow rate per internal reaction volume, yet require so much auxiliary hardware that its use in a scaled up system becomes impractical.

5.6 MicroSOG Power Extraction

The power carried by the flow of $O_2(a)$ at the microSOG gas outlet may be estimated from the molar flow rate extrapolated to the gas outlet and the energy of the $O_2(a)$ molecule, which is 94 kJ/mol. The resulting values for power in the flow are reported in Table 5.5. The maximum per chip power in the output flow is 1.37 W. Assuming a threshold yield of 7% and a typical COIL power extraction efficiency of 80% [47], the power in each microSOG's $O_2(a)$ flow is predicted to source about 1 W of laser output power when integrated into an appropriate COIL system. The original microSOG study [11] proposed using arrays of microdevices to construct COIL systems with power levels ranging from several kW to 100 kW. In that study, each

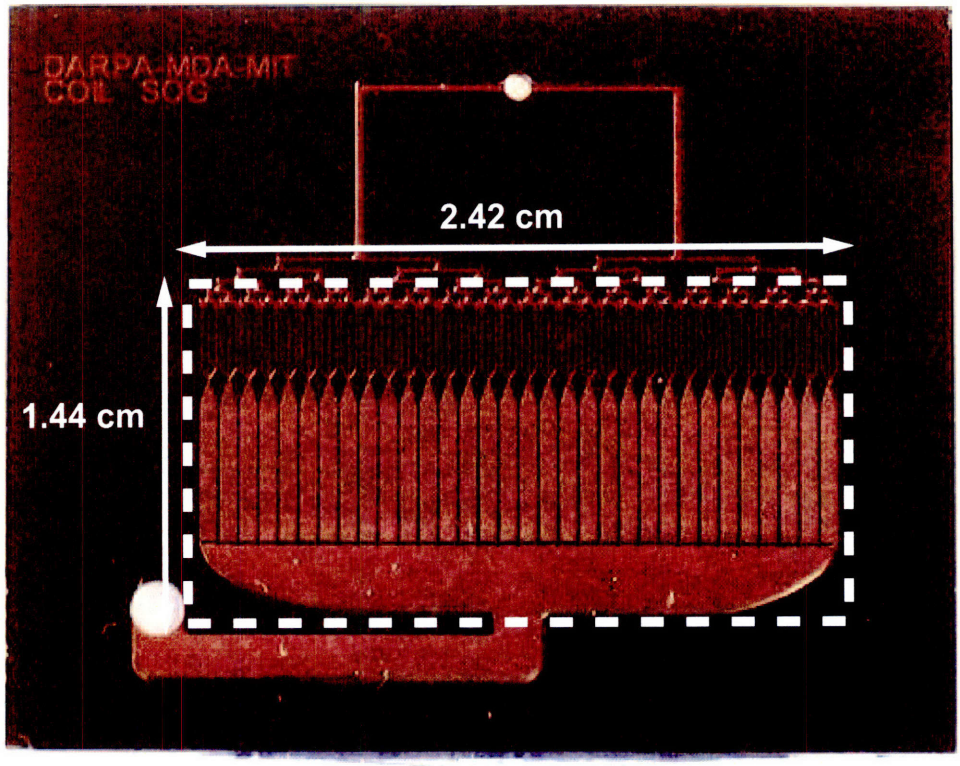

Figure 5-12: Definition of reactor area as it is used in Tables 5.5 and 5.6.

Table 5.5: Table summarizing extrapolated data with adjusted k_*. The superscript e denotes a value extrapolated to the microSOG gas outlet, while the superscript m denotes a model prediction.

Run	$[O_2(a)]^e$ x $10^{17}cm^{-3}$	E^e_{chem}	E^m_{chem}	P^e Watts	Molar Flow^e x 10^{-4}mol/L/sec
1	5.13 +2.19/-2.65	0.70 +0.3/-0.6	0.71	0.615 +0.3/-0.32	299 +144.7/-154
2	5.64 +1.57/-2.52	0.78 +0.22/-0.35	0.77	1.02 +0.29/-0.46	500 +140/-224
3	2.15 +0.76/-0.54	0.2987 +0.105/-0.08	0.8	0.52 +0.19/-0.13	255 +90/-64
4	$\geq$3.14	>0.43	0.71	$\geq$0.38	>183
5	1.76 +0.69/-0.47	0.23 +0.09/-0.06	0.76	0.31 +0.12/-0.08	149 +58/-40
6	$\geq$7.14	>0.48	0.63	$\geq$0.84	>410
7	8.48 +2.33/-4.74	0.78 +0.22/-0.44	0.72	1.37 +0.38/-0.77	669 +184/-374
8	1.63 +0.42/-0.34	0.22 +0.06/-0.05	0.82	0.49 +0.13/-0.1	240 +61/-50
9	1.14 +0.24/-0.21	0.15 +0.03/-0.03	0.82	0.39 +0.08/-0.07	188 +39/-35
10	1.08 +0.21/-0.19	0.14 +0.027/-0.024	0.82	0.42 +0.08/-0.07	203 +39/-35
11	1.38 +0.31/-0.27	0.26 +0.06/-0.05	0.86	0.45 +0.10/-0.09	219 +50/-42
12	0.92 +0.17/-0.15	0.22 + 0.04/-0.04	0.88	0.38 +0.067/-0.064	186 +33/-31
13	1.28 +0.25/-0.22	0.32 +0.06/-0.056	0.85	0.56 +0.11/-0.1	271 +59/-52
14	1.39 +0.28/-0.25	0.34 +0.068/-0.061	0.85	0.6 +0.12/-0.11	292 +59/-52
15	0.75 +0.16/-0.14	0.18 +0.38/-0.034	0.80	0.16 +0.32/-0.03	78 +16/-14

Table 5.6: Comparison of molar flow rate values between the microSOG and macroscale SOG implementations [28], [21], [18], [41].

SOG Type	Molar Flow Rate (mol/L/sec) x 10^{-4}
Sparger	2.3
Disk-Type	87
Jet-Type (Zagidullin)	1670
Jet-Type (Rybalkin)	1323
microSOG (this work)	670

microSOG chip was predicted to drive 2.3 W of this power output. The difference between the predicted optimum performance and the performance demonstrated in the first microSOG chips is not surprising given that the chips have not yet been operated at their optimum operating point because of flow limitations in the initial test rig. It is expected that the performance of the microSOG chips will approach the predicted optimum performance more closely as they are demonstrated closer to their optimum operating point. In particular, it is expected that the output of $O_2(a)$ per chip will increase and that clogging will decrease when the chips are operated at higher BHP and chlorine flow rates and at higher BHP to chlorine ratios.

Chapter 6

Design of a Second-Generation MicroSOG Device

In this chapter a design for a second-generation microSOG is proposed. First the shortcomings of the original design are discussed, followed by the goals for the new design. Next, there is a discussion of the features included in the new microSOG. Finally, the physical model outlined in Chapter 2 is used to determine the expected performance of the new device.

6.1 Motivation

Although the original MIT microSOG performs favorably as compared to its macroscale competitors, the experimental results fell short of the predictions presented in [11]. Assuming that the theoretical chip had exactly the same dimensions as the fabricated device the gas outlet, $O_2(a)$ molar flow rate of 6.7 x 10^{-2} mol/L/sec is well below the theoretical limit of 0.37 mol/L/sec. Of course this limit may not be fully reachable because of unavoidable $O_2(a)$ deactivation and less than perfect Cl_2 conversion. Still, the current results leave significant room for improvement.

The gap between results and theory can be attributed to two factors: an inability to operate at optimal flow rates due to packaging constraints and an under use of the reactor area due to the non-uniform distribution of reactants to the packed bed

channels. The optimal operating point in the theoretical study assumed a BHP flow rate three times higher (3 cm^3/min for 175 sccm of He:Cl_2 flow) than what was used experimentally. As a result the reaction ran near the solubility limit (defined as a $[O_2H^-]/[Cl_2]$ ratio of 10:1) which limited performance. Running at a higher liquid flow rate would not by itself increase the amount of O_2(a) produced; however it would diminish the effects of clogging in the device, thereby enabling longer residence times and O_2(a) molar flow rates. Also, it was not possible to operate the microSOG at gas flow rates higher than 200 sccm with the original testing rig. This value is far below the range proposed in [11], which included flow rates as high as 430 sccm. During the microSOG experiments, the gas delivery pressure steadily rose throughout operation, with failure occurring in the testing rig and package near 400 kPa.

Finally, a variety of flow behaviors are observed simultaneously across the chip during operation, which suggests that the pressure drop channels were not uniformly distributing the reactants to the packed bed channels. This behavior has two causes. First, the gas velocity in the pressure drop channels was so high that the incompressibility condition was violated. Even at the relatively low gas flow rate of 100 sccm, M_{gas} reaches a value of 0.3. With such high velocities, the linear relationship between pressure drop and flow rate no longer exists. Second, etch-related depth variation in the pressure drop channels caused the flow rates between individual reaction channels to diverge.

With these challenges in mind, the microSOG is redesigned with the following goals:

- A device with pressure drop channels that can handle the original maximum gas flow rate (430 sccm) while maintaining laminar, incompressible flow;
- A device that runs at a 12:1 $[O_2H^-]$:Cl_2 ratio to reduce the occurrence of clogging;
- A device that achieves a higher molar flow rate per unit volume than the last design, while still maintaining a reasonable pressure drop (below 400 kPa) and a high Cl_2 utilization.

6.2 Proposed Design

The following section contains the details of the proposed design. New dimensions for the features are given, along with a discussion comparing them to their analogs in the original design.

6.2.1 Pressure Drop Channels

The pressure drop channels can be modified in two dimensions: width and length. The depth must be kept equal to the width for Equation 3.29 to remain valid. The incompressibility condition is regulated by the cross sectional area of the channels. Figure 6-1 illustrates the rise in Mach number as a function of gas flow rate and width. It is clear that for high flow rates the channels need to be at least 50 microns wide to keep M_{gas} below 0.3. Increasing the width beyond 50 microns would further reduce the gas velocity, but could also require them to be longer and increase the overall reaction volume.

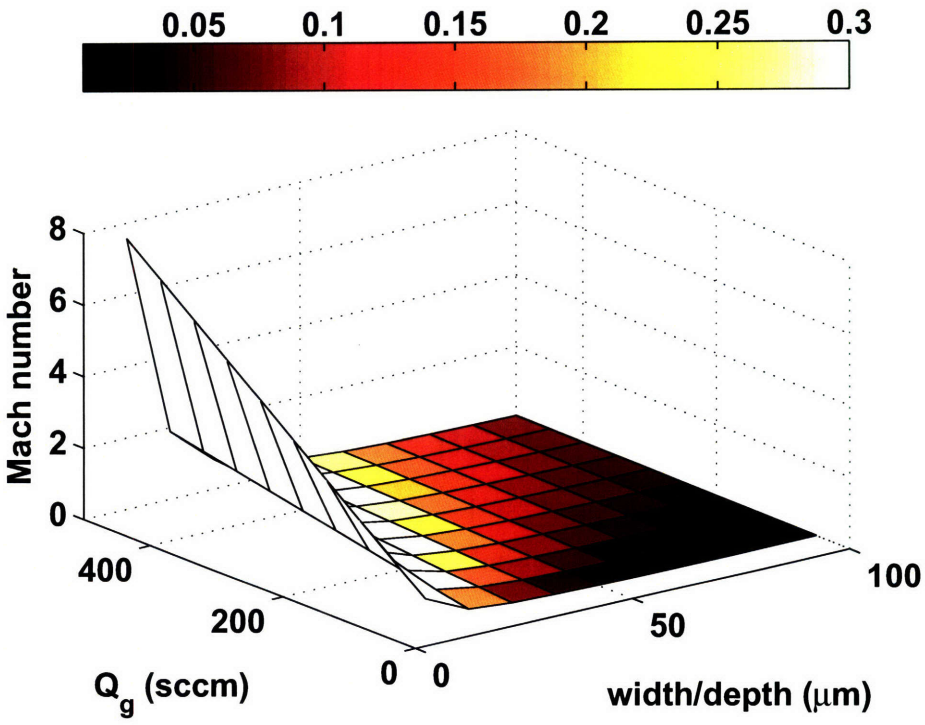

Figure 6-1: Mach number for various gas flow rates and cross-sectional geometries.

Because of the linear relationship between ΔP and flow rate described in Equation 3.29, the pressure drop channels in the original microSOG were designed to dominate the system hydraulics (by absorbing most of the pressure drop). However, the observed performance suggests that they performed this task poorly, as evidenced by the non-uniform regime behavior described earlier. Part of the solution to this problem lies in their fabrication. In the first-generation microSOG build the measured depth variation in pressure drop channels is $\pm$ 5% from a nominal value of 20 μm, which results in a $\pm$ 15% variation in flow rate between reaction channels at the best performing experimental operating point. Doubling the depth of the reaction channels will reduce the DRIE related variations. Previous work at MIT has shown that etch variation between channels can be reduced to as little as $\pm$ 2% at similar depths [2].

Now that the width and depth for the channels have been chosen, the length can be selected to achieve the desired pressure drop ratio over the reaction channels. It should be noted that this section has been focused on the gas rather than liquid pressure drop channels because the incompressibility issue was only seen in the gas phase. The liquid channels will have an identical width and depth, and a length chosen to match the gas pressure drop at the target flow rate of 430 sccm.

6.2.2 Reaction Channels

Along with pressure drop channels, the reaction channels also bear some responsibility for the non-uniform flow regime behavior observed during the experiments. The control problem discussed in the previous section can be solved by either increasing the pressure drop across the pressure drop channels and leaving the reaction channels alone, or by simply decreasing the drop across the reaction channels. Decreasing the pressure drop across the reaction channels is the more attractive option because it will make the chip easier to package and operate.

Before the discussion of the optimization, a short discussion about the contact area per unit volume a is necessary. Because all of the operating points have high ratios of gas to liquid reactants, annular flow is always assumed. Equations 3.41 and 3.42

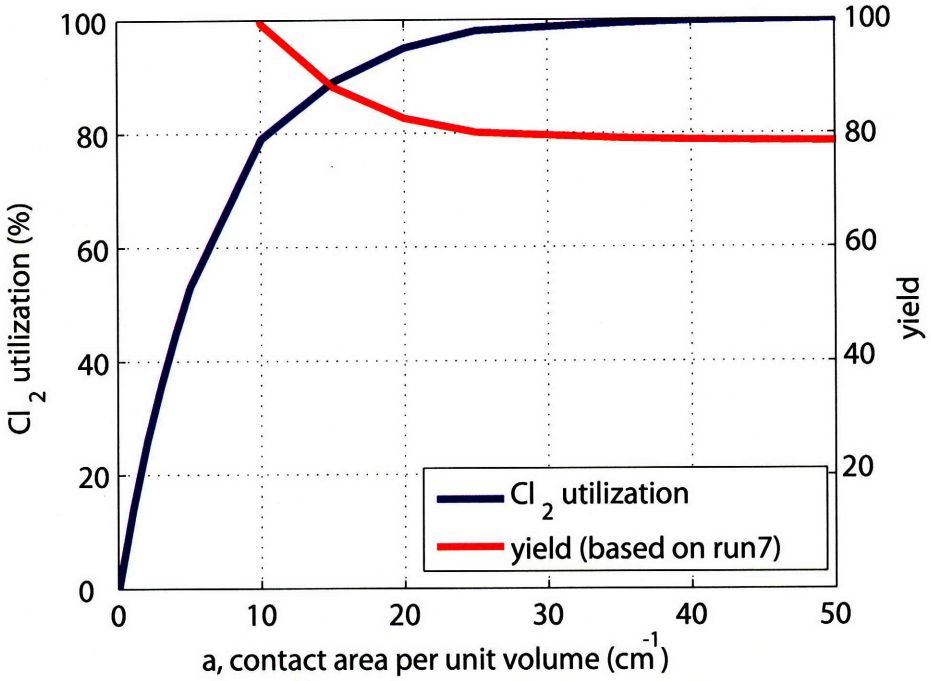

Figure 6-2: Yield and chlorine utilization versus a.

predict a range of values between 20 and 40 for the original microSOG geometry. The data of Chapter 5 can be used to discern the true value of a in this range. Figure 6-2 shows the Cl_2 conversion rate predicted by the model for a values ranging from 0 to 50. The conversion rate is based on the operating point used in run 7 of Chapter 5. The plot also shows the associated yield given the E_{chem} value of run 7, 0.785. It is important to note that yield values in excess of 100% are nonphysical. Because of the inevitability of O_2(a) deactivation, it is believed that the Cl_2 utilization of run 7 was near 100%, while the yield was closer to 78%. Since the model predicts Cl_2 utilization values of 95% and 99.7% for this operating point, it is very likely that the true value of a is in fact between 20 and 40. Therefore, for the purposes of the redesigning the reaction channels, a will be assumed to be the average between the minimum and maximum values of Equations 3.41 and 3.42.

The reaction channels are optimized by modifying their dimensions and then examining the consequences in terms of pressure drop and O_2(a) production. The degrees of freedom in this process are length, width, depth, and packing. The depth is held at 340 μm, since that value was effective in masking the effects of gravity in the original microSOG. The post diameter D_p is kept at 70 μm, because of the previous fabrication success at that size. The width is fixed to be eight times the value of post pitch δ; this is done to to ensure a fixed number of posts exist in the direction perpendicular to the reactant flow. The length is varied between 1 and 7 cm. A range of lengths exceed the reaction length of the previous design is chosen because of the target Q_g value is much higher than the gas flow rates used in the experiments of Chapter 5. Lastly, the post pitch δ is varied between 90 μm and 140 μm.

Figure 6-3 illustrates how the chemical efficiency of the microSOG varies with changes in the pitch and reactor length. This figure, along with the rest of the data in this section, evaluates the reaction channel performance for a gas flow rate of 430 sccm and a liquid flow rate of 8.9 ml/min. The maximum performance occurs at the surface crest, which corresponds to a reaction length of approximately 2 cm and a pitch between 115 and 140 microns. At shorter reaction lengths not all of the Cl_2

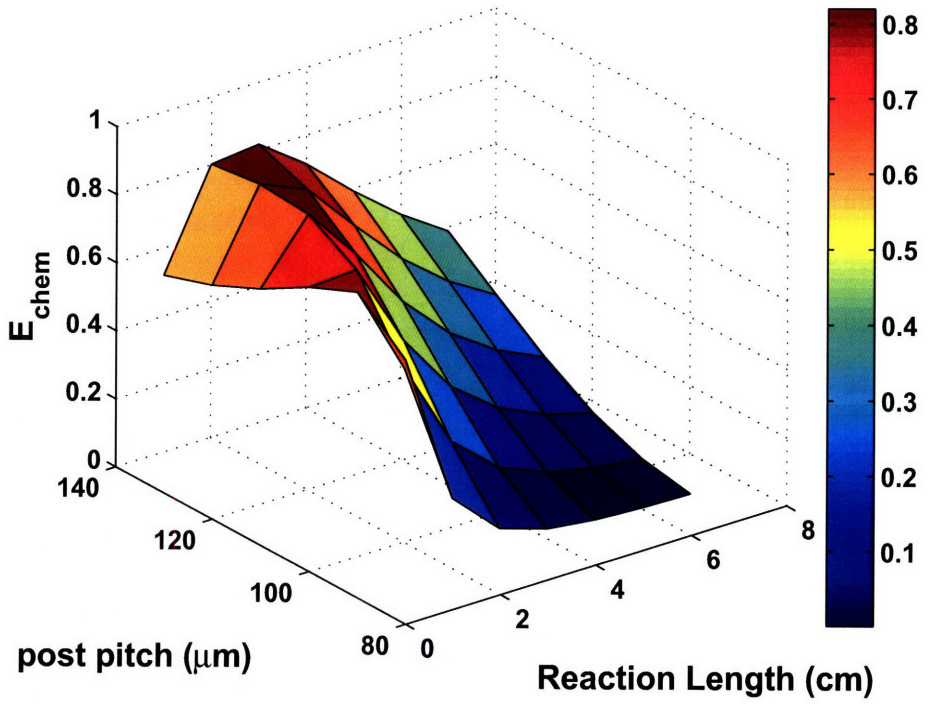

Figure 6-3: Chemical efficiency for different reaction channel geometries.

has been consumed, while significant $O_2(a)$ deactivation occurs with longer reaction channels. Although E_{chem} is an important microSOG metric, it is also important to maximize the $O_2(a)$ output per unit volume. In fact the point of highest chemical efficiency described above does not produce the highest molar flow rate per unit volume in the parameter space. However, that point, which occurs at a reaction length near 1 cm and a pitch of 100 μm, has a low Cl_2 utilization, which would be unacceptable in a scaled-up COIL system.

A third important metric is the the reaction channel pressure drop. Ideally the pressure drop would be as low as possible, allowing the chip to be easily packaged. Figure 6-4 illustrates the effect of pitch and channel length on pressure drop. As expected, channels with closely packed posts and longer lengths have higher drops. Fortunately, the area of the parameter space with high chemical efficiency exhibit pressure drops at or below 50 kPa. Once a reaction channel geometry is selected, the length of the pressure drop channels can be selected to give them the desired factor of hydraulic control over the reaction channels.

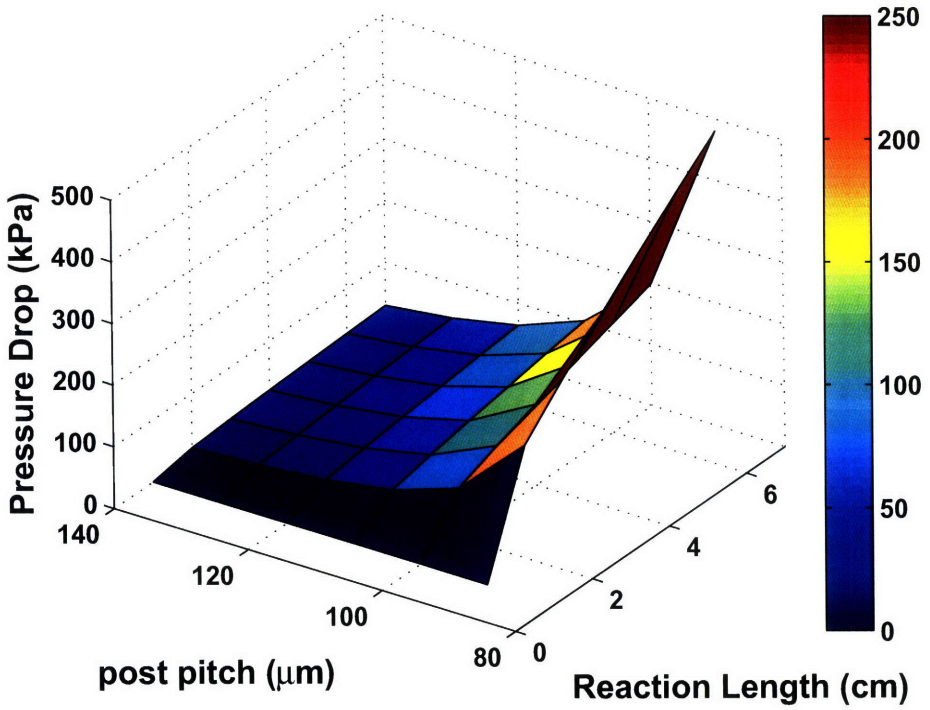

Figure 6-4: Pressure drop as a function of reaction channel geometry.

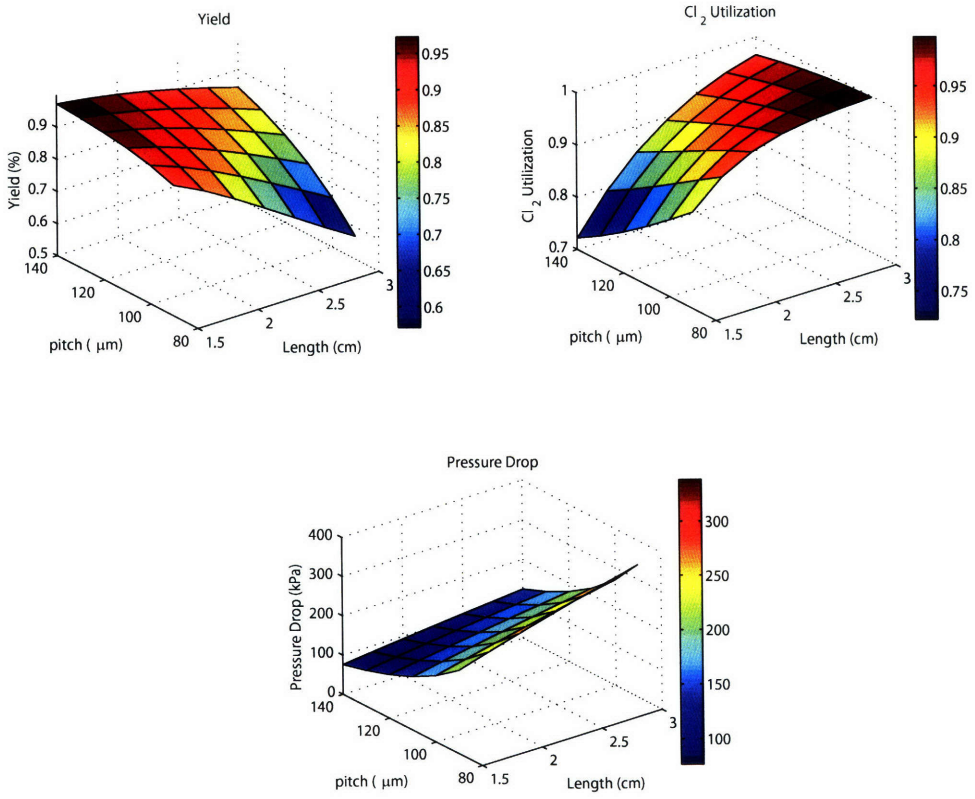

Figure 6-5: Simulation results for parameter sub-space.

The simulation data shown in Figures 6-3 - 6-4 indicate that the best performing area of the parameter space is located between pitches of 115 μm to 140 μm and reaction channel lengths of 1.5 cm to 3 cm. Within this smaller space the reaction channel performance was again evaluated in greater detail. The results are shown graphically in Figure 6-5. From this smaller space, the reaction length of 2.25 cm and pitch of 135 μm are chosen for the reaction channel design. The species profiles along the reactant flow path are plotted in Figure 6-6. The abscissa of the plot spans the reaction channels, separator, and exit lengths of the chip. The solution is not unique; the designer must balance the competing desires of high yield, high chlorine utilization, and low pressure drop when making a selection. The changes in geometry between the new and old channels are summarized in Table 6.1. The new reaction channels, which are longer, wider, and less packed than their predecessors, are still able to produce more $O_2(a)$ per unit volume because the of their higher reactant throughput. Additionally, the 12:1 O_2H^-:Cl_2 ratio will significantly reduce the clogging problems that plagued the previous experiments.

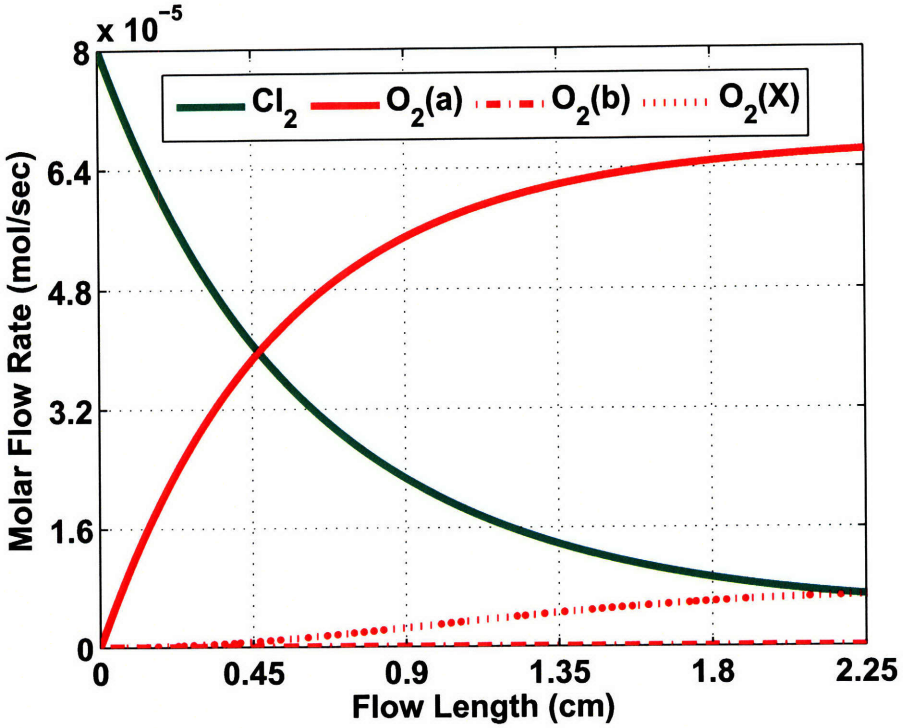

Figure 6-6: Molar flow rates of the Cl_2 and O_2 species as a function of flow length in the proposed microSOG design.

Table 6.1: Comparison of dimensions and performance in the old and new reaction channels. * - data refers to the best performance demonstrated in the original microSOG.

	old*	new
a (cm^{-1})	50 (assumed)	17
post diameter (μm)	70	70
post pitch (μm)	90	135
channel width (μm)	630	1080
channel depth (μm)	340	340
channel length (cm)	0.6	2.25
ΔP_{rxn} (kPa)	36	16
ΔP ratio	4.6	6
O_2(a) flow per vol (mol/L/s)	$6.7x10^{-2}$	$9.9x10^{-2}$
E_{chem} (%)	78	83

Table 6.2: Comparison of dimensions in the old and new pressure drop channels

dimension	old	new
width (μm)	25	50
depth (μm)	20	50
$length_{gas}$ (μm)	2428	4860
$length_{BHP}$ (μm)	2750	5230
Δ P_{BHP} (kPa)	652	97
Δ P_{gas} (kPa)	688	97
Δ $Q_{L,G}$ (%)	30	14

Now that the reaction channel dimensions have been chosen, the length of the pressure drop channels can be selected. The gas and liquid pressure drop channels are respectively sized to be 0.49 cm and 0.52 cm long, resulting in a pressure drop ratio of 6:1 between them and the reaction channels. A comparison between the old and new dimensions of the pressure drop channels is given in Table 6.2. The values in the table assume that both designs are operating at a gas flow rate of 430 sccm and a liquid flow rate of 8.9 cm^3/min. The per volume molar flow rate in Table 6.1 reflects the new pressure drop channel geometry. The value also considers the gas-liquid separator and exit length, which are both described in the next section.

6.2.3 Gas-Liquid Separator and Exit Length

Because the new version of the microSOG runs at a $[O_2H^-]$:$[Cl_2]$ ratio of 12, the gas-liquid separator requires increased liquid capacity. For the maximum BHP flow rate of 8.9 ml/min, 6700 pores would be needed, assuming the original pore geometry. However, by allowing for larger pore diameters, the separator flow capacity can be significantly increased. An increase in diameter from 20 μm to 30 μm raises the capacity of an individual pore by a factor of 5, according to Equation 3.45. It is important to note that the factor of 10 in Equation 3.45 changes to 12 in this case, because of the new $[O_2H^-]$:$[Cl_2]$ ratio. In contrast the maximum pressure drop associated with a non-zero contact angle meniscus, described in Equation 3.44, is only reduced by 33%. Therefore, approximately 1300 of the new pores are needed to accomodate the larger liquid flow rate. The new design contains 2000 pores, providing a buffer from liquid spillage into the gas outlet. The pitch between the pores is kept at 90 μm, resulting in a total separator area of approximately 3.84 cm x 0.05 cm.

A second change in the new design is the shape of the exit length. For the new microSOG, the gas exits the chip 0.1 cm after the separator region, rather than traveling through the elbow-shaped exit length of the old design. This change reduces the post channel flow length from 1.9 cm to 0.15 cm in the direction parallel to the reaction channel flow, greatly reducing the degree of O_2(a) deactivation in the chip.

6.2.4 Cooling Channels

Since the cooling channels already exceeded the required thermal capacity in the original design, they are simply resized to accomodate the new reaction channel area. Their extraction capacity is then recalculated. The new channels fit completely underneath the reaction channels, which are substantially longer in the proposed device. The convective heat transfer from the reaction channels in to the silicon is modeled using the Whitaker correlation [57], while the convective transfer from the silicon into the coolant is estimated with the Sieder-Tate correlation [51]. The relevant changes in the cooling channel geometry are summarized in Table 6.3. The values in the table

Table 6.3: Dimensions for the old and new cooling channels.

	old*	new
# of channels	19	20
width/depth (μm)	300/300	300/300
length (cm)	2.4	3.84
Heat In (W)	8.8	8.8
Max Heat Removed (W)	9.3	11.4

assume an ambient temperature of 293K and a coolant temperature of 263K.

6.3 Performance

The new microSOG design is conceptually illustrated in Figure 6-7. The device features longer and wider reaction channels, resulting in a larger overall die size of 5 cm by 4.3 cm.

The per hardware volume $O_2(a)$ molar flow rate of $9.9x10^{-2}$ is nearly a 50% improvement over the demonstrated performance of the original microSOG. Put another way, the new design increases the $O_2(a)$ molar flow rate per unit hardware volume by a factor of 4.55 while requiring only 3.1 times more reactor hardware volume and 4.3 times more gas reactant flow. The increase in per volume $O_2(a)$ molar flow rate has three causes. First, the proposed design has a slightly lower chlorine utilization (93%) than the original microSOG, which the model suggests had between 95% - 99% for experimental run 7. The lower conversion rate is an effect of the reaction channels being optimized for the highest possible E_{chem}, which is a product of utilization and yield. The second cause is a smaller post-reaction channel flow length. The elbowed gas exit path is removed from the new design, and wider pores dramatically reduce the area of the gas-liquid separator. Finally, some of the improved performance is due to the lower pressure drop across the reaction channels, which reduces $O_2(a)$ deactivation. The effect of pressure on the $O_2(a)$ output can be understood by examining the terms of Equation 3.13. The first and second terms respectively represent the creation and destruction of $O_2(a)$. The first term varies linearly with pressure while the second term has a quadratic pressure dependence. It is believed that the design

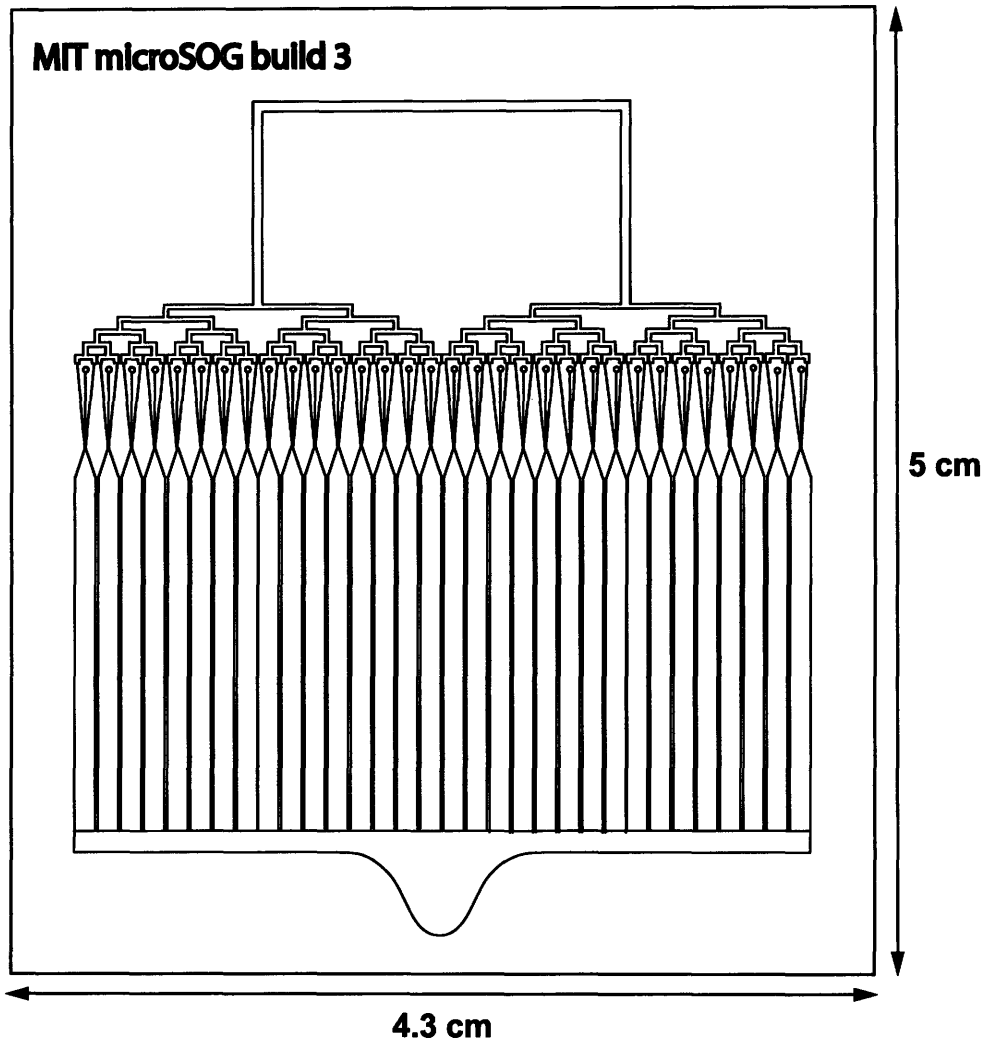

Figure 6-7: Conceptual drawing of the proposed microSOG device.

proposed here relies on relatively slow flows and long residence times to effectively mix the reactants. If this is true it may be possible to design an efficient reactor with smaller per channel flows and denser packing. However, such a reactor may require dimensions and packing densities that are impossible to realize with current microfabrication technology.

The molar flow rate value reported for the proposed device still lags the literature value for jet SOGs given in Table 5.6; however the discrepancy is simply a function of how the volume is calculated. Using the same method of Rybalkin, where only the internal reaction volume is considered, the $O_2(a)$ molar flow rate rises to 0.33 mol/L/sec, which exceeds all published jet SOG values.

The maximum molar flow rate for the new design corresponds to 6.2 W of power in the microSOG output stream, which is twice the 2.3 W predicted in [11]. As was done in Chapter 5, if a threshold yield of 7% is assumed along with an 80% power extraction efficiency, each of the new microSOGs can be expected to provide 4.6 W of laser power.

Chapter 7

Conclusions and Future Work

This chapter summarizes the accomplishments of the thesis, and proposes several avenues for future study.

7.1 Key Results and Conclusions

The most important achievement of this thesis is the demonstration of MEMS technology as capable of handling the three functional requirements of $O_2(a)$ generation for the COIL application. Specifically, the high contact area per unit volume of the microSOG is utilized in order to mix the BHP and Cl_2 and produce $O_2(a)$. The array of pores included in the chip is able to separate the gas and liquid phases at both atmospheric and sub-atmospheric pressures. Finally, the incorporation of cooling channels as well as the high thermal conductivity of silicon allows the microSOG to successfully remove excess heat that originates from both the reaction channels and the outside environment.

Not only does the microSOG produce $O_2(a)$, it produces $O_2(a)$ at high enough quantities that the concentration is measurable after a significant amount of deactivation has occurred. Before the project began it was unclear whether a strong enough optical signal could be obtained to independently verify the presence of $O_2(a)$. This goal was achieved even though the first generation microSOG produces less $O_2(a)$ than was expected from the theoretical study of [11]. The measurements are also impor-

tant because they lead to the conclusion that the $O_2(a)$ deactivation coefficient k_*, which has been used for decades by the COIL community, is likely overstated in the literature.

This thesis also contributes to the COIL community by providing a physical model for understanding the physics of $O_2(a)$ generation at the microscale. Although the chemical model is based on prior work [11], [13], [14], it is enhanced by the inclusion of detachment yield and more accurate BHP parameters. The fluidic model will aid microSOG development by giving future designers an idea of what flow regime and contact area to expect as a function of the operating point and chip dimensions.

Finally, this thesis proposes a second-generation microSOG design. The new chip uses the physical understanding developed through experiments and modeling to potentially achieve $O_2(a)$ flow rates per unit reactor volume greater than any other published SOG. The simulated results of the new SOG along with the demonstrated experimental results of the first generation SOG both suggest that further development of MEMS technology for the COIL application is a worthwhile endeavor. The next section of this chapter presents some possible avenues for that future work.

7.2 Future Work

7.2.1 Reducing the Reaction Volume

The $O_2(a)$ molar flow rate per unit volume reported in Chapter 6 can be significantly increased by re-routing the flow path of the microSOG. Specifically the pressure drop channels, which alone account for nearly 20% of the reactor volume in the second-generation microSOG, could be twisted or bent to fit inside a more compact footprint. However, it should be noted that requiring the inlet and outlet ports at the single-chip level to fit inside a more compact area could create more challenges with respect to packaging.

7.2.2 Integration and Scale-up

After the next generation microSOG is fabricated and tested, the next logical step is to demonstrate several microSOGs working in tandem. In the theoretical study of [11], 7.1 kW and 110 kW COIL systems were considered. The COIL architecture proposed in that study is illustrated in Figure 7-1. The microSOGs and I_2 mixing nozzles are fabricated on wafers and vertically integrated along the gain length L_g of the optical cavity. The cavity considered was 50 cm long and 7 cm wide, and utilized two mirrors having reflectivities of 99% and 70%. Although the architecture

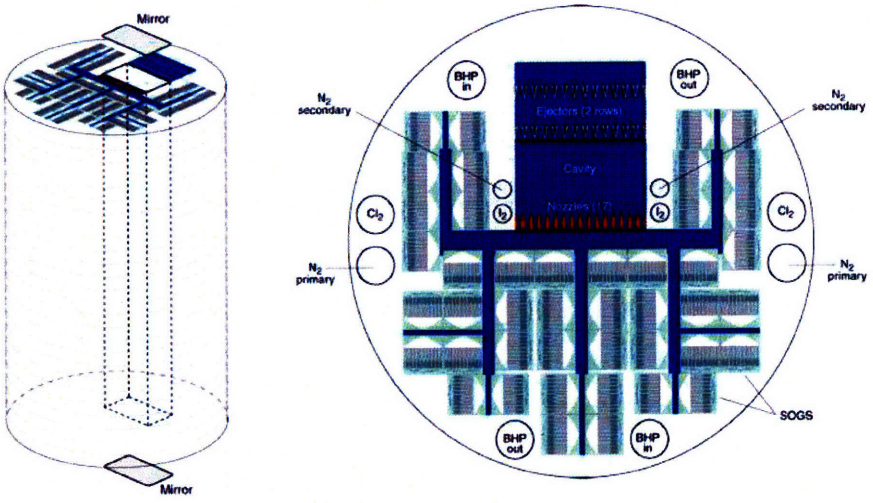

Figure 7-1: Illustration of microSOGs integrated into a full COIL system [11].

described in [11] requires thousands of microSOGs, positive laser gain could probably be achieved with several. One related issue that needs to be studied in detail is the thermal management in a scaled-up silicon SOG. At some point with bonded stacks of silicon microSOGs and nozzles, the isothermal approximation used in Chapter 3 is likely to break down.

7.2.3 Packaging and Materials

One of the great limitations for both generations of microSOG designs presented in this thesis was packaging. Had the package been able to handle higher delivery pressures, the amount of reactant throughput could have been increased. Therefore, some future microSOG work could focus on the implementation of high-pressure packaging for the device. One promising method would be connecting the lower end of the microSOG to a plate with Kovar tubing by a glass seal, described in [46]. Material compatibility tests would need to be conducted to assess whether this solution should be implemented with Kovar or another material. While it was not possible for this packaging solution to withstand the pressures associated with operating the microrocket (approximately 125 atm), it is highly probable that glass sealing would be robust below 10 atm, which is the pressure range of interest to the microSOG. An illustration of this packaging concept is shown in Figure 7-2. Additionally, coating or treatment of the rig materials for BHP resistance could be investigated. Silicon was made into a suitable microSOG through the deposition of a nitride layer. Perhaps an analogous process can be performed on the steel pipes and fittings of a future testing rig.

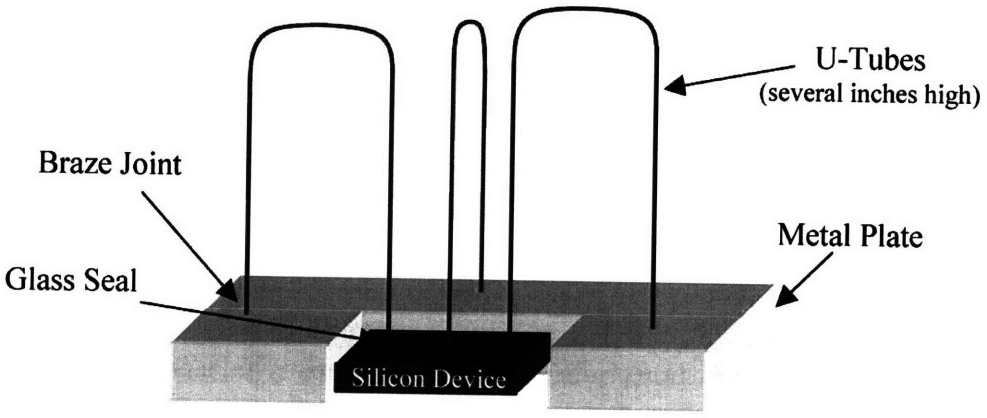

Figure 7-2: High pressure MEMS packaging concept from the MIT microrocket project [46].

7.2.4 Modeling and Kinetics

Many opportunities exist concerning improvement of the microSOG models. For example, the microSOG physical model assumes ideal plug flow in the channels. It would be interesting to employ a computational fluid dynamic (CFD) model to the microSOG reaction channels. CFD models have been used to simulate flow and estimate a in large-scaled packed bed reactors [39], [59]. Therefore, a CFD model could be used to test the accuracy of the geometric contact area model proposed in Chapter 3. The true a value of the a reaction channel could also be empirically verified by doing Cl_2 absorption measurements at the microSOG outlet. CFD tools could be used to model the pressure drop channels and reaction channels at extremely high flow rates. When the the Mach number M is greater than 0.3, the incompressibility assumption breaks down. So, computational tools could shed light on the regimes and mixing behavior of a microSOG with flows approaching sonic speeds.

7.2.5 MEMS-based jet SOGs

Due to the lack of detailed performance data on jet SOGs, it is worth investigating whether MEMS technology can improve the $O_2(a)$ molar flow rate per unit hardware volume for this technology. Because the droplet size can be controlled by the reactant flow rates, the jet technology offers dynamic control over the contact area per unit volume. A conceptual illustration of a MEMS jet SOG is shown in Figure 7-3. MEMS fabrication technology could be used to produce microscale orifices through which the reactant jets are created. The products of the SOG could then be separated using the same capillarity principle used in the microSOG.

7.2.6 Alternative Iodine Pumping

Finally, the $O_2(a)$ molecule is only important to the laser community as a pump source for the iodine gain medium. As such, it would be interesting the investigate other means of pumping I into $I(^2P_{1/2})$, and whether MEMS can be useful for this task. One variant of COIL is known as the All Gas Iodine Laser (AGIL) [37]. AGIL systems

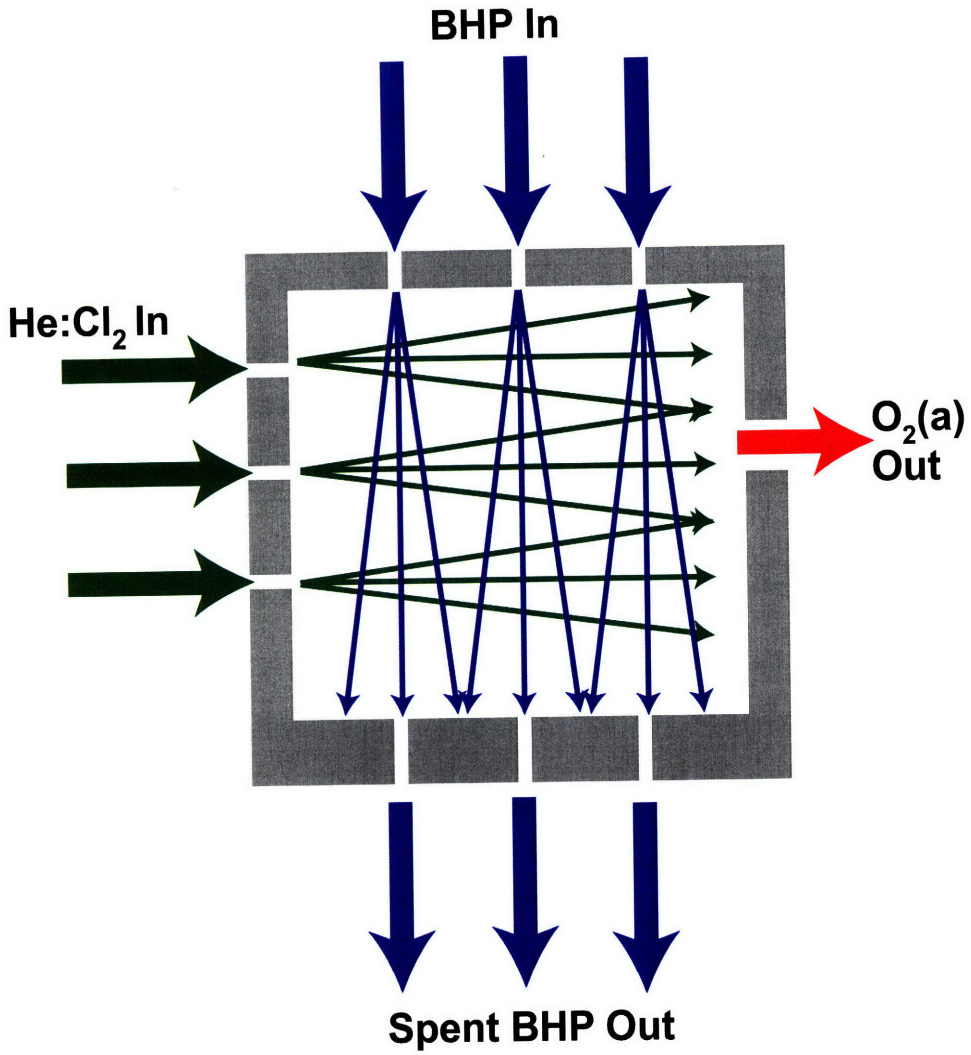

Figure 7-3: Conceptual view of a MEMS based jet SOG.

rely on singlet delta state NCl to pump iodine atoms into their excited states. Much like $O_2(a)$, $NCl(a^1\Delta)$ pumps its gain medium through collisions. The NCl molecule is a result of the all-gas reaction of Cl_2 and hydrazoic acid (HN_3). An all-gas reaction is would be advantageous in the airborne laser application as the total reactant weight would be diminished, although the tankage weight may increase. It would be useful to look at MEMS as a tool for efficiently mixing two gas phase reactants. The theoretical microCOIL assumes the use of a MEMS nozzle for mixing $O_2(a)$ and I_2, so there is no fundamental reason why one could not also be used to mix $NCl(a^1\Delta)$ and I_2. However, it remains to be seen whether $NCl(a^1\Delta)$, which is highly toxic and explosive, can be used safely in an academic setting.

7.3 Final Thoughts

Based on the work in this thesis and the potential of the areas outlined in the Future Work section, it is clear that MEMS-based COIL is a viable method for building high power oxygen-iodine lasers. The success to date is but another instance of using small-scale devices to tackle a large-scale real world problem.

Appendix A

Mask Set

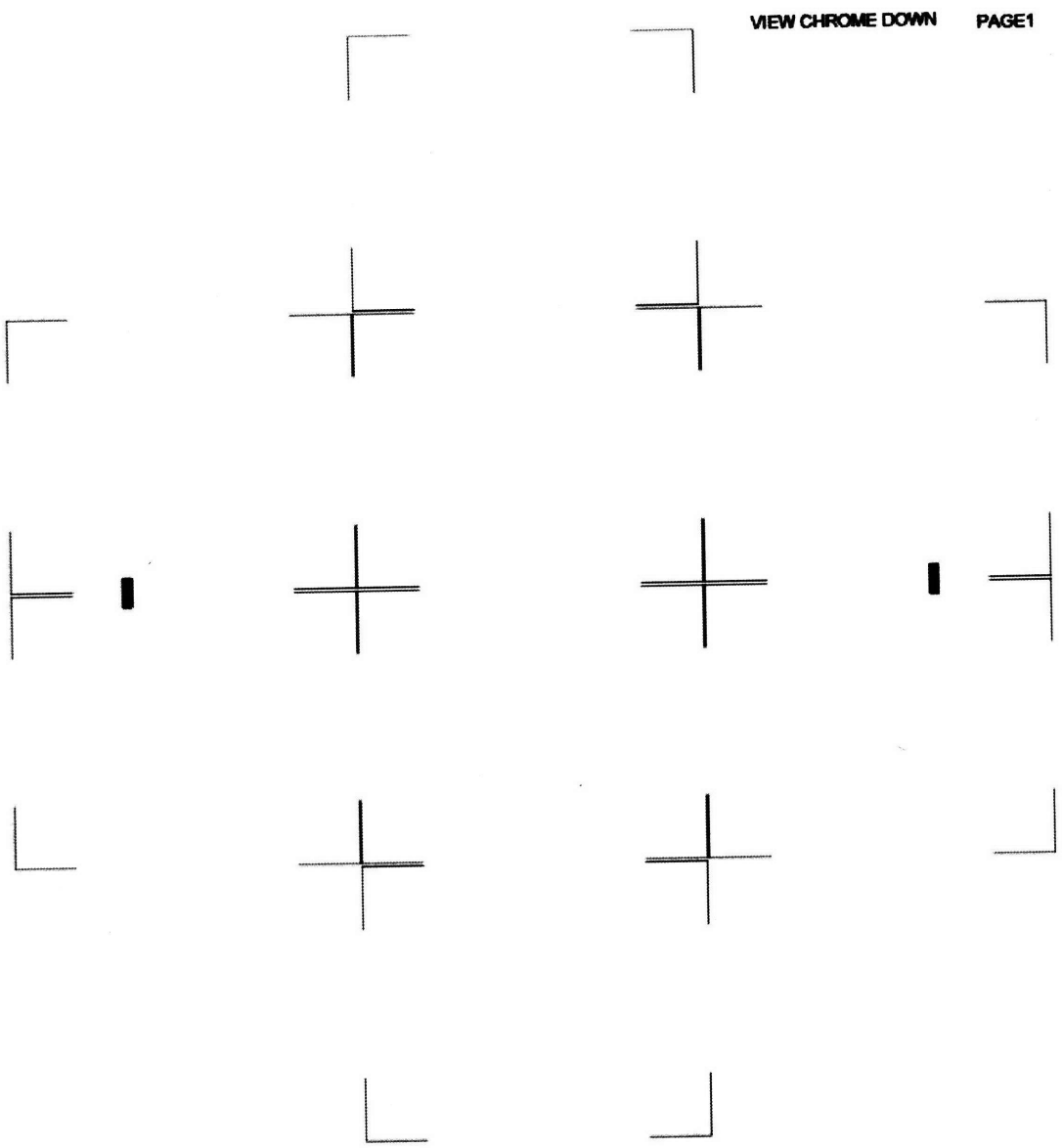

ALIGNMENT

VIEW CHROME DOWN

MASK TYPE D
(DARK BACKGROUND/
CLEAR FEAUTES)

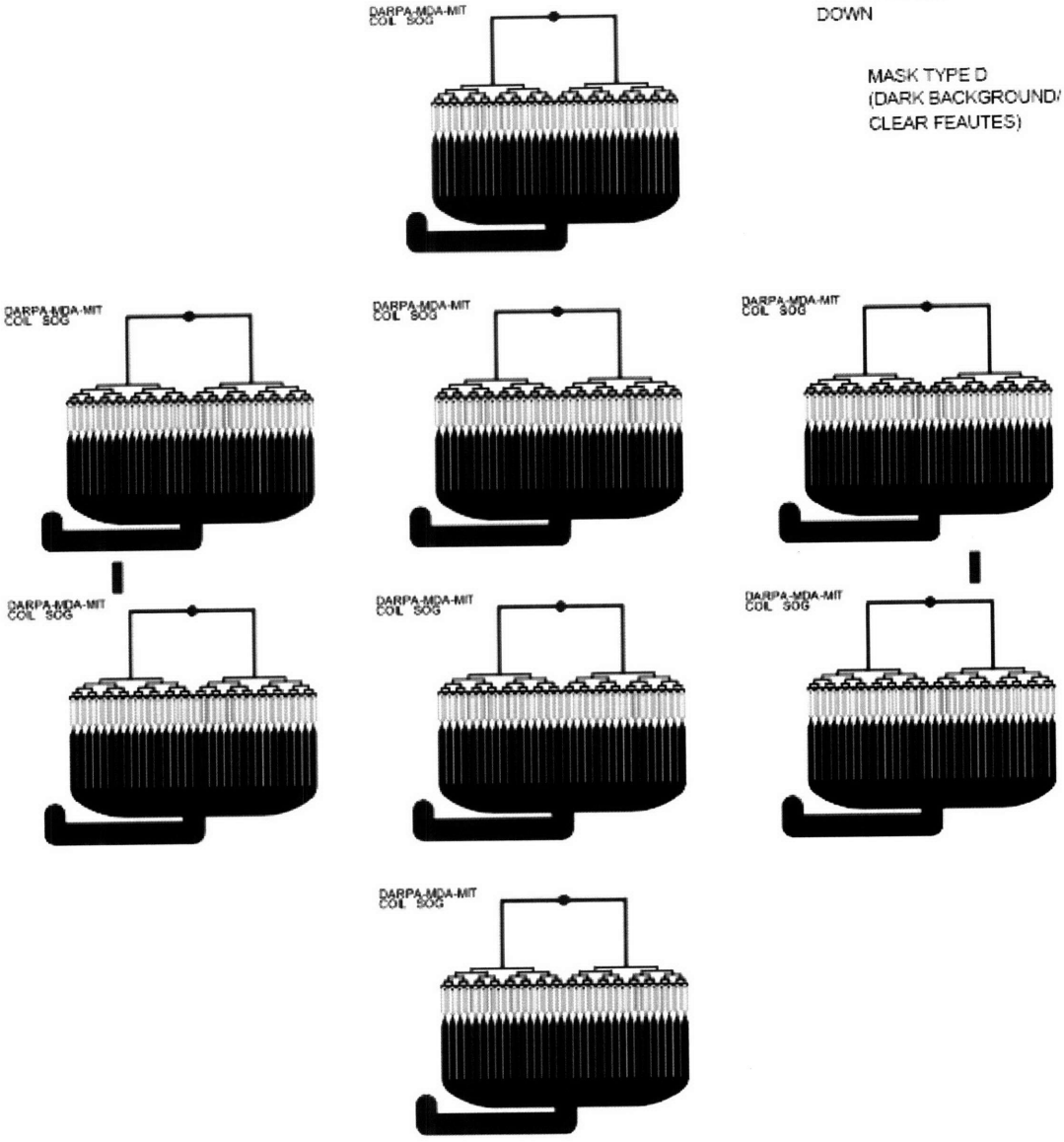

NITRIDE STRIP


VIEW CHROME DOWN
PAGE 4
MASK TYPE D
(DARK BACKGROUND/
CLEAR FEATURES)
POST ETCH

VIEW CHROME UP

PAGE 8

MASK TYPE B
(DARK BACKGROUND/
CLEAR FEATURES)

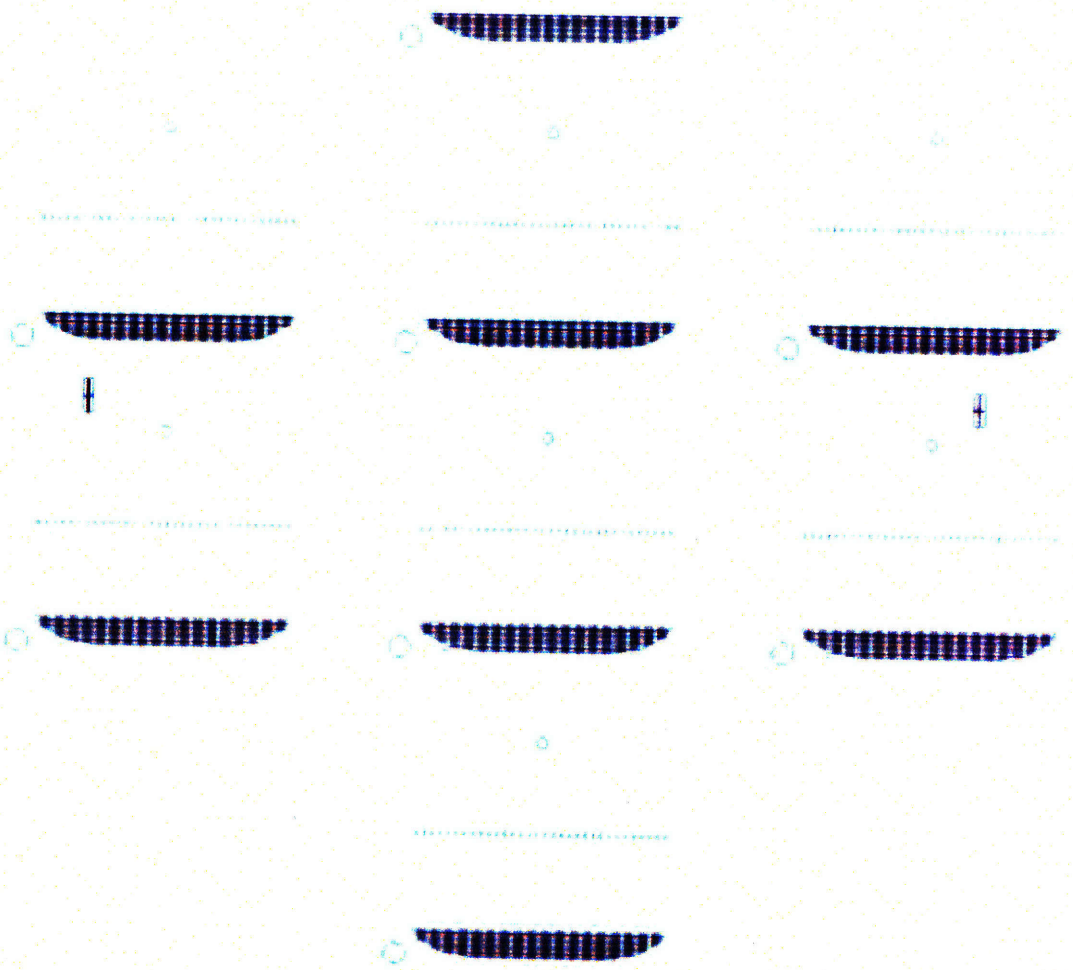

UPPER THROUGH HOLES

VIEW CHROME DOWN

PAGE 8

MASK TYPE D
(DARK BACKGROUND/
CLEAR FEATURES)

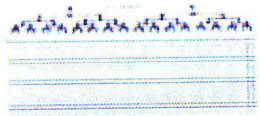

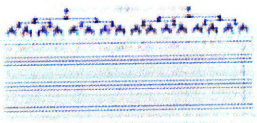

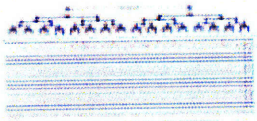

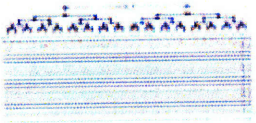

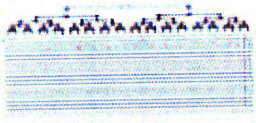

MASK TYPE B
(DARK BACKGROUND/CLEAR
FEATURES)

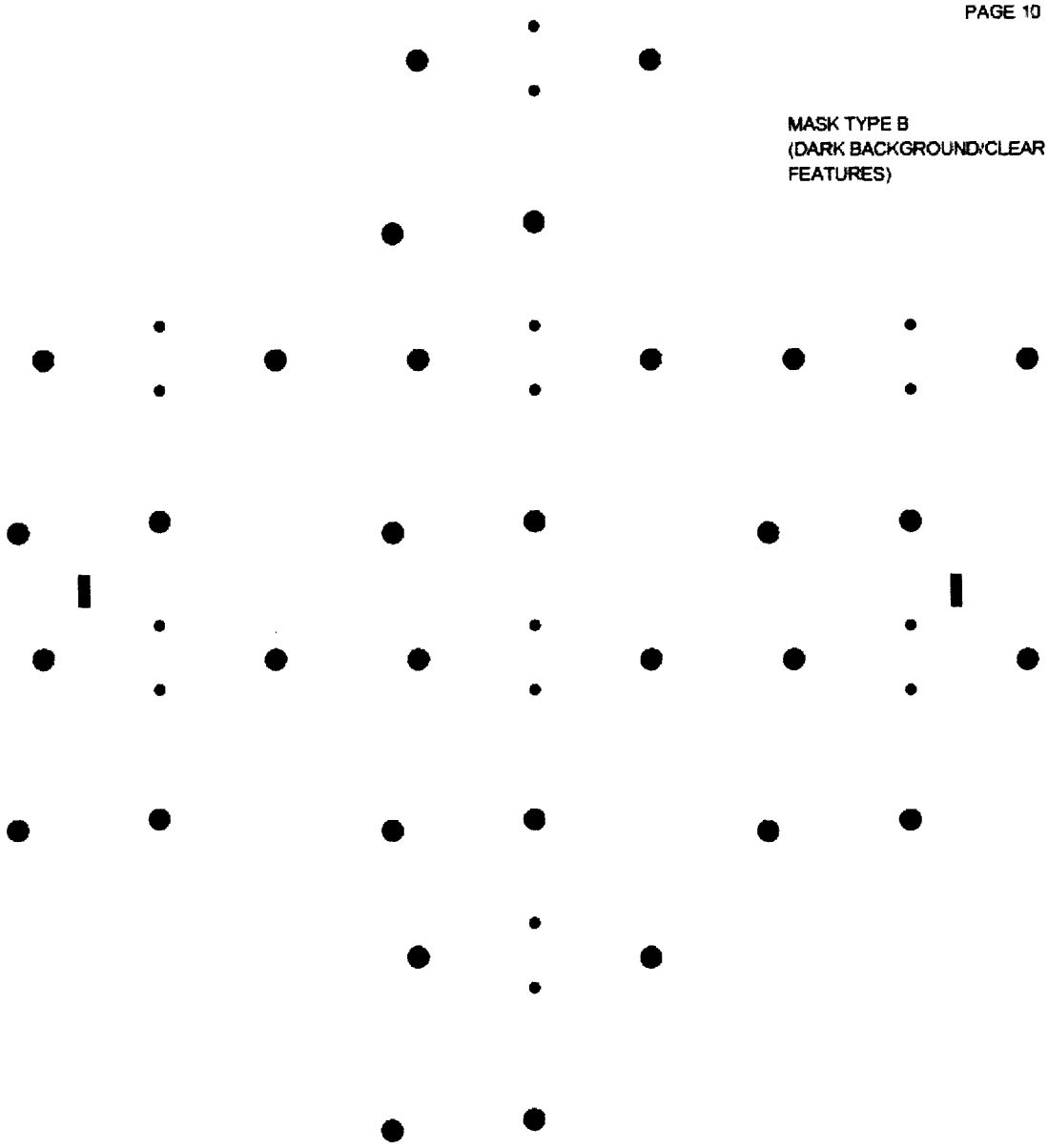

LOWER THROUGH HOLES

Appendix B

Fabrication Process

This section provides an in-depth view into the microSOG fabrication process. Cross-sections are provided, along with a detailed spreadsheet outlining the process steps. The fabrication methods are discussed in greater detail in [19].

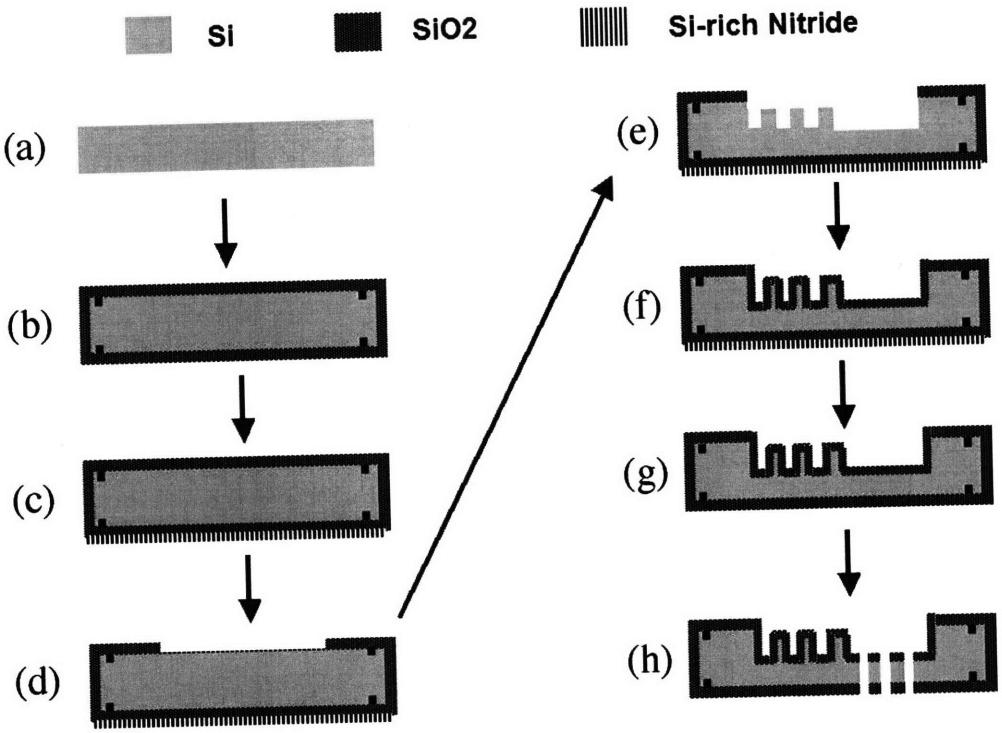

Figure B-1: (Process flow by which the middle wafer of the microSOG is fabricated. The process flow starts with a DSP p-Si <100> wafer (a). The wafer is oxidized, and alignment marks are transferred to both sides of the wafer (b). The wafer is then coated with 0.5 m of LPCVD silicon-rich silicon nitride, and the film on the top of the wafer is stripped using an RIE step (c). The silicon oxide film on the top surface of the wafer is patterned with the layouts of the pressure drop channels, the liquid inlet manifold, the reaction channels without the packed beds, and the region occupied by the separator (d). The reactor packed beds and an opening in the region that the separator will eventually occupy are then patterned in a resist and etched by DRIE (e). The photoresist film is stripped, and the features etched on the silicon oxide film on the top surface of the wafer are transferred to the silicon substrate using a DRIE step, while etching 20 μm. The wafer is then oxidized (f), and the silicon-rich silicon nitride on the backside of the wafer is stripped using hot phosphoric acid (g). Finally, the layouts of the chip ports and the capillary separator are patterned in a resist on the back side of the wafer, are transferred into the back-side silicon oxide layer with BOE, and are transferred to the silicon with DRIE. The photoresist film is stripped (h) [19].

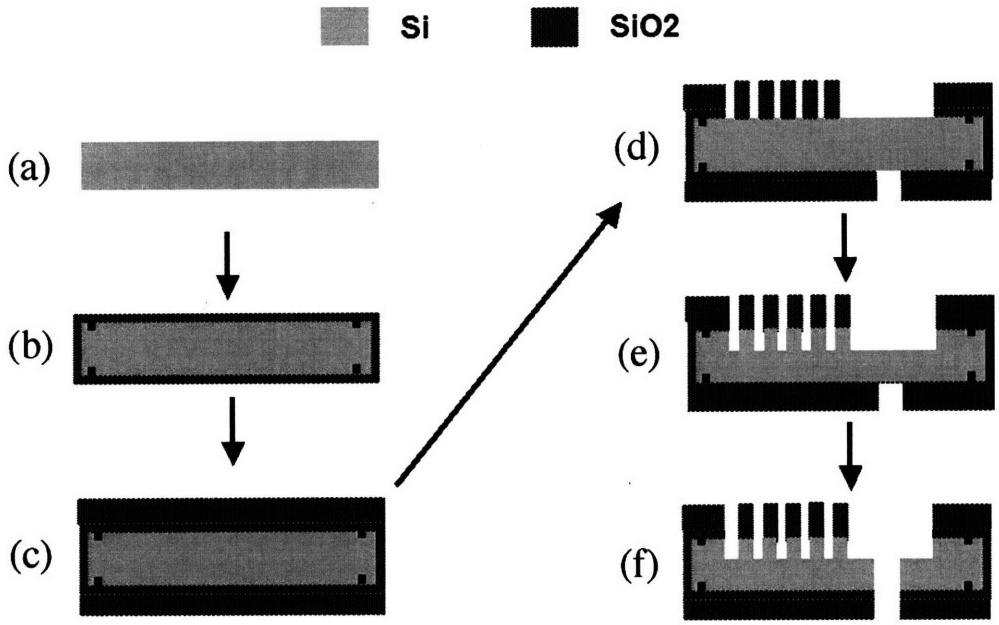

Figure B-2: Process flow that fabricates the bottom wafer of the SOG. (a) The process flow starts with a DSP p-Si <100> wafer. (b) The wafer is oxidized, and alignment marks are transferred to both sides of the wafer. The wafer is then coated with 4 μm of PECVD silicon oxide on both sides of the wafer and annealed at 950 C in a nitrogen atmosphere (c). The resist is applied to both sides of the wafer. The resist film on the top of the wafer is patterned photolithographically with the layouts of the heat exchanger and the gas inlet manifold, whereas the bottom film is patterned with the layouts of the chip ports. The layouts of both resist films are transferred to the silicon oxide films using a cycled RIE plasma recipe (d). The top of the wafer is then etched with DRIE to a depth of 325 μm (e). Finally, the wafer is flipped over and mounted on top of a quartz wafer, and the chip ports are etched with DRIE (f) [19].

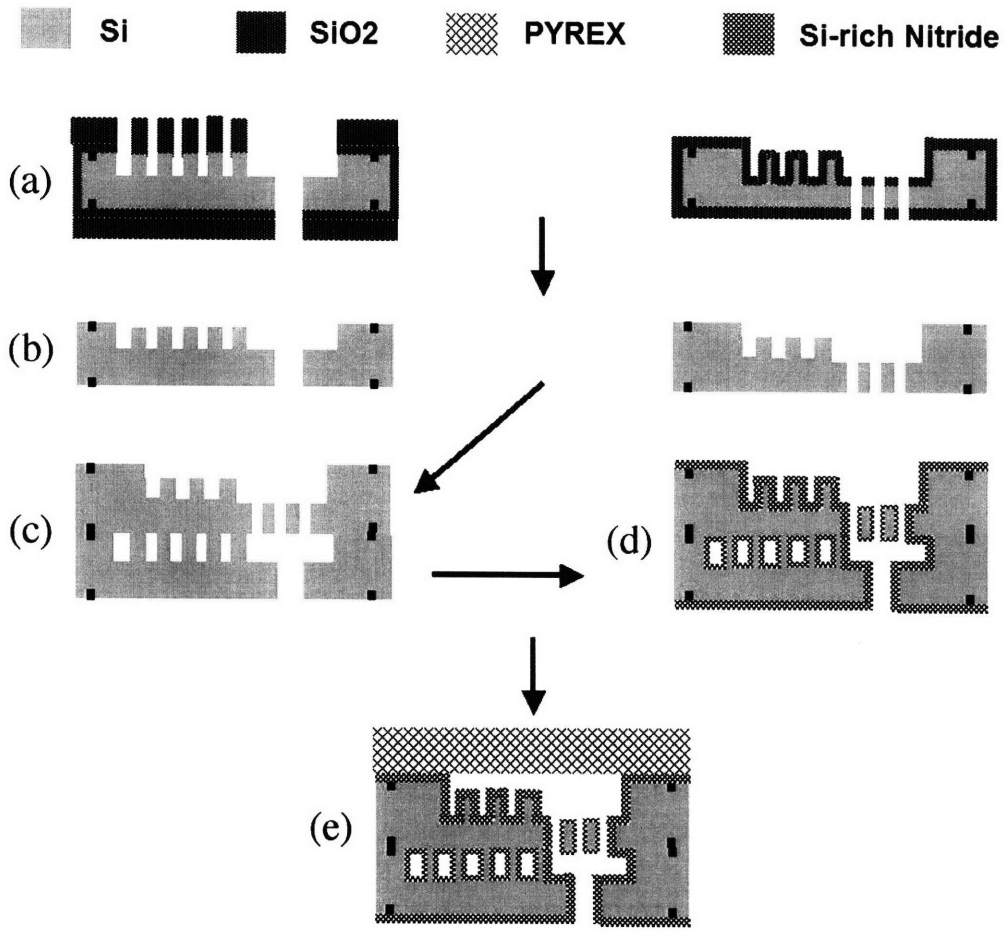

Figure B-3: Process flow to finalize the fabrication of the microSOG. The microfabricated middle and bottom wafers (a) are immersed in a 49% HF bath to strip the silicon oxide films (b). The two silicon wafers are fusion bonded (c). Then, a 0.4-μm-thick LPCVD silicon-rich nitride is conformally deposited on the silicon wafer stack (d). Next, the silicon wafer stack is anodically bonded to an unpatterned Pyrex wafer (e). The wafer stack is then die sawed to extract the SOG chips [19].

Microreactor Process Flow
Tyrone Hill, January 2005

Purpose: To fabricate a microchemical reactor for the creation of singlet delta oxygen.

Starting Materials: 2 DSP prime silicon wafers (6 inch), 1 pyrex wafer

Wafer 1

	Step #	Lab	Process Step	Machine	Chemicals	Recipe	Color	Comments
	1	TRL	piranha clean	acidhood/a2	sulfuric acid, peroxide	3:01	green	
	2	TRL or ICL	RCA				brown	
	3	TRL or ICL	oxidation	tubeA2/5C	N/A	std	brown	0.2 um thin oxide
Alignment Marks	4	TRL	HMDS	HMDS-TRL	N/A	std	green	thin resist recipe
	5	TRL	spin on resist	TRL coater	OCG 825-20CS	STD	"	1um, positive resist
	6	"	prebake	oven	N/A	N/A	"	90C, 30 minutes
	7	"	expose	EV1	N/A	STD	"	alignment mark mask
front	8	"	develop	N/A	N/A	N/A	"	OCG-934 (3.5-4 min)
	9	"	postbake		N/A	N/A	"	90C, 30 minutes
	10	"	spin on resist	TRL coater	OCG 825-20CS	STD	"	1um, positive resist (backside)
	11	"	postbake2		N/A	std	"	30 min, 120C
	12	"	oxide etch (BOE dip)	acidhood/a2	BOE	N/A	"	
	13	ICL or TRL	etch	sts2(3) /LAM			"	alignment mark etch (fronstide)
	14		remove resist	acidhood/a2	piranha		"	
	15	TRL	HMDS	HMDS-TRL	N/A	std	"	thin resist recipe
	16	TRL	spin on resist	TRL coater	OCG 825-20CS	STD	"	1um, positive resist
	17	"	prebake	oven	N/A	N/A	"	90C, 30 minutes
back	18	"	expose	EV1	N/A	STD	"	alignment mark mask
	19	"	develop	N/A	N/A	N/A	"	OCG-934 (3.5-4 min)
	20	"	postbake		N/A	N/A	"	90C, 30 minutes
	21	"	spin on resist	TRL coater	OCG 825-20CS	STD	"	1um, positive resist (backside)
	22	"	postbake2		N/A	std	"	30 min, 120C
	23	"	oxide etch (BOE dip)	acidhood/a2	BOE	N/A	"	
	24	ICL or TRL	etch	sts2(3) /LAM			"	alignment mark etch (backside)
	25		ash					
	26		remove resist	acidhood/a2	piranha			

Nitride deposition	27	ICL	nitride deposition	VTR			"	400 nm Si-Rich nitride (ER = 21 nm/min)
			nitride removal (front)	sts2(3)/LAM				

Nitride_strip	28	TRL	HMDS	HMDS-TRL	N/A	STD	"	thick resist recipe
	29	"	spin on resist	TRL coater	AZ4620 resist	STD	"	10 um thick resist
	30	"	prebake	oven	N/A	N/A	"	90C, 60 minutes
	31	"	expose	EV1			"	mask - pd + rxn channels
	32	"	develop	N/A	AZ440 developer		"	3.5-4 minutes
	33	"	postbake				"	90C, 30 minutes
	34	ICL or TRL	etch nitride layer	sts2(3)/LAM			"	

	35	TRL	etch thin oxide	acidhood or a2	BOE		"	short BOE dip
	36	TRL	remove resist	acidhood or a2	piranha		"	remove resist

	37	TRL	HMDS	HMDS-TRL	N/A	STD	green	thick resist recipe
pd_mask	38	TRL	spin on resist	TRL coater	AZ4620 resist	STD	"	10 um thick resist
	39	"	prebake	oven	N/A	N/A	"	90C, 60 minutes
	40	"	expose	EV1			"	mask - rxn channels (no pd)
	41	"	develop	N/A	AZ440 developer		"	3.5-4 minutes
	42	"	postbake				"	30 min, 90C
Etch rxn channels	43	"	etch	sts2(3)		jb-etch	"	define rxn channels (~90%) - 330 um
separator	44	"	remove resist	acidhood/a2	pihranha		"	
etch pd channels	45	"	etch	sts2(3)		jb-etch	"	short etch to define pd chan. (20um deep)
	46	"	ash	asher_TRL			"	~ 300nm of nitride should be left (~10 min etch)
	47		piranha					
	48	TRL	RCA	rca_TRL				
oxidiation/remove	49	TRL	oxidize	tubeA2			green	thin oxide to protect posts
SiN	50	ICL	revove back nitride	acidhood/a2			"	H3Po4 165C

attach to diesaw tape 51

through_holes	52	TRL	HMDS	HMDS-TRL	HMDS	HMDS	green	150 deg, 15 min
mask	53	"	Spin on 10 um resist (t	coater		AZ P4620	"	10um, positive thick resist, IFNS
	54	"	Pre-bake	oven		----	"	90deg, 30min
	55	"	Exposure	EV1		----	"	through hole mask
	56	"	Develop	photo-wet left	AZ440 developer		"	2min 20 - 30 sec
	57	"	bake	oven		----	"	90 C, 10 min
	58	"	etch oxide	acidhood/a2	BOE		"	
etch through holes	59	"	etch	sts2(3)	N/A	jb-etch	"	~#300 um etch
	60	"					"	
remove resist	61	"	cleaning	acidhood/a2	piranha		"	10 min
	62	"	ash	asherTRL				

Wafer 2

	Step #	Lab	Process Step	Machine	Chemicals	Recipe	Color	comments
	1	TRL	piranha clean	acidhood2	sulfuric acid, peroxide	3:01	green	
	2	TRL or ICL	RCA				brown	
	3	TRL or ICL	oxidation	tubeA2/5C	N/A	std	brown	0.2 um thin oxide
Alignment Marks	4	TRL	HMDS	HMDS-TRL	N/A	std	green	thin resist recipe
	5	TRL	spin on resist	TRL coater	OCG 825-20CS	STD	"	1um, positive resist
	6	"	prebake	oven	N/A	N/A	"	90C, 30 minutes
	7	"	expose	EV1	N/A	STD	"	alignment mark mask
front	8	"	develop	N/A	N/A	N/A	"	OCG-934 (3.5-4 min)
	9	"	postbake		N/A	N/A	"	90C, 30 minutes

	10	"	spin on resist	TRL coater	OCG 825-20CS	STD	"	1um, positive resist (backside)
	11	"	postbake2		N/A	std	"	30 min, 120C
	12	"	oxide etch (BOE dip)	acidhood/a2	BOE	N/A	"	
	13	ICL or TRL	etch	sts2(3) /LAM			"	alignment mark etch (fronstide)
	14		remove resist	acidhood/a2	piranha		"	
	15	TRL	HMDS	HMDS-TRL	N/A	std	"	thin resist recipe
	16	TRL	spin on resist	TRL coater	OCG 825-20CS	STD	"	1um, positive resist
	17	"	prebake	oven	N/A	N/A	"	90C, 30 minutes
back	18	"	expose	EV1	N/A	STD	"	alignment mark mask
	19	"	develop	N/A	N/A	N/A	"	OCG-934 (3.5-4 min)
	20	"	postbake		N/A	N/A	"	90C, 30 minutes
	21	"	spin on resist	TRL coater	OCG 825-20CS	STD	"	1um, positive resist (backside)
	22	"	postbake2		N/A	std	"	30 min, 120C
	23	"	oxide etch (BOE dip)	acidhood/a2	BOE	N/A	"	
	24	ICL or TRL	etch	sts2(3) /LAM			"	alignment mark etch (backside)
	25		ash					
	26		remove resist	acidhood/a2	piranha			

oxide deposition	27		deposition	sts-cvd				4 um PECVD oxide (both sides)

Cooling Channel	28	TRL	HMDS	HMDS-TRL	N/A	STD	green	thick resist recipe
Mask	29	"	spin on resist	TRL coater	AZ4620 resist	STD	"	10 um thick resist
	30	"	prebake	oven	N/A	N/A	"	90C, 60 minutes
	31	"	expose	EV1			"	cooling channels + gas channels + liquid res.
	32	"	develop	N/A	AZ440 developer		"	3.5-4 minutes
	33	"	postbake	oven			"	30 min 90C
	34	"	oxide etch	acidhood/a2	BOE		"	BOE dip to open up oxide windows
etch channels/	35	"	etch	sts2(3)		jb-etch	"	create features
reserviors	36	"	ash	asher_TRL			"	
	37	"	remove resist	acidhood/a2	piranha		"	

lower through	38	TRL	HMDS	HMDS-TRL	HMDS	HMDS	green	150 deg, 15 min
holes mask	39	"	Spin on 10 um resist (t	coater		AZ P4620	"	10um, positive thick resist, IFNS
	40	"	Pre-bake	oven		----	"	90deg, 30min
	41	"	Exposure	EV1		----	"	through hole mask
	42	"	Develop	photo-wet left	AZ440 developer		"	2min 20 - 30 sec
	43	"	Soft-bake	oven		----	"	90 C, 10 min
	44	"	etch oxide	acidhood/a2	BOE		"	
							"	
etch holes	45	"	etch	sts2(3)	N/A	jb-etch	"	~#300 um etch
	46	"					"	
remove resist	47	"	cleaning	acidhood/a2	piranha		"	
	48		ash	asher_TRL				

both wafers	1	TRL	HF to remove oxide	acidhood/a2			green	both wafers
	2	TRL	RCA clean wafers				"	
	3	"	fusion bonding	EV501-620			"	2500 N of force for 12 h; 1050 C for 1h in N2
nitride deposition	4	ICL	deposition				"	0.4 um nitide depostion over exposed Si
anodic bonding	5	TRL	bond pyrex to stack	EV501-620			"	anodic bonding
								1000 Volts; 1000 Newtons; 350 C
	6	ICL	dice wafers	diesaw				250 um blade

Appendix C

Experimental Protocol

This document details how to operate the experimental apparatus for reacting BHP with chlorine in the microSOG chip to produce $O_2(a)$.

C.1 Equipment

1. Adjustable wrench
2. 1/2", 7/16", 9/16" wrenches
3. small flat-head screwdriver (for adjusting set points)
4. 2 liter beaker, half full with water

C.2 KOH Preparation

1. Put 50 mL of water into a volumetric flask (the KOH solution is 50% water by weight; the density of water is 1 gm/mL)
2. Use a weighing dish to measure out 50 grams of KOH pellets
3. Slowly add KOH pellets to the water mixture, being carefully not to let the solution overheat.

4. After all of the pellets have been dissolved and the solution has cooled, use a rubber stopper to cap the flask.

C.3 Packaging

1. Place packaged chip into holder inside setup. Make all swagelok connections to cooling, gas, and liquid ports.

2. Turn on chiller. Immediately verify that no cooling leaks exist.

3. Set chiller to -15°C. Make sure that flow knobs for both chip and reservoir jackets are open, so that both are chilled. For mixing BHP, keep a jacket temperature of -10° to -15°C to minimize the rate of BHP decomposition. It is important to note that if the temperature is held too low, ice formation can occur, which may block liquid flow through the chip.

4. Load liquid reservoir with BHP. Loosen the six black nuts on the two sealing flanges. Remove the flanges, and lift off the lid. Prepare BHP solutions in accordance with the instructions of Chapter 4. Once liquid reservoir has been filled, replace the lid, sealing the flanges. Tighten the six black nuts with a 9/16" or adjustable wrench

5. At this point, make sure that all fluidic connections are made. Consult schematic of setup. Make sure that gas line, from supply to vacuum pump/vent, is connected. Make sure that the liquid line, from reservoir to collector to vacuum pump/vent, is connected.

C.4 Gas Flow Startup

1. Make sure that vent valves 2 and 3 are open.

2. Set plenum pressure, separator pressure, to 800 torr on controller unit.

3. Turn on plenum, separator controllers, on controller unit.

4. Open He valve.

5. Initiate He flow of 50 sccm on controller unit.

6. At this point, gas should be flowing through the He mass flow controller, into the ch ip, and out through the LN trap and vent valve.

C.5 Liquid Flow Startup

1. Make sure that the liquid reservoir is filled, closed, and sealed.

2. Close manual blow-off valve.

3. Open pumping gas (He) valve.

4. Open pressure control valve.

5. To start flow of pumping gas to reservoir, turn on pumping gas mass-flow controller.

6. Monitor the reservoir pressure (controller 1, channel 1). The pressure (in psig) should slowly rise towards the set point. There may an initial overshoot; allow 60 s for the pressure to stabilize. The stabilization should correspond to the observation of liquid flowing through the chip.

7. At this point, gas should be flowing through the chip, and liquid is being pumped (by He pressure) from the liquid reservoir into the chip. The next setp is to begin to reduce the separator pressure (providing suction to withdraw liquid phase out through the liquid exit line).

C.6 Reducing Separator Pressure

1. To reduce the separator pressure to below atmosphere, we need to divert gas flow from exiting the vent line to the vacuum pump. The first step is to set the separator pressure to 600 torr on the controller unit.

2. Close valve 2

3. At this point, gas should flow from the liquid collector, through the LN trap, past the closed vent, through the back-pressure controller, into the vacuum pump.

C.7 Reducing Plenum Pressure

1. Set plenum pressure to desired vacuum (e.g. 700 torr) on controller unit.

2. Close valve 3.

3. At this point, gas flowing from the chip to vent is being diverted to flow past the back-pressure controller, and into the vacuum pump. Please note that the back-pressure controllers have a tendency to over-shoot the set point, and may take several minutes to stabilize.

C.8 Attaining the Desired Set Point

1. Now that both the separator and plenum (gas outlet) are operating under vacuum, you can adjust the set points to the desired pressures. Keep in mind that both controllers will overshoot, and maintain a pressure difference of at least 40 torr at all times to prevent flooding of the liquid into the gas outlet.

2. Also, set the He gas feed rate to the desired value (controller 1, channel 1).

3. At the point all operating conditions should be at the desired levels. Plenum and separator pressure, He flow rate and chip temperature should be stable.

C.9 Opening Chlorine Supply Line

1. Open the lower left panel. Identify chlorine tank, cross-purge assembly, and regulator. Make sure all three valves are closed.

2. Open chlorine cylinder. On top of the cylinder is a stem and a valve. Turn the valve counterclockwise to open the tank.

3. Open the purge assembly to the chlorine regulator, by opening the red valve. Chlorine gas is now able to flow from the cylinder, through the purge assembly, into the chlorine regulator.

4. Open the valve on the regulator (the smaller, leftmost black valve). Now chlorine gas is exiting the regulator and flowing to the mass-flow controller.

5. Finally, open the green chlorine safety valve on the gas panel. Chlorine can now flow through the mass flow controller into the chip. This means that chlorine exposure is a risk be sure to wear a face shield. Also, ensure that adequate ventilation exists in the hood.

C.10 Running the Singlet Oxygen Reaction

1. On controller 1, channel 2, adjust chlorine set point to the desired flow rate.

2. Initiate chlorine flow on the controller box.

3. A faint bleach smell indicates a leak. If a leak exists, turn of the the flow controller, and close the green safety valve. Once the safety valve is closed, the gas is contained within the stainless-steel plumbing.

4. When finished collecting data, close the green safety valve.

C.11 Shutting Down the Experiment

If

- all the desired data is obtained,

- the BHP supply reservoir is empty and needs to be refilled,

- any BHP temperature has exceed 10°C for any reason,

the experiment needs to be shut down.

1. Change the plenum and separator set points to 800 torr on the controller box.

2. Turn of the vacuum pump.

3. Now that the vacuum pump is off, and both controllers are being ordered to let the system pressurize to 800 torr, the helium being fed to the chip is slowly raising the system pressure. However, given the total volume of the chip, tubing, and associated glassware is roughly 5 liters, and the maximum He flow rate is 200 ml/min, it would take roughly 30 minutes for the He flow to bring the system to atmospheric pressure. So, air can be used to speed up this process.

4. Crack open (slowly) the plenum vent (valve 3). This action allows air to be drawn into the plenum, raising the pressure. It should take approximately 1 minute for the gas outlet pressure to reach atmospheric levels.

5. Slowly open vent valve 2. This action allows air to be drawn into the BHP collector. Similarly, it should take around 1 minute to bring this side of the setup to atmospheric pressure.

6. Once both plenum and separator pressures are at atmosphere, the next step is stop liquid flow through the chip.

7. Turn off the liquid reservoir pressure controller (control box 2, channel 1). The pressure controller will now let the liquid delivery pressure drop back to 0 psig.

8. Turn off the pumping gas mass-flow controller. Helium is no longer needed to drive liquid into the chip.

9. Open manual vent for liquid reservoir-this will allow any excess pressure in the reservoir to escape.

10. Check the reservoir pressure (control box 21, channel 1) to ensure that the reservoir pressure is 0. Do not attempt to open the reservoir when it is under pressure.

11. If the pressure is 0 psig, loosen the six black securing nuts. Remove the sealing flanges and lid.

12. At this point, it is acceptable to turn of the chiller, dispose of the BHP, and close the Cl_2 gas line.

C.12 BHP Disposal

1. Remove glass liner from BHP reservoir. Pour the BHP into the 2 mL beaker.

2. Remove fittings/joints from BHP collector. Pour BHP out of collector directly into 2 mL beaker.

3. Carry the beaker to acid hood for neutralization and disposal. BHP should be handled as hazardous waste. For now, let diluted BHP rest in the hood while the chlorine line is being shut down.

C.13 Closing and Purging Chlorine Line

1. Check to make sure that (i) the Cl_2 mass flow controller is off, and (ii) the Cl_2 safety valve is tightly closed.

2. Open bottom left panel to access gas plumbing.

3. Close regulator valve (leftmost valve on cross-purge assembly).

4. Close red valve on cross-purge assembly.

5. Close valve on chlorine cylinder. Note that this is the exact opposite of the procedure for opening the chlorine line.

C.14 Final Tasks

1. Turn of He flow. Close the He regulator valve to prevent losses due to leaks. For long shutdowns, turn off He cylinder valve as well.

2. The back-pressure controllers utilize a very small valve to control the pressure; a combination of moisture, residual Cl_2 and BHP vapors can condense and plug this valve, preventing the system from being pumped down. To prevent this, cap off both the separator and plenum vacuum lines and shut down the vacuum pump. Let the vacuum pump pump both controllers down to 0-5 torr, and then turn it off. This procedure effectively sucks out any gas in the controller to prevent their clogging.

3. If the pressure controllers do plug, they can be disconnected from the setup, disassembled, and cleaned with a cotton swab wetted with ethanol or methanol.

Bibliography

[1] P. B. Avizonis and K. A. Truesdell. The chemical oxygen-iodine laser (coil). *Proc. SPIE*, 2502:180–202, 1995.

[2] A. A. Ayon, R. Braff, C. C. Lin, H. H. Sawin, and M. A. Schmidt. Characterization of a Time Multiplexed Inductively Coupled Plasma Etcher. *J. Electrochem. Soc.*, 146(1):339–349, 1999.

[3] H. D. Babcock and L. Herzberg. Fine structure of the red system of atmospheric oxygen bands. *Astrophysical Journal*, 108:167, 1948.

[4] B. D. Barmashenko and S. Rosenwaks. Theoretical modeling of chemical generators producing $O_2(^1\Delta)$ at high pressure for chemically pumped iodine lasers. *Journal of Applied Physics*, 73(4):1598–1611, 1993.

[5] D. J. Bernard and N. R. Pchelkin. Measurement of $O_2(^1\Delta)$ content in the gaseous effluents of a chemical generator. *Rev. Sci. Instrum.*, 49(6).

[6] J. C. Charpentier. Recent Progress in Two Phase Gas-Liquid Mass Transfer in Packed Beds. *The Chemical Engineering Journal*, 11:161–181, 1976.

[7] R. G. Derwent and B. A. Thrush.

[8] R. G. Derwent and B. A. Thrush. Measurements on $O_2(^1\Delta_g)$ and $O_2(^1\Sigma_g^+)$ in Discharge Flow Systems. *Transactions of the Faraday Society*, 67:2036–2043, 1971.

[9] S. Ergun. Fluid flow through packed columns. *Chem. Eng. Prog.*, 48(2):88–94, 1952.

[10] A. Gunther et al. Micromixing of Miscible Liquids in Segmented Gas-Liquid Flow. *Langmuir*, 21:1547–1555, 2005.

[11] B. A. Wilhite et al. Design of a MEMS-based microChemical Oxygen-Iodine Laser (microCOIL) System. *IEEE Journal of Quantum Electronics*, 40(8):2555–2562, 2004.

[12] B. A. Wilhite et al. Design of a Silicon-Based Microscale Trickle-Bed System for Singlet-Oxygen Production. *accepted for publication in AIChE Journal*, 2008.

[13] D. A. Copeland et al. Two-phase model of $O_2(^1\Delta)$ production with application to rotating disk generators. *Proc. SPIE*, 1871:203–228, 1993.

[14] D. A. Copeland et al. Exact and approximate solutions of the utilization and yield equations for $O_2(^1\Delta)$ generators. *Proc. SPIE*, 2119:27–41, 1994.

[15] D. L. Carroll et al. Continuous-wave laser oscillation on the 1315 nm transition of atomic iodine pumped by $O_2(^1\Delta)$ produced in an electric discharge. *Applied Physics Letters*, 86:111104, 2005.

[16] G. Watanabe et al. Modeling of crossflow jet-type singlet oxygen generator. *Journal of Applied Physics*, 97(11):114905, 2005.

[17] J. F. Hon et al. A heuristic method for evaluating COIL performance. *AIAA Journal*, 34(8):1595–1603, 1996.

[18] K. R. Kendrick et al. Determination of singlet-oxygen generator efficiency on a 10-kw class supersonic chemical oxygen-iodine laser (RADICL). *IEEE Journal of Quantum Electronics*, 35(12):1759–1764, 1999.

[19] L. F. Velasquez-Garcia et al. A MEMS Singlet Oxygen Generator-Part I: Device Fabrication and Proof of Concept Demonstration. *IEEE Journal of Microelectromechanical Systems*, 16:1482–1491, 2007.

[20] M. V. Zagidullin et al. Highly efficient jet $O_2(^1\Delta)$ generator. *Soviet Journal of Quantum Electronics*, 21(7):747–753, 1991.

[21] M. V. Zagidullin et al. Highly efficient supersonic chemical oxygen-iodine laser with a chlorine flow rate of 10 mmol s-1. *Soviet Journal of Quantum Electronics*, 27(3):195–199, 1997.

[22] M. W. Losey et al. Microfabricated Multiphase Packed-Bed Reactors: Characterization of Mass Transfer and Reactions. *Ind. Eng. Chem. Res.*, 40:2555–2562, 2001.

[23] N. G. Basov et al. *Chemical Lasers.* Springer-Verlag, Berlin, Germany, 1990.

[24] O. Aharon et al. $O_2(^1\Delta)$ generation in a bubble column reactor for chemically pumped iodine lasers: Experiment and modeling. *Journal of Applied Physics*, 70(10):5211–5220, 1991.

[25] R. P. Larkins et al. Two-phase concurrent flow in packed beds. *AIChE Journal*, 7:231–236, 1961.

[26] R. Srinivasan et al. Micromachined Reactors for Catalytic Partial Oxidation Reactions. *AIChE Journal*, 43(11).

[27] S. J. Arnold et al. Some New Emission Bands of Molecular Oxygen. *Journal of Chemical Physics*, 40(6):1769–1770, 1964.

[28] V. Rybalkin et al. Parametric study of a highly efficient chemical oxygen-iodine laser with supersonic mixing of iodine and oxygen. *Journal of Applied Physics*, 98(2):0213106, 2005.

[29] W. E. McDermott et al. An electronic transition chemical laser. *Applied Physics Letters*, 32(8), 1975.

[30] W. J. Lafferty et al. Rotational line strengths and self-pressure-broadening coefficients for the 1.27-μm $a^1\Delta_g$-$X^3\Sigma_g^-$ v = 0-0 band of O_2. *Appl. Opt.*, 37(12).

[31] T. Fujioka. Industrial gas laers between 1.05-10.6 μm range. *Infrared Physics*, 32:89, 1991.

[32] G. D. Hager, C. A. Helms, K. A. Truesdell, D. Plummer, J. Erkkila, and P. Crowell. A Simplified Analytic Model for Gain Saturation and Power Extraction in the Flowing Gas Chemical Oxygen Iodine Laser. *IEEE Journal of Quantum Electronics*, 32(9):1525–1536, 1996.

[33] A. M. Held, D. J. Halko, and J. K. Hurst. Mechanisms of chlorine oxidation of hydrogen peroxide. *Journal of the American Chemical Society*, 100:5732–5740, 1978.

[34] G. Herzberg. *Spectra of Diatomic Molecules.* D. Van Nostrand Company, New York, 1950.

[35] A. Hicks, S. Norberg, P. Shawcross, W. R. Lempert, J. W. Rich, and I. V. Adomovich. Singlet oxygen generation in a high pressure non-self-sustained electric discharge. *Journal of Physics D: Applied Physics*, 38:3812–3824, 2005.

[36] S. C. Hurlock. COIL Technology Development at Boeing. *Proc. SPIE*, 4631:101–115, 2002.

[37] G. C. Manke II, C. B. Cooper, S. C. Dass, T. J. Madden, and G. Hager. A Multiwatt All Gas-Phase Iodine Laser (AGIL). *IEEE Journal of Quantum Electronics*, 39(8).

[38] F. P. Incropera and D. P. DeWitt. *Introduction to Heat Transfer, Fourth Edition.* Wiley, New York, 2002.

[39] Y. Jiang, M. R. Khadilikar, M. H. Al-Dahhan, and M. P. Dudukovic. CFD of Multiphase Flow in Packed-Bed Reactors: I. k-Fluid Modeling Issues. *AIChE Journal*, 48(4):701–715, 2002.

[40] J. G. Kralj, H. R. Sahoo, and K. F. Jensen. Integrated continuous microfluidic liquid-liquid extraction. *Lab on a Chip*, 7(2):256–263, 2007.

[41] G. R. Kwirandt and W. O. Schall. Basic Experiments on the production of $O_2(^1\Delta)$. *Proc. SPIE*, 2502:331–337, 1995.

[42] H. V. Lilenfeld. Oxygen-iodine laser kinetics. Technical Report AFWL-TR-83-01, Air Force Research Lab, Kirtland AFB, Albuquerque, NM, 1983.

[43] Matthew Losey. PhD thesis, Massachusetts Institute of Technology.

[44] D. A. McQuarrie. *Physical Chemistry: A Molecular Approach.* University Science Books, Sausalito, CA, 1997.

[45] E. Bruce Nauman. *Chemical Reactor Design, Optimization, and Scaleup.* McGraw-Hill, New York, 2002.

[46] Y. Peles, V. T. Srikar, T. S. Harrison, C. Protz, A. Mracek, and S. M. Spearing. Fluidic Packaging of Microengine and Microrocket Devices for High-Pressure and High-Temperature operation. *IEEE Journal of Microelectromechanical Systems*, 13(1).

[47] G. P. Perram and G. D. Hager. The standard chemical oxygen-iodine laser kinetic package. Technical Report AFWL-TR-88-50, Air Force Weapons Lab, Kirtland AFB, Albuquerque, NM, 1988.

[48] W. T. Rawlins, S. Lee, J. Kessler, and S. J. Davis. Observations of gain on the $I(^2P_{1/2} \rightarrow {}^2P_{3/2})$ transition by energy transfer from $O_2(a^1\Delta_g)$ generated by microwave discharge in a subsonic flow reactor. *Applied Physics Letters*, 86(5):051105–1 – 051105–3, 2005.

[49] R. J. Richardson, C. E. Wiswall, P. A. G. Carr, F. E. Hovis, and H. V. Lilenfeld. An efficient singlet oxygen generator for chemically pumped iodine lasers. *Journal of Applied Physics*, 52:4962–4969, 1981.

[50] G. Ruiz-Ibanez. Solubility and diffusivity of oxygen and chlorine in aqueous hydrogen peroxide solutions. *J. Chem Eng. Data*, 36:459–466, 1991.

[51] E. N. Sieder and G. E. Tate. Heat Transfer and Pressure Drop of Liquids in Tubes. *Ind. Eng. Chem.*, 28:49, 1936.

[52] T. G. Slanger and P. C. Cosby. O_2 Spectroscopy below 5.1 eV. *The Journal of Physical Chemistry*, 92(2):267–282, 1988.

[53] E. Talmor. Two-Phase Downflow Through Catalyst Beds: Part I. Flow Maps. *AIChE Journal*, 23(6):868–874, 1977.

[54] W. J. Thayer, A. K. Cousins, and R. D. Romea. Modeling of uniform droplet singlet oxygen generators. *Proc. SPIE*, 2117:71–100, 1994.

[55] K. A. Truesdell, C. A. Helms, and G. D. Hager. A History of COIL Development in the USA. *Proc. SPIE*, 2502:217–237, 1995.

[56] Yasuhiro Wada, Martin A. Schmidt, and Klavs F. Jensen. Flow Distribution and Ozonolysis in Gas-Liquid Multichannel Microreactors. *Ind. Eng. Chem. Res.*, 45:8036–8042, 2006.

[57] S. Whitaker. Forced Convection Heat Transfer Correlations for Flow in Pipes, Past Flat Plates, Single Cylinders, Single Spheres, and for Flow in Packed Beds and Tube Bundles. *AIChE Journal*, 18(2):361–371, 1972.

[58] K. R. Williams and R. S. Muller. Etch rates for micromachining processing. *IEEE Journal of Microelectromechanical Systems*, 5(4), 1996.

[59] F. H. Yin, C. G. Sun, A. Afacan, K. Nandakumar, and K. T. Chuang. CFD Modeling of Mass-Transfer Processes in Randomly Packed Distillation Columns. *Ind. Eng. Chem. Res.*, 39:1369–1380, 2000.

[60] S. Yoshida, M. Endo, T Sawano, S. Amano, H. Fujii, and T. Fujioka. Chemical oxygen iodine laser of extremely high efficiency. *Journal of Applied Physics*, 65(2):870, 1989.